申报	系列：教师系列教学科研并重型
	专业：机械工程
	职称：副教授

业绩成果材料

（申报人的业绩成果材料包括论文、科研项目、获奖以及其他成果等）

单　位（二级单位） 工程学院

姓　名 卢家欢

材料核对人:　　单位盖章:

核对时间:

华南农业大学制

目　录

一、教研业绩

1.1 青年教师教学优秀奖（校级）

通知公告

华南农业大学2024-2025学年“青年教师教学优秀奖” 获奖名单

2025-12-31 来源:

各学院（部、中心）：

根据《华南农业大学青年教师教学优秀奖评选办法》（华南农办〔2017〕71号）经各学院（部、中心）推荐、学校审核、评奖专家组评审，确定廖建昭等20位教师获农业大学2024-2025学年“青年教师教学优秀奖”。现将获奖名单(按成绩排序)予以

奖项	姓名	比赛课程	单 位
一等奖	廖建昭	兽医临床诊断学	兽医学院
	罗均	兽医微生物学	兽医学院
	李征	中国近现代史纲要	马克思主义学院
二等奖	刘朝阳	园艺植物生物技术	园艺学院
	朱勇文	饲料学	动物科学学院
	侯丽娴	中外文化比较	外国语学院
	孙华	中国近现代史纲要	马克思主义学院
	罗琎昕	现代汉语	人文与法学学院
	黄欢	结构力学	水利与土木工程学院
	黄培奎	传感器与检测技术	工程学院
三等奖	龙健梅	药用植物遗传育种	林学与风景园林学院
	莫钊文	作物栽培学	农学院
	魏世娜	细胞生物学	海洋学院
	周毅	大学生心理健康教育	公共管理学院
	魏丹纯	英语写作	国际教育学院
	刘京一	景观生态学	林学与风景园林学院
	卢家欢	机械设计基础	工程学院

1.2 教改重点项目（校级）

华南农业大学文件

华南农教〔2025〕57号

关于公布华南农业大学2025年度校级本科教学质量与教学改革工程项目立项名单的通知

各学院、部处、各单位:

根据《关于开展2025年度校级本科教学质量与教学改革工程项目申报工作的通知》精神,经项目负责人申请、所在单位推荐、本科生院审核、学校组织专家评审和公示(无异议)等程序,决定立项“善境伦理学与风景园林专业实践教学深度融合的探索与实践”等127个项目为2025年度校级本科教学改革项目，立项“筑基·焕新·赋能：食品质量与安全专业‘新工科’建设暨工程教育认证提质创新工程”等52个项目为2025年度校级本科质量工程项目。具体名单见附件。

请各项目负责人按照项目建设任务及要求,及时开展各项改

革工作；各单位要切实履行项目建设主体责任，加强对项目建设的督促、指导，以确保项目建设任务高质量完成。

特此通知。

附件：1. 2025年度校级本科教学改革项目立项名单

2. 2025年度校级本科质量工程项目立项名单

华南农业大学

2025年10月14日

（联系人：孙齐胜；电　话：85288020）

公开方式：主动公开

华南农业大学党政办公室　　2025年10月15日印发

2025年度高等教育教学改革项目拟立项名单

序号	类型	项目名称	级别	所在单位	姓名
25	教学改革项目	英国文学史课程的AI知识图谱构建及数智化教学实践研究	重点	外国语学院	李良博
26	教学改革项目	AI赋能《数学分析》一流课程建设的改革与实践研究	重点	数学与信息学院 软件学	金玲玉
27	教学改革项目	AI背景下面向农经专业本科生的《大数据 分析与挖掘》课程体系建设与教学模式优化	重点	经济管理学院	文乐
28	教学改革项目	基于大模型辅助的软件体系结构课程生成式编程教学改革与实践	重点	数学与信息学院 软件学	林毅申
29	教学改革项目	《种子加工与贮藏学》“理论-实践-实习”三位一体教学的探索和实践	重点	农学院	张亚锋
30	教学改革项目	中华优秀传统文化融入高校思政课程的路径研究——聚焦《马克思主义基本原理》课程	重点	马克思主义学院	禹规娥
31	教学改革项目	新时代应用型人才培养模式创新改革与实践研究——以环境工程专业为例	重点	资源环境学院	陈烁娜
32	教学改革项目	产教融合视域下《家具定制技术》课程“三融四阶五维”教学模式创新与实践	重点	材料与能源学院	郭琼
33	教学改革项目	面向AI赋能的《机械设计基础》“1+1+1+N”混合式教学方法	重点	工程学院	王慰祖
34	教学改革项目	“科研-竞赛-创新”协同融合培养智慧农业拔尖人才探索与实践	重点	工程学院	何杰
35	教学改革项目	基于RAMP原则的“学科——安全” 化学实验双线融合教育体系构建与实践	重点	基础实验与实践训练中	林碧敏
36	教学改革项目	基于人工智能与虚拟仿真融合的《分子生物学》智慧课程体系建设与教学模式改革	重点	食品学院	叶志伟
37	教学改革项目	产科教融合视角下茶学专业课程体系优化与实践——以《茶树栽培学》为例	重点	园艺学院	郑鹏
38	教学改革项目	生成式AI驱动农林院校“新文科”教学模式创新 —《应急管理概论》智慧课程的建设实践	重点	公共管理学院	游艳玲

华南农业大学教育教学研究和改革项目

申 报 书

项目类别 重点项目

项目名称 面向 AI 赋能的《机械设计基础》“1+1+1+N”混合式教学方法

项目负责人 王慰祖

职 称 副教授

手机号码 [redacted]

所在单位 工程学院（公章）

申报日期 2025.6.10

华南农业大学 本科生院 制

二〇二五年 五月

		姓名	性别	出生年月	职称	工作单位	分工	签名[2]
	主要成员（不含申请者）	夏红梅	女	[illegible]	教授	工程学院	教学模式实践	夏红梅
		甄文斌	女	[illegible]	正高实验师	工程学院	案例收集整理	甄文斌
		卢家欢	男	[illegible]	副教授	工程学院	资源建设	卢家欢
		程碧懿	男	[illegible]	副教授	工程学院	资源建设	程碧懿

二、立项依据（项目研究的意义、现状分析）[3]

1. 立项依据

2019 年，中共中央、国务院印发《中国教育现代化 2035》，明确指出要加快教育信息化进程，推动现代信息技术与教育教学深度融合。最近几年，人工智能技术取得了飞速发展，快速渗透到社会的各个层面，教育领域同样经历着前所未有的变革。人工智能技术的广泛应用，不仅对传统的高等教育提出了巨大挑战，同时也为教育方法的革新创造了机会。

《机械设计基础》是省级线上线下混合一流课程，目前工程学院有机制、车辆、机化、机器人和工业设计等 5 个专业需要修读。作为机械工程专业核心课程，其对于培养学生工程设计能力、创新思维和解决实际问题能力具有重要意义。该课程包含《机械原理》和《机械设计》两部分，具有内容多、难点多、知识分散的特点，仅依靠目前的 64 学时很难覆盖全部重点内容，采用线上线下混合式教学方式后，通过学生自学加老师课堂讲解的方式理论上可以以较少学时学习更多内容，但依然存在学生自学效果差异大、学习过程难以监督等问题。因此，有必要在课程中引入人工智能技术，通过 AI 学伴等方式提高学生的自学效果，并通过大数据跟踪学生的学习进度，分析学生的学习难点和学习效果，使得教师能够及时调整教学策略，实现精准教学，从而有效提升课程教学质量。

2. 现状分析

[2]此页须成员手写签字后扫描成 PDF 电子版。

[3] 表格不够，可自行拓展加页；但不得附其他无关材料。下同。

1.3 智慧课程（校级）

华南农业大学校内公文

本科生院（招办）〔2026〕2 号

关于公布华南农业大学 2025 年度智慧课程认定结果的通知

各学院、部处，各相关单位:

根据《关于做好 2025 年度校级教学质量与教学改革工程项目结题验收工作的通知》要求，学校组织开展了项目的结题验收工作。经项目负责人所在单位组织专家结题、学校组织专家验收、公示等程序，认定《动物营养学》等 69 门校级智慧课程。请各单位高度重视智慧课程建设，以课程建设的智慧化带动专业智慧化升级。各项目负责人应加强项目成果的推广应用，争取获得更好的示范效果。

附件：1.2025 年度校级智慧课程认定名单

2.智慧课程认定标准（2025 年版）

19	智慧建设类课程	信息光学	翁嘉文	李海，杨初平，潘哲朗，曾应新，戴占海	电子工程学院（人工智能学院）
20	智慧建设类课程	森林培育学	邱权	何茜、刘效东、陈祖静、潘澜	林学与风景园林学院
21	智慧建设类课程	机电一体化与过程控制	齐龙	杨秀丽，邢航，冯骁，龚浩	水利与土木工程学院
22	智慧建设类课程	植物生理学	刘慧丽	张雪莲、陶利珍、刘亚林、郭长奎、王曼、柳青、刘太波、刘宇婷、罗娜	生命科学学院
23	智慧建设类课程	电影音乐欣赏	胡远慧	栾志弘、唐涤非、黎冬霞、李美群、李乐	艺术学院
24	智慧建设类课程	生态工程学	蔡昆争	蔡昆争 田纪辉 蔡一霞 舒迎花 陈桂葵	资源环境学院
25	智慧建设类课程	土力学	黄金林	姜俊红、余长洪、胡威	水利与土木工程学院
26	智慧课程培育项目	兽医寄生虫学	元冬娟	郭亚琼，李娜，夏宁波，许瑞冯耀宇	兽医学院
27	智慧课程培育项目	劳动经济学	陈然	张雯闻、徐汹涛、杜玉红、张丽瑜、曾敏峰、徐强	公共管理学院
28	智慧课程培育项目	兽医临床诊断学	廖建昭	唐兆新，张辉，胡莲美，李英，郭剑英，潘家强，韩庆月	兽医学院
29	智慧课程培育项目	机械设计基础	王慰祖	夏红梅、卢家欢、程碧懿、卿艳梅	工程学院
30	智慧培育类课程	水污染控制工程	余光伟	梁瑜海、种云霄、陈澄宇、仲海涛、黄柱坚、陈杨梅	资源环境学院
31	智慧培育类课程	果树栽培生理（双语）	黄旭明	赵明磊 曾仁芳	园艺学院

二、科研项目

2.1 主持：国家自然科学基金青年基金项目（A 类）

项目批准号	52407246
申请代码	E0707
归口管理部门	
依托单位代码	51064208A0499-0932

5240724610014 57

国家自然科学基金

资助项目计划书

（包干制项目）

资助类别：青年科学基金项目

亚类说明：

附注说明：

项目名称：跨型号多场景电池衰老相似性对衰老态势感知算法迁移的导向研究

资助经费：30万元　　执行年限：2025.01-2027.12

负 责 人：卢家欢　　BRID：05165.00.07280

通讯地址：天河区华南农业大学工程学院

邮政编码：510642　　电　　话：020-85280783

电子邮件：jhlu@scau.edu.cn

依托单位：华南农业大学

联 系 人：唐家林　　电　　话：020-85280070

填表日期：2024年08月27日

国家自然科学基金委员会制

Version：1.001.457

国家自然科学基金资助项目计划书填报说明

（包干制项目）

一、项目负责人收到《国家自然科学基金资助项目批准通知》（以下简称《批准通知》）后，请认真阅读本填报说明，参照国家自然科学基金相关项目管理办法和新修订的《国家自然科学基金资助项目资金管理办法》（以下简称《资金管理办法》，请查阅国家自然科学基金委员会官方网站首页“政策法规”栏目），按《批准通知》的要求认真填写和提交《国家自然科学基金资助项目计划书》（以下简称《计划书》）。

二、填写《计划书》时要科学严谨、实事求是、表述清晰、准确。《计划书》经国家自然科学基金委员会相关项目管理部门审核批准后，将作为项目研究计划执行、检查和验收的依据。

三、《计划书》各部分填写要求如下：

（一）简表：由系统自动生成。

（二）摘要及关键词：各类获资助项目都应当填写中、英文摘要及关键词。

（三）正文：

1. 青年科学基金项目、青年学生基础研究项目：如果《批准通知》所附“项目评审意见及修改意见表”中“修改意见”栏目没有修改要求的，只需选择“研究内容和研究目标按照申请书执行”即可；如果《批准通知》中上述栏目明确要求调整研究期限或研究内容等的，须选择“根据研究方案修改意见更改”并填报相关修改内容。

2. 国家杰出青年科学基金项目和优秀青年科学基金项目按下列提纲撰写：

（1）研究方向；

（2）结合国内外研究现状，说明研究工作的学术思想和科学意义（限两个页面）；

（3）研究内容、研究方案及预期目标（限两个页面）；

（4）年度研究计划；

四、资助经费相关要求：

1. 资助经费批准时不再区分直接费用和间接费用。

2. 项目负责人在提交计划书时需签署承诺书，承诺尊重科研规律，弘扬科学家精神，遵守科研伦理道德和作风学风诚信要求，认真开展科学研究工作；承诺项目经费全部用于与本项目研究工作相关的支出，不得用于与本项目研究无关的支出。

3. 项目负责人提交计划书时，无需编制项目预算。项目资金由项目负责人自主决定使用，按照《资金管理办法》第九条规定的开支范围列支。有关管理费用的补助支出，由依托单位根据实际管理需要，在充分征求项目负责人意见基础上合理确定。绩效支出由项目负责人根据实际科研需要和相关薪酬标准自主确定，依托单位按照工资制度进行管理。对于青年学生基础研究项目，支付给项目负责人本人的劳务费用，应符合相关比例要求。其余用途经费无额度限制，由项目负责人根据实际需要自主决定使用。

4. 项目结题时，项目负责人根据实际使用情况编制项目经费决算，经依托单位财务、科研管理部门审核后，报自然科学基金委。依托单位应当在单位内部公开非涉密项目立项、主要研究人员、资金使用（重点是间接费用、外拨资金、结余资金使用等）、决算、大型仪器设备购置以及项目研究成果等情况，接受内部监督。
5. 自然科学基金委结合项目管理，对经费使用情况和依托单位管理情况定期开展抽查。

简表

项目负责人信息	姓　　名	卢家欢	性 别	男	出生年月	[illegible]	民 族	汉族
	学　　位	博士			职称	副教授		
	是否在站博士后	否			电子邮件	jhlu@scau.edu.cn		
	电　　话	020-85280783			个人网页			
	工 作 单 位	华南农业大学						
	所 在 院 系 所	工程学院						
依托单位信息	名　　称	华南农业大学					代码	51064208A0499
	联 系 人	唐家林			电子邮件	kycjhk@scau.edu.cn		
	电　　话	020-85280070			网站地址	http://kjc.scau.edu.cn/		
合作单位信息	单 位 名 称							
项目基本信息	项 目 名 称	跨型号多场景电池衰老相似性对衰老态势感知算法迁移的导向研究						
	资 助 类 别	青年科学基金项目			亚 类 说 明			
	附 注 说 明							
	申 请 代 码	E0707:电能存储与应用						
	基 地 类 别							
	执 行 年 限	2025.01-2027.12						
	资 助 经 费	30万元						

项目摘要

中文摘要：

锂离子电池是运载装备与电化学储能的核心器件，其长期应用安全和科学梯次利用依赖于衰老态势精准感知。现有感知算法在跨型号多场景迁移时过度依赖长周期高成本的衰老测试，制约电池的进一步发展。本项目拟开展跨型号多场景电池衰老相似性对衰老态势感知算法迁移的导向研究，用多源衰老相似数据取代测试：①探究从本征特性与使用特性解耦电池衰老规律，构建跨型号多场景衰老相似性度量，揭示衰老相似性对算法迁移的作用机理；②探究衰老相似性度量在衰老评估迁移中的引导机制，并融入物理信息，构建多源相似数据与物理信息协同引导的跨型号多场景衰老评估模型；③探究面向不确定应用场景的多维度残余价值预测方法，利用多源衰老相似数据引导先验预测和不确定性场景量化，通过内嵌物理模型解析衰老历程和衰后特性信息。预期形成电池衰老评估与残值预测的跨型号、多场景快速精准迁移方法。研究成果为新能源运载装备及新型储能系统快速精准开发提供科学理论依据。

Abstract：

Lithium-ion batteries serve as critical components for transportation equipment and electrochemical energy storage, and their long-term safety and scientific utilization hinge upon precise aging estimation and prediction algorithms. Existing algorithms for aging estimation and prediction rely extensively on prolonged and costly aging tests when transferring to cross-type multi-scenario batteries, thus hindering the further development of batteries. This project focuses on cross-type multi-scenario battery aging similarity and its guidance on the migration of aging estimation and prediction algorithms, aiming to replace testing with multi-source aging similarity data: ① Investigate the decoupling of aging patterns from intrinsic and usage characteristics, construct a cross-type and multi-scenario battery aging similarity metric, and elucidate the mechanism of aging similarity on algorithm transfer. ② Explore the guiding mechanism of aging similarity metrics in the transfer of aging estimation, and incorporate physical information to construct a cross-type and multi-scenario aging estimation model guided by multi-source similar data and physical information. ③ Investigate multi-dimensional residual value prediction methods for uncertain application scenarios, utilize multi-source aging similarity data to guide prior prediction and quantification of uncertainty scenarios, and analyze aging trajectories and post-aging characteristics through embedded physical models. The project aims to develop rapid and accurate cross-type and multi-scenario transfer methods for battery aging estimation and residual value prediction. The research results will provide a scientific theoretical basis for the rapid and accurate development of new energy transportation equipment and novel energy storage systems.

关键词(用分号分开)：新能源汽车；运载装备电能存储；电池管理；状态估计；寿命预测

Keywords(用分号分开)： New Energy Vehicles; Electric Energy Storage for Transportation Equipment; Battery Management; State Estimation; Life Prediction

报告正文

研究内容和研究目标按照申请书执行。

2.2 主持：广东省自然科学基金面上项目（B 类）

受理编号：c25140500000832

项目编号：2025A1515010354

文件编号：粤基金字〔2025〕10号

广东省基础与应用基础研究基金项目

任务书

项目名称：迁移学习驱动的跨型号电池衰老状态估计及衰后特性预测

项目类别：广东省自然科学基金-面上项目

项目起止时间：2025-01-01 至 2027-12-31

管理单位（甲方）：广东省基础与应用基础研究基金委员会

依托单位（乙方）：华南农业大学

通讯地址：广东省广州市天河区五山路483号

邮政编码：510642 单位电话：020-85283435

项目负责人：卢家欢 联系电话：

（广东科技微信公众号） （查看任务书信息） （受理纸质材料二维码）

广东省基础与应用基础研究
基金委员会
二〇二〇年制

填写说明

一、项目任务书内容原则上要求与申报书相关内容保持一致，不得无故修改。

二、项目承担单位通过广东省科技业务管理阳光政务平台下载项目任务书，按要求完成签名盖章后扫描上传到广东省科技业务管理阳光政务平台。

三、签名盖章说明。请分别在单位工作分工及经费分配情况页、人员信息页、签约各方页等地方按要求签字或盖章，签章不合规或错漏将不予受理。其中，人员信息页要求所有参与人员本人亲笔签名，代签或印章无效，漏签将不予受理。

四、本任务书自签字并加盖公章之日起生效，各方均应负本任务书的法律责任，不应受机构、人事变动影响。

五、根据《广东省科学技术厅广东省财政厅关于深入推进省基础与应用基础研究基金项目经费使用“负面清单+包干制”改革试点工作的通知》（粤科规范字〔2022〕2号），2022年度及以后立项资助的全部省基金项目（包括省自然科学基金、省市联合基金、省企联合基金项目等）均适用“负面清单+包干制”，项目提交申请书和任务书时无需编制费用明细科目预算。

一、主要研究内容和要达到的目标

（1）主要研究内容：

①跨型号多场景衰老相似性度量及其对算法迁移的作用机理

研究多型号电池在各类场景下长周期运行的衰老演化规律，重点从本征特性与使用特性维度解耦衰老规律，提取显著表征跨型号多场景衰老共性和差异性的主成分特征；研究跨型号多场景电池衰老相似性度量方法，厘清本征特性相似与使用特性相似在跨电池多场景衰老特性相似性中的权重规律；揭示衰老相似性度量对衰老评估及残值预测算法迁移的正向作用机理，为迁移提供理论基础。

②多源相似数据与物理信息协同引导的跨电池衰老评估建模

研究由目标电池片段运行数据驱动、多源衰老相似数据与物理信息协同引导跨型号多场景迁移的衰老评估模型；研究多源衰老相似性数据在跨型号多场景衰老评估中的引导机制，利用衰老相似性度量精细化组建最优正向迁移作用的多源训练集，并引导分配衰老相似样本的学习权重；研究物理信息在跨型号多场景衰老评估中的引导机制，通过建立共性本征物理信息嵌入机制，启发动力学和热力学的机理化学习，增强跨型号多场景衰老评估的可解释性。

③面向未来不确定应用场景的电池多维度残余价值预测

研究多源衰老相似数据与共性物理信息协同引导的电池多维度残余价值预测架构，内嵌跨型号迁移和未来多应用场景切换机制；研究多源衰老相似数据在长时衰老预测的引导机制，包括本征相似性先验预测和使用相似性不确定应用场景生成量化；研究共性物理信息在长期衰老预测中的引导机制，建立共性物理内嵌模型，利用编码启发并约束长时预测，通过解码解析未来不确定场景下的衰老历程、衰后特性等多维度残余价值信息。

④电池衰老评估与残余价值预测的跨型号多场景应用验证

搭建边云协同的算法验证台架，模拟运载装备电能储存过程中可能出现的实际应用场景，验证电池全寿命衰老特性预测的跨型号迁移提升效果，重点检验算法精度与面对未来不确定使用工况的适应性能。

（2）研究目标

本项目旨在突破当前算法面临的长周期、高成本测试依赖性以及不确定工况适应性差等难题，提出迁移学习驱动的科学方案，期望达成以下目标：

①建立跨型号多场景电池的衰老相似性度量，深入揭示衰老相似性对衰老评估及残值预测算法迁移的正向作用机理；

②构建多源数据与物理信息协同引导的跨型号多场景衰老评估模型；

③提出面向未来不确定应用场景的电池多维度残余价值预测方法；

④通过台架进行迁移验证并完善所提算法，形成完整的电池跨型号衰老特性预测方法体系，解决长周期、高成本、适应性差等问题。

二、项目预期获得的研究成果及形式

<table>
<tr><td rowspan="3">论文及专著情况</td><td colspan="2">国家统计源刊物以上刊物发表论文（篇）</td><td colspan="2">6</td><td colspan="2">科技报告（篇）</td><td colspan="2">2</td></tr>
<tr><td colspan="2">其中被SCI/EI/ISTP收录论文数（篇）</td><td colspan="2">6</td><td colspan="2">培养人才（人）</td><td colspan="2">5</td></tr>
<tr><td colspan="2">专著（册）</td><td colspan="2">0</td><td colspan="2">引进人才（人）</td><td colspan="2">1</td></tr>
<tr><td rowspan="2">专利情况(项)</td><td colspan="2">发明专利</td><td colspan="2">实用新型专利</td><td colspan="2">外观设计专利</td><td colspan="2">国外专利</td></tr>
<tr><td>申请</td><td>授权</td><td>申请</td><td>授权</td><td>申请</td><td>授权</td><td>申请</td><td>授权</td></tr>
<tr><td></td><td>3</td><td>0</td><td>0</td><td>0</td><td>0</td><td>0</td><td>0</td><td>0</td></tr>
</table>

三、项目进度和阶段目标

（一）项目起止时间： 2025-01-01 至 2027-12-31

（二）项目实施进度及阶段主要目标：

开始日期	结束日期	主要工作内容
2025-01-01	2025-12-31	重点研究跨型号多场景衰老相似性度量及其对算法迁移的作用机理： ①聚合公开数据集、过去自主构建的数据集以及开源工程数据集等多种数据源，构建多源电池衰老数据库； ②研究多型号电池在各类场景下的衰老演化规律，从本征与使用特性维度解耦分析衰老特性，提取显著反映衰老共性和差异性的关键特征； ③深入探究电池全寿命周期运行数据的衰老相似性度量方法； ④揭示衰老相似性度量对衰老评估及残值预测算法迁移能力的作用机理。 该阶段预期发表高水平SCI论文2篇，至少申请国家发明专利1件，投稿并参加电气相关领域学术会议。
2026-01-01	2026-12-31	重点研究多源相似数据与物理信息协同引导的跨电池衰老评估建模： ①构建由目标电池片段运行数据驱动、多源衰老相似数据与物理信息协同引导跨型号多场景迁移的衰老评估模型； ②研究多源衰老相似性数据在电池跨型号多场景衰老评估中的引导机制； ③研究物理信息在跨型号多场景衰老评估中的引导机制； ④研究相似性数据与物理信息协同引导的跨型号多场景衰老评估方法。 该阶段预期发表高水平SCI论文2篇，至少申请国家发明专利1件，投稿并参加电气相关领域学术会议。
2027-01-01	2027-12-31	重点研究面向未来不确定应用场景的多维度残余价值预测及相关验证： ①构建多源衰老相似数据与物理信息协同驱动、支持跨型号迁移和未来应用场景切换的电池残余价值预测架构； ②研究多源衰老相似数据在长时残值预测过程的引导机制，包括先验预测和不确定应用场景生成机制； ③研究共性物理信息在长期衰老预测过程中的引导机制，通过内嵌共性物理模型启发并约束长时衰老预测； ④研究面向未来不确定应用场景的电池多维度残余价值预测方法； ⑤搭建边云协同的多场景验证台架，验证并完善相关算法。 该阶段预期发表高水平SCI论文2篇，至少申请国家发明专利1件，投稿并参加电气相关领域学术会议，对所有研究成果进行归纳分析，完成项目结题。

四、项目总经费及省基金委经费预算

1.省基金委经费下达总额：（大写）壹拾万圆整；（小写 ）10万元；					
2.省基金委经费年度下达计划：					
年度	2025 年	年	年	年	年
经费(万元)	10.00				

五、人员信息

项目负责人

姓名	证件号码	年龄	性别	职称	学历	在项目中承担的任务	所在单位	签名
卢家欢			男	副教授	博士研究生	项目负责人	华南农业大学	

项目组主要成员

姓名	证件号码	年龄	性别	职称	学历	在项目中承担的任务	所在单位	签名
李杰浩			男	副教授	博士研究生	机理研究	华南农业大学	
曾山			男	研究员	博士研究生	机理研究	华南农业大学	
吴伟斌			男	教授	博士研究生	算法研究	华南农业大学	
王昱			女	副教授	博士研究生	算法研究	华南农业大学	
张闻宇			男	助理研究员	博士研究生	集成验证	华南农业大学	
杨禹锟			男	未取得	硕士研究生	机理研究	华南农业大学	
陈纳			男	未取得	本科	算法研究	华南农业大学	
邓棋瀚			男	未取得	本科	算法研究	华南农业大学	
徐宇航			男	未取得	本科	集成验证	华南农业大学	
李城林			男	未取得	本科	集成验证	华南农业大学	

六、工作分工及财政经费分配

承担/参与单位名称（盖章）	工作分工	省级财政科技资金分配（万元）
华南农业大学	全面负责项目攻关	10.00
	合计	10.00

七、任务书条款

第一条 甲方与乙方根据《中华人民共和国民法典》及国家有关法规和规定，按照《广东省自然科学基金及联合基金项目管理实施细则》（粤科规范字〔2024〕5号）《省级科技计划项目任务书管理细则》（粤科规范字〔2022〕8号）等规定，为顺利完成（2025）年迁移学习驱动的跨型号电池衰老状态估计及衰后特性预测专项项目（项目编号：2025A1515010354）经协商一致，特订立本任务书，作为甲乙双方在项目实施管理过程中共同遵守的依据。

第二条 甲方的权利义务：1.按任务书规定进行经费核拨的有关工作协调。2.根据甲方需要，在不影响乙方工作的前提下，定期或不定期对乙方项目的实施情况和经费使用情况进行检查或抽查。3.根据《广东省科学技术厅科技计划项目科研诚信管理办法》〔粤科规范字〔2024〕2号〕《广东省基础与应用基础研究基金项目科研不端行为调查处理实施细则（试行）》〔粤科规范字〔2023〕1号〕等规定对乙方进行科技计划信用管理。

第三条 乙方的权利义务：1.确保落实自筹经费及有关保障条件。2.按任务书规定，对甲方核拨的经费实行专款专用，单独列账，并随时配合甲方进行监督检查。3.经费使用按照广东省级财政科研项目经费使用及省基金项目经费使用“负面清单+包干制”等有关规定进行管理。4.项目依托单位应制定经费使用“负面清单+包干制”内部管理制度并报甲方备案。5.使用财政资金采购设备、原材料等，按照《广东省实施〈中华人民共和国招标投标法〉办法》有关规定，符合招标条件的须进行招标。6.项目任务书任务完成后，或任务书规定的任务、指标及经费投入等提前完成的，乙方可提出验收结题申请，并按甲方要求做好项目验收结题工作。7.若项目发生需要终止结题的情况，乙方须提出终止结题申请，并按甲方要求做好项目终止结题工作。8.在每年规定时间内向甲方如实提交上年度工作情况报告，报告内容包含上年度项目进展情况、经费决算和取得的成果等。9.按照国家和省有关规定，提交科技报告及其他材料。10.利用甲方的经费获得的研究成果，项目负责人和参与者应当注明获得“广东省基础与应用基础研究基金（英文：Guangdong Basic and Applied Basic Research Foundation）〔项目编号〕”资助或作有关说明。11.乙方要恪守科学道德准则，遵守科研活动规范，践行科研诚信要求，不得抄袭、剽窃他人科研成果或者伪造、篡改研究数据、研究结论；不得购买、代写、代投论文，虚构同行评议专家及评议意见；不得违反论文署名规范，擅自标注或虚假标注获得科技计划（专项、基金等）等资助；不得弄虚作假，骗取科技计划（专项、基金等）项目、科研经费以及奖励、荣誉等；不得有其他违背科研诚信要求的行为。12.确保本项目开展的研究工作符合我国科技伦理管理相关规定。

第四条 在履行本任务书的过程中，如出现广东省相关政策法规重大改变等不可抗力情况，甲方有权对所核拨经费的数量和时间进行相应调整。

第五条 在履行本任务书的过程中，当事人一方发现可能导致项目整体或部分失败的情形时，应及时通知另一方，并采取适当措施减少损失，没有及时通知并采取适当措施，致使损失扩大的，应当就扩大的损失承担责任。

第六条 本项目技术成果的归属、转让和实施技术成果所产生的经济利益的分享，除双方另有约定外，按国家和广东省有关法规执行。

第七条 根据项目具体情况，经双方另行协商订立的附加条款，作为本任务书正式内容的一部分，与本任务书具有同等效力。

第八条 本任务书一式三份，各份具有同等效力。甲、乙方及项目负责人各执一份，三方签字、盖章后即生效，有效期至项目结题后一年内。各方均应负任务书的法律责任，不应受机构、人事变动的影响。

第九条 乙方必须接受甲方聘请的本项目任务书监理单位的监督和管理。监理单位按照甲方赋予的权利对本项目任务书的履行进行审核、进度调查，对项目任务书变更、经费使用情况进行监督管理及组织项目验收。

说明：1. 本任务书中，凡是当事人约定无需填写的内容，应在空白处划（/）。
2. 委托代理人签订本任务书的，应出具合法、有效的委托书。

八、本任务书签约各方

管理单位（甲方）：　　广东省基础与应用基础研究基金委员会（盖章）

法定代表人（或法人代理）：曾路　（签章）

2025 年　03 月　21 日

依托单位（乙方）：　华南农业大学　（盖章）

法定代表人（或法人代理）：　薛红卫　（签章）

联系人（项目主管）姓名：　夏杰　（签章）

Email：　kjcgxk@scau.edu.cn

电话：　020 85283435　/

开户单位名称：　华南农业大学

开户银行名称：　广东广州工行五山支行

开户银行账号：　3602002609000310520

2025 年 4 月 9 日

联系人（项目负责人）姓名：　卢家欢　（签名）

Email：　491157160@qq.com

电话：

2025 年 4 月 7 日

2.3 主持：广西科技重大专项课题（B 类）

任务书编号： 桂科JF2504240002-1
课 题 类 别： 广西科技重大专项

广西创新驱动发展专项资金项目
课 题 任 务 书

项 目 名 称 ： 智能化切段式甘蔗联合收获机的整机研发与应用示范

课 题 名 称 ： 甘蔗梢部智能识别与精准切梢控制技术

项目牵头单位（甲方）： 广西柳工农业机械股份有限公司

课题承担单位（乙方）： 华南农业大学
广西柳工农业机械股份有限公司
广西科技大学

任 务 下 达 单 位 ： 广西壮族自治区科学技术厅

广西壮族自治区科学技术厅
二〇二四年制

第一条 广西柳工农业机械股份有限公司（以下简称甲方）与 华南农业大学、广西柳工农业机械股份有限公司、广西科技大学（以下简称乙方）依据《广西壮族自治区创新驱动发展专项资金管理办法(修订)》（桂财教〔2022〕36号）、《广西科技计划项目管理办法》的通知（桂科规字〔2025〕16号）、《广西科技重大专项经费管理办法（试行）》（桂财教〔2017〕80号）和有关法律、法规，为顺利完成自治区科技厅关于下达2025年广西科技计划立项项目（第四批）的通知（桂科发〔2025〕424号）文件下达的广西创新驱动发展专项资金项目“ 智能化切段式甘蔗联合收获机的整机研发与应用示范”(合同编号:桂科JF2504240002)所属课题“甘蔗梢部智能识别与精准切梢控制技术”（以下简称本课题），特签订本任务书。

第二条 本课题实施期限为自 2025年11月至2028年10月，乙方按以下要求完成本课题：

一、总体目标和主要内容（包括研究解决的问题、技术关键及创新内容）

1.课题总体目标：

课题聚焦于切段式甘蔗收获过程中存在的梢部识别不稳、切割路径不准与连续作业响应迟滞等关键瓶颈，旨在构建集视觉感知、空间定位与高精度执行控制于一体的甘蔗梢部智能切割技术体系。面向蔗田“高密植、多遮挡、光照剧烈变化”等典型非结构化作业环境，构建融合空间先验与时序感知能力的多目标识别模型，提升系统对主茎与蔗梢边界的精准辨识能力融合多视角RGB-D图像与点云信息，实现蔗梢三维结构重建与多个切割点的协同空间定位与路径排序。针对不同切割姿态需求，开发具备多角度调节、轨迹预调与滞后补偿能力的智能执行机构，支撑多目标之间的轨迹切换与作业连续性控制。最终实现田间环境下甘蔗梢部的精准识别、空

		智能化关键技术，负责课题技术方案设计、实验实施及报告撰写	梢部切割点识别精度不低于85%，切割误差不高于±25 mm；经济指标 2.晋升高级职称1人；培养研究生3名。 3.申请发明专利2项，其中，授权发明专利1项；发表学术论文2篇。	
2	广西柳工农业机械股份有限公司	协助开展数据采集与相关方法验证	/	0
3	广西科技大学	协助切梢硬件设计	/	0

主要研究、开发人员及责任分工如下：

姓名	性别	年龄	身份证号	职称	从事专业	工作单位	研究开发中的责任分工
卢家欢	男	[illegible]	[illegible]	副高级-副教授	农业工程	华南农业大学	课题1负责人
曾山	男	[illegible]	[illegible]	正高级-研究员	农业工程	华南农业大学	切割策略
张闻宇	男	[illegible]	[illegible]	中级-讲师（高校）	农业工程	华南农业大学	切割末端执行设计
杨禹锟	男	[illegible]	[illegible]	中级-讲师（高校）	农业工程	华南农业大学	课题1科研财务助理，试验与调试测试
高巧明	男	[illegible]	[illegible]	正高级-正高级工程师	智能农机装备	广西科技大学	协助切梢硬件设计
罗青康	男	[illegible]	[illegible]	中级-工程师	电气自动化	广西柳工农业机械股份有限公司	协助开展数据采集与相关方法验证
黄健友	男	[illegible]	[illegible]	中级-工程师	工程力学	广西科技大学	协助切梢硬件设计
梁汉康	男	[illegible]	[illegible]	中级-工程师	过程装备与控制工程	广西柳工农业机械股份有限公司	协助开展数据采集与相关方法验证

沈毅	男		[illegible]	中级-工程师	机械工程及自动化	广西柳工农业机械股份有限公司	协助开展数据采集与相关方法验证

第五条 甲方应当在自治区财政项目资金拨付到账后30天内向乙方转拨课题经费。本课题科技经费（伍拾万零肆仟元整）50.40万元，按课题实施进度分期拨给乙方，首期拨付（叁拾伍万贰仟捌佰元整）35.28万元，第二年拨付0万元，第三年拨付（壹拾伍万壹仟贰佰元整）15.12万元，待课题验收后拨付0万元。如乙方未能完成本课题任务书规定的计划任务，甲方可依据乙方完成课题情况拨付课题经费。

第六条 乙方必须按规定使用甲方转拨给的科技经费。课题经费单独核算，专款专用。科技经费用途预算如下：

科目	金额（万元）	开支内容
合　　计	50.40	/
（一）直接费用	41.40	/
设备费	6.00	购买质构仪2台，用于甘蔗梢部力学性能测试
业务费	28.00	主要用于材料费、测试化验加工费、差旅费、以及出版/文献/信息传播/知识产权事务费等
劳务费	7.40	临时聘用人员、在校研究生补贴、专家咨询费等
(二)间接费用	9.00	/
绩效支出	5.40	学校及参与项目成员绩效支出
其他费用	3.60	项目管理费

各单位的财政科技经费预算如下：

1、华南农业大学

科目	金额（万元）	开支内容
合　　计	50.40	/
（一）直接费用	41.40	/
设备费	6.00	购买质构仪2台，用于甘蔗梢部力学性能

签订任务书各方：

甲方：广西柳工农业机械股份有限公司（盖章）

法人代表（或受委托人）：（签章）

项目负责人：（签章）

签章日期：2026 年 1 月 8 日

乙方1：华南农业大学（盖章）

法人代表（或受委托人）：（签章）

课题负责人：（签章）

帐户名称：华南农业大学

开户银行：中国工商银行广州五山支行

帐　　号：3602002609000310520

签章日期：2026 年 1 月 8 日

乙方2：广西柳工农业机械股份有限公司（盖章）

法人代表（或受委托人）：（签章）

课题负责人：（签章）

帐户名称：广西柳工农业机械股份有限公司

开户银行：中国建设银行和平路支行

帐　　号：45050162376700000023

签章日期：2026 年 1 月 8 日

乙方3：广西科技大学（盖章）

法人代表（或受委托人）：（签章）

课题负责人：（签章）

帐户名称：广西科技大学

开户银行：中国农业银行柳州祥兴支行

帐　　号：20112801040000305

签章日期：2026 年 1 月 8 日

广西壮族自治区科学技术厅同意备案（盖章）

签章日期：2026 年 3 月 4 日

2.4 主持：四川省农业科学院开发课题项目（C 类）

四川省农业科学院　中国电信四川公司

2024 年“天府粮仓”数字农业川渝联合创新重点实验室-火花计划开放课题任务书

课　题　名　称：不规则地块全覆盖的新能源底盘无人作业路径规划

承　担　单　位：华南农业大学

课　题　负　责　人：卢家欢

立　项　经　费：30 万元

联　系　电　话：[redacted]

电　子　邮　箱：jhlu@scau.edu.cn

填　报　日　期：2024 年 09 月 20 日

“天府粮仓”数字农业川渝联合创新重点实验室管理委员会制

二〇二四年九月

一、课题基本情况

（一）名称及实施周期

课题名称：不规则地块全覆盖的新能源底盘无人作业路径规划

实施周期：任务签订之日至2025年12月

（二）立项背景和重要性

（三）课题任务

研究内容：

（1）多源信息融合驱动作业地块全覆盖感知

研究影响地形全覆盖感知性能的关键信息；研究多源信息的融合算法，提高感知精度；研究由多源信息融合驱动的不规则作业地块感知方法，为后续的路径规划和作业决策提供基础。

（2）新能源底盘适应性建模与作业状态监测

研究新能源农用底盘的物理结构、动力源性能以及运动学特性；研究底盘关键作业状态的在线监测方法，精准获取关键作业状态，为后续的路径规划和作业决策提供前馈与反馈信息。

（3）无人作业路径规划与动力管理协同优化

研究能够适应不规则地形的自主路径规划算法，综合考虑农业生产代表性环节的需求；研究新能源农用底盘的动力源管理策略；探究无人作业路径规划与动力管理协同优化方法。

技术路线：

（1）多源信息融合驱动作业地块全覆盖感知

首先，研究影响地形全覆盖感知性能的关键信息。通过收集多源数据，建立综合信息数据库，深入分析并揭示影响地形全覆

盖感知性能的关键信息规律。拟采用空间插值算法、图像处理等技术，对地形地貌、作物分布等信息进行精细化描述。然后，研究多源信息的融合算法。考虑到不同信息来源的特性，拟采用贝叶斯网络、模糊集合等理论来探索数据融合方法。为了进一步提高感知准确性和可靠性，拟引入卷积神经网络、循环神经网络等深度学习算法，对融合后数据进行特征提取和分类，以获取更准确的地形和作物信息。随后，研究由多源信息融合驱动的不规则作业地块感知方法。拟采用基于语义分割的图像处理方法，以识别出不同地形的有效作业边界和特征。与此同时，构建地形模型和作物分布图，为后续路径规划和作业决策提供基础数据支持。最后，开展感知方法性能验证，评估感知系统的准确性和可靠性。

（2）新能源底盘适应性建模与作业状态监测

首先，研究新能源农用底盘的物理结构、动力源性能以及运动学特性，以某型号新能源农用底盘为例，拟采用逆向工程和仿真分析方法，建立基础的底盘动力学模型，同时，结合动力电源性能测试数据，建立动力电源模型，评估底盘在不同作业条件下的机电响应特性。然后，基于感知获取的作业地块信息，拟建立具备不规则地块适应性的底盘模型，并通过仿真分析，评估底盘在不同作业条件下的响应特性。随后，研究新能源底盘关键作业状态的在线监测方法，拟采用传感器技术和数据通信技术，实时监测底盘的位姿、作业速度等关键作业状态。同时，结合底盘模型以及速度、位置等机载传感器信号，研发数据处理与在线监测机制，实现底盘作业状态的精准获取和可视化展示。最后，研究

底盘适应性建模与作业状态监测之间的协同运作机制，拟通过构建底盘模型和监测系统的前馈反馈机制，为最优路径规划提供科学依据。

（3）无人作业路径规划与动力管理协同优化

首先，研究能够适应不规则地形的自主路径规划算法，以四边形地块为例，拟采用图论和搜索算法相结合的方法，构建作业地块的拓扑图或网格图，拟采用 A*算法、Dijkstra 算法等经典搜索算法寻找从起点到终点的最优路径。然后，研究新能源农用底盘的动力源管理策略，拟分析底盘的动力源性能和作业需求，制定合理计划，对动力源进行高效利用和安全性保障，提高底盘的作业效率和续航能力。随后，探究无人作业路径规划与动力管理协同优化方法，拟采用遗传算法、粒子群算法等群智能优化算法，对路径规划和动力管理进行协同优化，构建适应不规则地块的新能源底盘路径规划系统，并求解最优解，提高农业生产的自动化水平和智能化水平。最后，验证系统的有效性和实用性，拟开展系统仿真实验和实地测试验证，评估优化方法的性能和效果，最终形成相关成果材料。

创新性：

（1）揭示影响复杂地形全覆盖感知性能的关键信息规律，通过融合多种信息来源，并考虑信息不确定性和噪声的影响，解决动力底盘在不规则作业地块下的全覆盖感知难题。

（2）建立新能源底盘机电一体化模型，精准解析底盘在不同作业条件下的响应特性，并获取底盘位姿、作业速度等关键作

业状态，解决动力底盘在不规则地块下的适应性建模难题。

（3）综合考虑不规则地块和可持续作业需求，提出无人作业路径规划与动力管理协同优化方法，制定多阶段路径规划策略，实现不规则地块全覆盖的精准路径规划。

实施方案：

（1）2024 年 10 月至 2025 年 08 月：重点研究多源信息融合驱动作业地块全覆盖感知、新能源底盘适应性建模与作业状态监测，形成科技报告。

（2）2025 年 09 月至 2025 年 12 月：重点研究无人作业路径规划与动力管理协同优化，构建适应不规则地块的新能源底盘路径规划系统，并开展相关验证。该阶段预期申请专利 2 件、软著 2 项，实现地块覆盖率≥95%、作业重复率≤5%、计算耗时≤10s，对所有研究成果进行归纳分析，完成结题报告，培养研究生 3 人。

（四）课题参加人员

类别	姓名	性别	学历	职称	出生年月	电话
主持人	卢家欢	男	博士 研究生	副教授		
主要参与人员	**姓名**	**性别**	**学历/职称**	**所属单位**	**任务分工**	
	罗锡文	男	教授	华南农业大学	技术总指导	
	曾山	男	研究员	华南农业大学	技术指导	
	王昱	女	副教授	华南农业大学	底盘建模	
	李杰浩	男	副教授	华南农业大学	协同优化	
	张闻宇	男	助理研究员	华南农业大学	路径规划	
	姜锐	男	副教授	华南农业大学	环境感知	
	杨禹锟	男	其他	华南农业大学	状态监测	
	陈纳	男	其他	华南农业大学	底盘建模	
	李城林	男	其他	华南农业大学	测试验证	
	邓棋瀚	男	其他	华南农业大学	协同优化	
	徐宇航	男	其他	华南农业大学	测试验证	

二、考核指标

（一）创新研究

开发针对不规则地块的新能源底盘无人作业路径规划系统，突破复杂地块条件全覆盖的高效路径规划算法瓶颈，确保覆盖率≥95%、作业重复率≤5%、计算耗时≤10 秒，并通过在代表性不规则地块区域进行田间试验，评估系统在实际作业环境中的适应性与稳定性，最终实现新能源底盘在不规则地块上的无人作业路径规划全覆盖。

（二）市场推广与应用前景

新能源底盘无人作业路径规划技术在市场推广和应用前景方面具有广阔的发展潜力。随着农业生产智能化和新能源化进程的加速，尤其是在不规则地块、山地、丘陵等复杂地形区域，传统油动农业机械的作业效率和能量利用率受限，而本项目技术能够有效应对这些地块的作业挑战，显著提升作业覆盖率、作业效率和能量利用率。此外，新能源底盘符合国家‘双碳’战略的环保要求，具备节能减排的优势，契合现代农业绿色发展的方向。通过本项目的技术攻关，未来可通过示范试点推广，结合国家农业补贴政策，推动该技术在精准农业和现代农业机械等多个领域的快速应用，助力农业生产的全面升级。

注：选择 2 个以上考核方向填写。

三、经费预算（2025年）

经费来源预算（单位：万元）		经费支出预算（单位：万元）	
科　目	预算数	科　目	预算数
1.专项资金拨款	30	一、直接费用	24
		1、设备费	0
		（1）购置设备费	0
		（2）试制设备费	0
		（3）设备改造费	0
		（4）设备租赁费	0
		2、材料费	10
		3、测试化验加工费	1
		4、燃料动力费	0
		5、差旅费/会议费/国际合作与交流费	5
		6、出版/文献/信息传播/知识产权事务费	3
		7、劳务费	4
		8、专家咨询费	1
		9、其他支出	0
		二、间接费用	6
经费来源预算合计	30	经费支出预算合计	30

注：经费预算保留到小数点后两位。间接费用预算不得超过30%。

四、计划任务书签定各方盖章及意见

甲方	单位名称	四川省农业科学院
	重点实验室负责人	
	意见	（单位公章） 2024年10月9日
乙方	承担单位	华南农业大学
	课题负责人	卢家欢
	电话及传真	020-38676975
	单位意见	同意 （单位公章） 2024年9月28日

2.5 主持：广州市基础与应用基础研究专题“启航”项目（C 类）

任务书编号：2025A04J3660

广州市科技计划项目

任务书

项目名称：	新能源农用底盘动力电源精细化管理与优化控制
承担单位：	华南农业大学
项目负责人：	卢家欢
计划类别：	基础研究计划
专题名称：	2025年度基础与应用基础研究专题
支持方向：	青年博士“启航”项目
组织单位：	华南农业大学
起止时间：	2025-01-01 至 2026-12-31
主管处室：	引进智力管理处（科技人才处）

广州市科学技术局制

二〇二五年

填写说明

1.任务书甲方为广州市科学技术局；乙方为项目承担单位；丙方为项目组织单位。

2.任务书基于项目申报书转换而成，请按照“广州科技GI（广州科技大脑）”提示在线填写核实，若存在不填写内容的栏目，请用“无”表示；任务书中的单位名称应为规范全称，并与单位公章一致。

3.乙方与合作单位的合作协议自动从项目申报书中读取，如需变化调整，须待任务书签订后，按要求及时办理重大变更。

4.乙方完成项目任务书在线填写，依次提交丙方和甲方审核确认后，按要求完成签章。具备电子签章条件的单位，在“广州科技GI（广州科技大脑）”完成任务书签署；不具备电子签章条件的单位，经与业务主管处室沟通对接后，可下载电子版项目任务书用A4纸双面打印装订签章，一式六份报甲方和丙方签章，其中甲方两份丙方两份，项目承担单位和项目负责人各一份。

5.涉密项目请在“广州科技GI（广州科技大脑）”下载项目任务书模板，按保密要求离线填写报送。

6.项目申报书是项目任务书填报的重要依据，未经甲方许可，乙方不得修改考核指标，调整主要研究内容。项目任务书将作为项目实施管理、验收结题和监督评估的重要依据。

7.项目任务书中的“备注”，包括重要的必须补充的内容。

8.“广州科技GI（广州科技大脑）”是项目管理过程中重要通知和文书的电子送达平台，电子送达与书面送达具有同等法律效力。为确保电子送达渠道畅通，乙方和项目负责人应及时更新维护“广州科技GI（广州科技大脑）”的单位和个人信息。

9.项目涉及科技伦理、科技安全（如临床研究、生物安全、信息安全等）和科技保密相关问题的，申报单位须严格执行国家有关法律法规和伦理原则，完成相关审查工作；项目负责人在项目任务书签订环节，须提供符合国家有关法律法规和伦理准则要求的审查

批准文件，项目承担单位负责审核批准文件的真实性和有效性。

一、项目基本信息

项目基本信息	项目名称	新能源农用底盘动力电源精细化管理与优化控制
	申请市财政科技经费	5(万元)
	研究期限	2（年）
项目摘要	本项目聚焦农业机械化、智能化与低碳化的迫切需求，旨在突破新能源农用底盘推广应用面临的动力电源管理技术瓶颈，拟研究新能源农用底盘动力电源精细化管理与优化控制，包括：①农用底盘作业工况特征提取与代表性工况谱构建；②适用于农用底盘作业工况的动力电源精细化建模；③新能源农用底盘动力电源多维状态估计与快速补能，探究兼顾效率、寿命及安全的精细化管控策略。研究成果为新能源农业机械动力电源高质量开发提供科学依据。	

二、项目单位情况

项目承担单位	单位名称	华南农业大学	统一社会信用代码	12440000455416563 4
	注册时间	1952-01-01	单位类型	高等院校
	注册地址	广东省广州市天河区五山路483号		
	办公地址（联系地址）	广东省广州市天河区五山路483号		
	联系人	姓名	夏杰	
		手机号码	[redacted]	
		电子邮箱	kjcgxk@scau.edu.cn	
	开户银行	广东广州工行五山支行		
	开户户名	华南农业大学		
	银行账号	3602002609000310520		

注：如果办公地址（联系地址）等相关信息有变更，项目单位应当在变更之日起三个工作日内告知我单位变更后的地址。

三、项目负责人信息

姓名	卢家欢	证件类型	身份证
证件号码	[redacted]	性别	男
出生日期	[redacted]	民族	汉族
国籍	中国	学历	博士研究生
学位	博士	学位授予国家（或地区）	中国
职务	教师	职称	副高级
所学专业	机械工程	手机号码	[redacted]
办公电话	020-85280783	电子邮箱	jhlu@scau.edu.cn

四、项目经费信息

本项目总投入：¥（5）万元，其中，市财政科技经费：¥（5）万元，自筹经费：¥（0）万元。

经费下达计划			
资金来源	小计	市财政科技经费	自筹经费
2025	5	5	0
总计	5	5	0

（单位：万元）

注：本专题纳入“包干制”，市财政科技经费按市科技计划项目经费“包干制”相关规定执行。

五、预期代表性成果

项目负责人在项目实施期内，以该项目作为资助项目获得以下5种情形之一且经费使用符合规定的，由组织单位审核后通过验收。

（一）项目实施期内，以第一作者/通讯作者发表论文1篇或以上（须标注资助项目编号）；

（二）项目实施期内，以第一完成人申请或授权专利、软件著作1项或以上；

（三）项目实施期内，获省级以上科技计划项目或人才项目支持1项或以上；

（四）项目实施期内，获省级以上科技奖励（含列入获奖团队成员名单）1项或以上；

（五）项目实施期内，获得职称晋升。

六、备注

专题补充约定条款：

甲方对未履行勤勉尽责义务的相关责任主体，自作出处理结论之日起，依照法律法规规定或任务书约定实施惩戒5年，取消相关责任主体申报市科技计划项目、申领市科技计划项目经费的资格。

预期代表性成果需在实施期内获得。

项目承担单位（乙方）及项目负责人承诺书

承诺书

本单位/本人作为广州市科技计划项目承担单位/项目负责人，将严格遵守广州市科技计划管理相关规定，严格履行自身责任，加强对项目组人员及合作单位的管理，在此郑重承诺：

（一）确保与本项目有关的全部材料真实、合法、有效，未侵犯其他方知识产权等权利，不存在多头申报、重复申报行为；

（二）严格遵守《广州市科技创新条例》《广州市科技计划项目管理办法》《广州市科技计划项目经费管理办法》《广州市科技计划科技报告管理办法》等相关规定，实施项目和经费管理；

（三）严格遵守国家、省、市关于科研诚信、科技伦理、科技安全（如临床研究、生物安全、信息安全等）和科技保密的有关法律、法规，相关政策以及各项规定，加强项目实施过程中的科研诚信、科技伦理、科技安全（如临床研究、生物安全、信息安全等）和科技保密管理，恪守科研道德准则。

如有违反，本单位/本人愿意接受相关部门做出的各项处理决定，包括但不限于终止项目、停拨经费、核减经费、追回经费，取消一定期限广州市科技计划项目申报资格，记入科研失信行为数据库，将不良行为向社会公开等。

项目承担单位：华南农业大学

日期：2024年12月25日

项目负责人：卢家欢

日期：2024年12月25日

电子送达确认书

告知事项	1.为便于本项目承担单位（受送达人）及时收到相关通知和文书，请受送达人知悉项目管理过程中重要通知和文书（如：项目验收结果通知书、配合结余资金审计通知书、项目终止通知书等）的送达方式是通过“广州科技GI（广州科技大脑）”平台（以下简称平台）电子送达。 2．确认的送达方式适用于行政执法全过程程序。 3．请受送达人在项目管理过程中及时、主动查看平台相应模块，以免错过相关通知和文书。 4．此电子送达方式，以发送方设备显示发送成功视为送达。但接收方证明其到达平台的日期与发送方对应系统显示发送日期不一致的，以受送达人证明到达平台的日期为准。
电子送达	受送达人同意：“广州科技GI（广州科技大脑）”是项目管理过程中重要通知和文书的电子送达平台，电子送达与书面送达具有同等法律效力。为确保电子送达渠道畅通，受送达人同意“广州科技GI（广州科技大脑）”作为电子送达平台。 “广州科技GI（广州科技大脑）”网站地址：https://gzsti.gzsi.gov.cn。
受送达人确认	我单位已阅读本确认书的告知事项，接受并确认了上栏送达方式。 受送达人：华南农业大学 2024年12月25日
备注	

任务书签署

甲乙丙三方根据《广州市科技计划项目管理办法》《广州市科技计划项目经费管理办法》《广州市科技计划科技报告管理办法》等有关文件规定，以及有关法律、政策和管理要求，签署本任务书。

签订地点：广州市越秀区

广州市科学技术局（甲方）：广州市科学技术局
局项目经办人：陈良　　联系电话：83124036
责任处室负责人：洪雪妍

2024年12月31日

项目承担单位（乙方）：华南农业大学
二级部门：华南农业大学工程学院
项目负责人：卢家欢
项目经费汇入账号
账户名：华南农业大学　　账号：360200260900031[illegible]520
开户银行：广东广州工行五山支行

2024年12月25日

组织单位（丙方）：华南农业大学
项目经办人：夏杰

2024年12月27日

2.6 主持：教育部国合联合实验室开放课题（其他）

编号：2024JIRLIMC04

节能与新能源汽车关键零部件智能制造与控制
教育部国际合作联合实验室

开放课题计划任务书

课题名称：	新能源农用车辆动力电池智能管控技术
课题负责人：	卢家欢
所在单位：	华南农业大学
邮政编码：	510642
通讯地址：	广东省广州市天河区五山路 483 号
工作邮箱：	jhlu@scau.edu.cn
联系电话：	[illegible]
起止年限：	2025 年 1 月—2026 年 12 月
申请日期：	2024 年 12 月

重庆理工大学

共享。

3、提交研究报告、发表的学术论文等成果材料复印件。

4、结题前来实验室作与开放课题研究内容密切相关的学术报告 1 次。

四、条款

1、课题负责人应按本任务书的内容认真开展相关研究工作，并按开放基金课题管理办法的有关规定按时报送有关材料。

2、取得的研究成果应该根据节能与新能源汽车关键零部件智能制造与控制教育部国际合作联合实验室开放基金管理办法的要求正确署名。

3、课题研究经费分期划拨至课题负责人所在单位，即课题正式立项后研究经费的 50%划拨至课题负责人所在单位，作为启动经费。其余 50%的课题研究经费在资助期满且考核指标完成后划拨至课题负责人所在单位。

4、划拨至课题负责人所在单位的经费，所在单位应严格按照任务书预算核准报销。

5、课题研究工作结束三个月内须提交开放课题结题报告，并提交经承担单位财务部门审查的财务报告（须加盖承担单位财务公章）。

6、每年的 12 月 31 日前应向实验室提交年度执行情况报告（格式参考“开放课题结题报告”）。

7、课题的执行期限为二年。

五、经费预算（单位：万元）

经费来源预算		经费支出预算	
科目	预算数	科目	预算数
1、开放课题经费	5.00	材料费	1.7
		差旅费	1
		测试化验加工费	0
		出版/文献/信息传播/知识产权事务费	2
		管理费	0.3
来源预算合计	5.00	**支出预算合计**	5.00

六、主要研究人员

主要研究人员（含项目负责人）:

姓名	学历	职 称	工作单位	项目分工	每年工作时间（月）	签名
卢家欢	研究生	副教授	华南农业大学	负责人	8	卢家欢
汤爱华	研究生	教授	重庆理工大学	电池建模	8	汤爱华
唐晓鹏	研究生	助理教授	香港岭南大学	电池建模	8	唐晓鹏
陈纳	本科	其他	华南农业大学	状态估计	8	陈纳
徐宇航	本科	其他	华南农业大学	优化充电	8	徐宇航
马建福	本科	其他	华南农业大学	工况构建	8	马建福
邓棋瀚	本科	其他	华南农业大学	算法验证	8	邓棋瀚

七、拨款账号

户名	华南农业大学
帐号	3602 0026 0900 0310 520
开户行	中国工商银行广州五山支行

八、审批表

课题负责人：卢家欢 2025年01月03日
课题负责人所在单位审查意见(盖章)： 盖章须为所在单位科研合同章 单位： 2025年01月03日
实验室审批意见(车辆工程学院代章)： 实验室负责人： 年 月 日
重庆理工大学科学技术研究院审批意见(盖章)： 负责人： 年 月 日

2.7 主持：中国北方车辆研究所委托项目（军工脱密项目）

0000D2024000000061376600-非密-1/14-5

中国北方车辆研究所
合同第AK2024F1168号
日期 2024.11.1

合同登记编号：

技术开发（委托）合同

项目名称：动力电池系统测试评价模型

委 托 方：中国北方车辆研究所

（甲方）

受托开发方：华南农业大学

（乙方）

填 写 说 明

一、“合同登记编号”由技术合同登记处填写。

二、技术开发合同是指当事人之间就新技术、新产品、新工艺和新材料及其系统的研究开发所订立的合同。技术开发合同包括委托开发合同和合作开发合同。

三、计划内项目应填写国务院部委、省、自治区、直辖市、计划单列市、地、市（县）级计划。不属于上述计划的项目此栏划（/）表示。

四、标的技术的内容、范围及要求

包括开发项目应达到的开发目的、使用范围、技术经济指标及效益情况。

五、研究开发计划

包括当事人各方实施开发项目的阶段进度、各个阶段要解决的技术问题、达到的目标和完成的期限等。

六、本合同的履行方式（包括成果提交方式及数量）

1、产品设计、工艺规程、材料配方和其他图纸、论文、报告等技术文件；

2、磁盘、磁带、计算机软件；

3、动物或植物新品种、微生物菌种；

4、样品、样机；

5、成套技术设备。

七、技术情报和资料的保密

包括当事人各方情报和资料保密义务的内容、期限和泄漏技术秘密应承担的责任。

八、本合同书中，凡是当事人约定认为无需填写的条款，在该条款填写的空白处划（/）表示。

注：本合同书标有※号的条款按填写说明填写

本合同由甲方委托乙方进行动力电池系统测试评价模型项目的技术开发（该项目属 / 计划※），并支付研究开发经费和报酬，乙方接受委托并进行此项研究开发工作。合同双方经过平等协商，在真实、充分地表达各自意愿的基础上，依据《中华人民共和国民法典》的规定，经协商一致，签订本合同，并由双方共同恪守。

一、标的技术的内容、范围、目标及要求※

本合同为甲方委托乙方进行动力电池系统测试评价模型的相关工作。

开展特种车辆储能装置的代表性实验测试工况构建的研究，以“精、简、短”的测试快速模拟特种车辆实际应用场景下的各类复杂环境和操作条件，并创建特种车辆储能装置评价关键技术，科学量化评估特种车辆实际应用场景下的电池综合性能，提高特种车辆储能装置测试效率、降低测试成本、缩短开发周期。

二、应达到的技术指标和参数

（1）特种车辆储能装置工况谱分析及性能敏感因子提取

开展特种车辆储能装置工况谱清洗及预处理，研究特种车辆储能装置在不同行驶速度、载重、路况和气候等条件下的工况谱演变规律；结合储能装置物理建模方法，研究基于储能装置工况谱的多元性能敏感因子提取机制，以此支撑储能装置代表性实验测试工况构建及评价体系研究。

（2）储能装置代表性实验测试工况构建及评价体系研究

结合数理统计手段，研究能够逼近储能装置复杂应用条件的代表性实验测试工况生成方法；创建面向储能装置综合性能的有效评价体系，基于所建评价体系，提出储能装置综合性能的多维对齐方法，研究以少量历史工况数据快速构造“精、简、短”的代表性实验测试工况，以此提高特种车辆开发过程的测试效率。

（3）代表性实验测试工况评价体系验证

以某型号特种车辆为例，采集多车海量实车工况下的电性能数据，建立工况谱数据库，并基于此针对性创建储能装置评价体系与代表性实验测试工况；随机以数据库中的某车作为验证组，针对该车储能装置开展代表性工况测试并计算综合性能值，再以其历史数据作为对照组，一并计算综合性能值，通过比对验证组与对照组的综合性能，以验证项目所提相关方法的有效性。

三、研究开发计划、进度及研发成果※

1、研究计划及主要节点

全部工作在一个月时间内完成。

2、成果

（1）性能敏感因子分析与提取报告（纸版或电子版）

（2）储能装置代表性实验测试工况构建与评价报告（纸版或电子版）

四、履行期限、地点和方式

履行期限：本合同自签订生效之日起，一个月内完成合同规定研究内容，达到技术指标，并交付相关的研究成果。

在 乙方所在地 （地点）履行。

本合同的履行方式：甲、乙双方确定，按以下标准及方法对本合同最终完成的研究开发工作成果进行验收：

以验收评审会通过，并满足相关技术指标为标志。评审专家由甲方确定。乙方按技术协议向甲方提供相应的研究成果和技术资料。

五、验收标准和方式

研究开发所完成的技术成果，达到了本合同第二条所列技术指标，乙方应按要求提供报告，采用会议评审方式验收，由 甲方 出具技术项目验收证明。

六、研究开发经费、报酬及其支付或结算方式

（一）研究开发经费是指完成项目研究开发工作所需的成本，报酬是指本项目开发成果的使用费和研究开发人员的科研补贴。

本项目研究开发经费和报酬（大写）：壹拾肆万伍仟元整（￥145,000），其中经费壹拾肆万伍仟元整（￥145,000），报酬 0 元。

（二）支付方式和条件：一次性支付。

壹拾肆万伍仟元整（￥145,000），支付时间和支付条件：全部任务完成并验收合格，乙方开具全部价款的增值税发票后，甲方于 3 个月内支付。

七、利用研究开发经费购置的设备、器材、资料的财产权属

利用研究开发经费购置的设备、器材、归属乙方。

八、风险责任的承担

在履行本合同的过程中，确因在现有水平和条件下难以克服的技术困难，导致研究开发部分或全部失败所造成的损失，风险责任由甲方承担 50 %，乙方承担 50 %。

本项目风险责任确认的方式：本合同的技术风险按双方共同认可的鉴定机构或其他组织或人员的鉴定结论为准进行认定。

认定技术风险的基本内容应当包括技术风险的存在、范围、程度及损失大小等，认定风险的基本条件是：

1、本合同项目在现有技术水平条件下具有足够的难度；

2、乙方在主观上无过错且经认定研究开发失败为合理的失败。

乙方发现技术风险存在并有可能致使开发失败或部分失败时，应在 7 日内通知另一方采取适当措施减少损失。逾期未通知或未采取适当措施而致使损失扩大的，应当就扩大的损失承担赔偿责任。

在本合同履行中，若作为研究开发标的技术已经由他人公开（包

括以专利权方式公开），一方应在 7 日内通知另一方解除合同，逾期未通知并致使另一方产生损失的，另一方有权要求予以赔偿。

九、甲乙双方的主要义务

1、甲方的主要义务

（1）甲方应按本合同的规定及时向乙方支付合同价款；

（2）乙方如申请国家资金援助，甲方应积极予以配合或协助；

2、乙方的主要义务

（1）乙方应保证合同价款特别是研发费用的合理使用，且不得将其挪为他用；

（2）乙方应按本合同的要求和进度完成各阶段研发工作，向甲方交付符合本合同规定的研发成果；

（3）在确定研发团队的人员组成及分工前，乙方应积极与甲方进行沟通，征询甲方的意见或建议；

（4）乙方应根据项目的复杂及紧迫程度以书面形式定期向甲方汇报研发进展情况，在进行重要试验或遇到关键问题时，应主动邀请甲方参与或及时通知甲方；

（5）乙方应按照甲方的要求，及时编制、修改与本合同研发成果有关的文件、资料或清单等并提供给甲方。

十、费用审计与质量督察

1、研发费用审计

乙方对研发费用应保证专款专用，甲方保留对乙方及其研发分包单位的研发费用支出情况进行审计的权利，乙方应予以配合。

乙方应按照甲方书面要求向甲方提供关于本方及其研发分包单位研发费用支出情况的财务凭证、报表及其它相关材料。

如果乙方不按上述要求配合甲方审计的，甲方有权不予支付相应的合同款项，如甲方已完成合同款项的支付，则甲方有权向乙方追索

相应的合同款项；如果经甲方审计发现存在重大问题或出入的，甲方有权通知乙方予以整改且暂缓支付相应的合同款项，并视整改后的二次审计结果情况，支付、调整或不予支付相应的合同款项，如甲方已完成合同款项的支付，则甲方有权向乙方追索相应的合同款项。

2、产品质量督察

甲方有权定期或不定期地对乙方研发质量进行督察，并视督察情况向乙方提出有关意见和建议。

乙方在进行科研开发的过程中应按照国家、行业等标准，建立健全质量保证体系，严格执行质量管理的相关规定，保证其研发成果符合国家、行业及甲方的要求。

乙方保证合同项下产品的检验、试验记录完整齐全，对生产过程形成的所有质量原始记录应妥善保存，定期归档。

十一、技术成果的归属和分享

1、甲方已按照本合同约定支付研究开发经费和报酬的，则本项目技术成果归属如下：

专利申请权：（1）

（1）甲方所有　（2）双方共有　（3）乙方所有

技术秘密的使用权、转让权：双方共有

其他约定：无

2、后续改进的技术成果归属：双方确定，甲方有权利用乙方按照本合同约定提供的研究开发成果，进行后续改进。由此产生的具有实质性或创造性技术进步特征的新的技术成果及其权属，由甲方（甲方/乙方/双方）享有。具体相关利益的分配办法如下：甲方占100%。

乙方有权在完成本合同约定的研究开发工作后，利用该项研究开发成果进行后续改进。由此产生的具有实质性或创造性技术进步特征

的新的技术成果，归 乙方 （甲方/乙方/双方）所有。具体相关利益的分配办法如下： 乙方占100% 。

3、侵权赔偿

（1）未经甲方同意，乙方不得在向甲方交付研究开发成果之前，自行将研究开发成果转让给第三方或让第三方知悉、使用或公开。

（2）未经甲方同意，乙方应确保其交付甲方的研发成果不存在任何侵犯或可能侵犯第三方权利的情形，如果一旦发生第三方指控侵权时，乙方应负责与第三方进行交涉，赔偿给甲方造成的损失，并承担由此引起的一切法律和经济责任。

十二、违约责任

1、甲方未按本合同第六条规定的期限向乙方支付合同款项的，每逾期一日，应按合同总额的0.1%向乙方支付逾期违约金，该逾期违约金的总额不得超过本合同总价的10%；逾期超过60日的，乙方有权解除合同；

2、乙方未按本合同第三条规定的进度和期限完成工作的，每逾期一日，应按合同总额的0.1%向甲方支付逾期违约金，该逾期违约金的总额不得超过本合同总价的10%；逾期超过60日的，甲方有权解除合同。

3、甲乙任何一方不履行本合同其他义务或其履行不符合本合同规定的，应及时履行该义务或采取合理的补救措施，并赔偿另一方因其违约行为而遭受的实际损失。

十三、保密条款

1、甲乙双方应对各自在本合同签订或履行过程中所获得的属于对方或与对方有关的信息和资料以及与本合同、本合同研发成果有关的信息和资料（“保密信息”）予以保密。

2、甲乙双方应采取所有合理、必要的手段和措施对保密信息予以保护，不得将保密信息用于本合同以外的任何目的，也不得向本合同之外的第三人提供、披露或允许其使用保密信息。

3、本合同项下的保密信息的保密期限为 / 年，在该保密期限内，甲乙双方的保密义务始终有效，不因本合同的终止或被解除而受到任何影响。

4、因违反保密条款而给对方造成损失的，应承担赔偿责任。

5、本次协作配套事项（任务）为 非密 级，合同文本为 非密 级，保密期限为/年，适用 A附件 （A附件《非密合同协作事项保密条款》/B附件《内部合同协作事项保密条款》/C附件《涉密合同协作事项保密条款》）。本合同中相关保密条款的内容如与A附件之内容有不一致的，涉及国家秘密的部分则以该附件为准。

十四、解决合同纠纷的方式

在履行本合同的过程中发生争议，双方当事人和解或调解不成，双方同意采取以下第 （二） 种方式解决。

（一）双方同意由 北京 仲裁委员会仲裁。

（二）双方约定向委托方所在地人民法院起诉。

十五、合同的变更或解除

本合同的变更或解除必须由双方协商一致，并以书面形式确定。

十六、不可抗力

因不可抗力致使本合同不能履行或者不能完全履行时，遇上不可抗力事件的一方，应在合理期限内书面通知合同相对方，最大限度减少因此可能给另一方造成的损失，并应在不可抗力事件发生后15天内，向合同另一方提供证明不可抗力发生的有效证明文件。由合同各方按事件对合同履行影响的程度协商决定是否解除合同，或者部分免除履行合同责任，或者延期履行合同。

十七、通讯地址条款

1、各方一致同意本合同载明的通讯信息（通讯地址、联系人、联系电话、电子邮箱）作为本合同相关文书邮寄送达的相关信息，如果上述信息发生变更的，应当立即书面通知对方。邮寄文书被签收之日即文件送达之日。

2、在按上述信息送达相关文书时，如出现文书无法送达或被退回情况时，发送文书一方应以电子邮件的方式将相关文书内容或内容摘要发送至本合同约定的电子邮箱，电子邮件发送之日（无论该电子邮件送达还是退回）即为该文书送达之日。

3、本条款适用于法院、仲裁等法律文书的送达。

4、本条款具有独立性，不受本合同终止或解除的影响。

十八、其它规定

1、未经一方书面同意，另一方不得将其在本合同项下的全部或部分权利或义务转让给第三方，否则，守约方有权随时解除合同并追究对方违约责任。

2、本合同的所有附件是本合同不可分割的一部分，与本合同具有同等法律效力。

十九、合同份数及生效时间

本合同一式五份，甲方执三份，乙方执二份。本合同自双方签字、盖章之日起生效。

委托方（甲方）	名称（或姓名）	中国北方车辆研究所（签章）			技术合同专用章 或 单位公章
	法定代表人	刘勇（签章）			
	委托代理人	（签章）			
	联系（经办）人	刘丹（签章）			
	住所（通讯地址）	北京市丰台区槐树岭4号院	邮政编码	100072	
	电话	010-83809589	传真	010-83803668	
	开户银行	工行北京长辛店支行			2024年11月7日
	银行账号	0200004809014403194			
	纳税人识别号	12100000400852739D			
受托开发方（乙方）	名称（或姓名）	华南农业大学（签章）			技术合同专用章 或 单位公章
	法定代表人	薛红卫（签章）			
	委托代理人	卢家欢（签章）			
	联系（经办）人	卢家欢（签章）			
	住所（通讯地址）	广东省广州市天河区五山路483号	邮政编码	510642	
	电话	020-85280783	传真		
	开户银行	中国工商银行广州五山支行			
	银行账号	3602 0026 0900 0310 520			
	纳税人识别号	124400004554165634			2024年11月5日

印花税票粘贴处

～～～～～～～～～～

登记机关审查登记栏：   经办人：　　技术合同登记处机关（专用章） 年　月　日

附件：保密条款

A 附件《非密合同协作事项保密条款》

合同事项不涉及国家秘密，但相关技术信息等涉及甲方利益，双方约定履行以下保密义务，有效期为 长期 （年或长期）：

1、乙方应只限定本合同中从事该项目工作的人员知悉有关信息，不得擅自扩大知悉范围。

2、甲方提供给乙方用于合同事项的各种技术资料，乙方不得擅自复制留存、转让出卖、宣传扩散等。

3、乙方持有的相关信息遭遇泄露，应及时报告甲方，并采取必要的补救措施。

2.8 主持：安克创新科技委托项目（其他）

No.安克旭创 20251113ZXGWFW5902*

技术咨询服务协议

本《技术咨询协议》（以下简称"本协议"）由以下双方于 2025-11-13 在深圳市南山区签订：

甲方：深圳市安克旭创科技有限公司

地址：广东省深圳市宝安区新安街道海富社区 45 区翻身路中心大厦厂房 G1515

乙方：华南农业大学

地址：广东省广州市天河区五山路 483 号

项目负责人：卢家欢

身份证号：

甲乙双方经过友好协商，本着平等互利，共同发展，优势互补的原则，依据相关法律法规的规定，就双方合作事宜达成如下协议：

一、 声明和保证

1.1 乙方是锂电池业务方面的专家，掌握足够的锂电池工作知识，并愿意为甲方提供技术咨询服务，甲方将按本协议的条款就【倚天剑 AIEMS-电池延寿】项目，委托乙方提供相关的技术咨询服务。

1.2 甲乙双方保证依据各自商务状况和经营能力，履行本协议约定的各项责任、权利和义务。

1.3 各方已清楚了解，本协议约定的服务合作是平等主体的民事合作关系，乙方或乙方安排的工作人员并非甲方的员工，且不享有甲方员工的权利义务，双方的法律关系也不适用《中华人民共和国劳动法》及相关法律。

1.4 乙方保证根据本协议将交付或提供的材料、分析、数据、程序和服务不侵犯任何第三方的知识产权，均符合甲方要求的种类和质量，且将由乙方合格人

4.2 除 4.1 条规定的服务费之外，乙方都无权为其根据本协议提供的服务获得任何直接或间接的其他补偿。

4.3 支付方式：服务费用合计 5 万元，甲方分两批支付：

1）合同签订后[10]个工作日内，且乙方提供等额有效发票后支付 50%费用，即 2.5 万元人民币；

2）乙方服务履行完毕并经甲方验收合格，且提供了等额有效增值税发票后[10]个工作日内，由甲方支付剩余 50%费用，即 2.5 万元人民币；

4.4 乙方指定的银行账户资料如下：

税号：124400004554165634

单位地址：广州市天河区五山路 483 号

开户银行：中国工商银行广州五山支行

银行帐号：3602 0026 0900 0310 520

五、 知识产权

5.1 甲方单独享有乙方提供服务中所形成的服务成果的知识产权以及相关权益，未经甲方书面同意，乙方不得将上述服务成果提供给任何第三方或将其用于本协议之外的其他目的。乙方保证对相关技术拥有合法有效的知识产权并拥有许可使用的权利（即未与第三方签订排他许可协议以及独占许可协议），保证采取积极、稳妥的措施维持所涉及的知识产权的有效性。同时，甲方利用乙方提交的服务工作成果所完成的新的技术成果，归甲方所有。

5.2 任何一方在未获得对方书面允许的情况下，不应以任何形式向任何第三方披露、泄露或提供从对方取得的保密资料。

六、 协议终止

6.1 协议任何一方可提前 30 天向对方发出书面通知的形式终止该协议，该

12.5 本合同壹式叁份，甲方执壹份，乙方执贰份，具有同等的法律效力。

12.6 本合同附件为本合同的组成部分，与本合同具有同等的法律效力。

12.7 本合同自甲方盖章、乙方盖章签字之日起生效。

附件 1:合作内容以及服务要求

附件 2:保密协议

附件 3：廉政共建协议

（以下无正文）

甲方：深圳市安克旭创科技有限公司

乙方：华南农业大学（盖章）

项目负责人：

2.9 主参：中国烟草总公司“揭榜挂帅”项目（A 类参与排 2）

计划文号：中烟办〔2023〕138 号
类　　别：“揭榜挂帅”
合 同 号：110202301004

中国烟草总公司烟草农机研发与应用领域“揭榜挂帅”项目计划项目合同

项 目 名 称：	丘陵山区烟草自动高速精准移栽机的研发与应用
所 属 榜 单：	丘陵山区烟草自动高速精准移栽机的研发与应用
委托单位（甲方）：	中国烟草总公司
承担单位（乙方）：	常州亚美柯机械设备有限公司
	华南农业大学
	云南农业大学
	贵州省山地农业机械研究所
	湖南省农业装备研究所
项目起止日期：	2024 年 1 月～2026 年 12 月

中国烟草总公司
二○二四年制

- 1 -

课题编号：110202301004　　**密　级：公开**

中国烟草总公司
“揭榜挂帅”计划项目课题任务书

课题名称（编号）：	烟草自动高速精准移栽机打窖机构关键部件设计及优化
课题负责人：	曾山
课题承担单位：	华南农业大学
项目名称（编号）：	丘陵山区烟草自动高速精准移栽机的研发与应用
所属榜单：	榜单二：丘陵山区烟草自动高速精准移栽机的研发与应用
项目牵头单位：	常州亚美柯机械设备有限公司
执行期限：	2024 年 01 月至 2026 年 12 月

中国烟草总公司
二〇二四年制

九、课题参加人员基本情况表

姓 名	性 别	出生年月	学历	职称	专业	工作单位	任务分工
曾　山	男	[illegible]	博士	研究员	农业机械化	华南农业大学	课题负责人
杨文武	男	[illegible]	博士	副教授	农业机械化工程	华南农业大学	任务负责人
卢家欢	男	[illegible]	博士	副教授	农业机械化工程	华南农业大学	行走机构设计
甄文斌	女	[illegible]	硕士	高级实验师	农业水土工程	华南农业大学	输送机构设计
梅伟丽	女	[illegible]	硕士	助理研究员	图书情报工程	华南农业大学	行走机构设计
王 昱	女	[illegible]	博士	副教授	农业机械化工程	华南农业大学	行走机构设计
陈海波	女	[illegible]	博士	正高级实验师	农业机械化工程	华南农业大学	控制机构设计
夏红梅	女	[illegible]	博士	副教授	农业机械化工程	华南农业大学	投苗机构设计
周云开	女	[illegible]	博士	讲师	农业机械化工程	华南农业大学	投苗机构设计
骈瑞琪	男	[illegible]	博士	讲师	林木遗传育种	华南农业大学	烟苗参数测定分析
李　捷	男	[illegible]	硕士	副教授	机械设计与制造	华南农业大学	机构改进及优化

课题经费来源表

<table>
<tr><td>课题承担单位</td><td colspan="2">华南农业大学</td><td>负责人</td><td>曾山</td></tr>
<tr><td>经费（万元）</td><td colspan="2">经费来源</td><td colspan="2">任务分工及里程碑考核指标分解</td></tr>
<tr><td rowspan="5">120.0</td><td>中国烟草总公司投入经费</td><td>120.0</td><td rowspan="5" colspan="2">任务分工：协助打塘式和打窖式烟草自动高速精准移栽机整机的研发与试制
里程碑 1：参与打窖/打塘、计亩和计数系统的核心部件研制；申请发明专利1件以上；
里程碑 2：参加打窖/打塘烟草移栽机关键部件改进及样机试验。发表核心期刊论文 1 篇以上。
里程碑 3：1）申请专利 1 项以上。2）发表核心期刊论文 1 篇以上。</td></tr>
<tr><td>自筹经费</td><td>0</td></tr>
<tr><td>其中：
1. 本单位自筹</td><td></td></tr>
<tr><td>2.（单位名称）投入经费</td><td></td></tr>
<tr><td>3.（单位名称）投入经费</td><td></td></tr>
</table>

签订合同各方：

委托单位（甲方）：中国烟草总公司（签章）

代表人（签字）：

项目经办人：　　2024年　4月　12日

单位地址：北京市西城区月坛南街 55 号（100045）

联系电话：010-63605920

项目第一承担单位（乙方）：常州亚美柯机械设备有限公司（签章）

2024 年　3 月 15 日

法定代表人或授权代表（签字）：

财务部门负责人（签字）：

户名、开户行及账号：常州亚美柯机械设备有限公司、中国银行常州分行营业部、552178107870

单位通信地址：江苏省常州市钟楼经济开发区樱花路 19 号

邮编：213023

项目联系人：徐小林

手机电话：

项目负责人（签字）：　　2024 年 3 月 15 日

手机电话：

项目第二承担单位（乙方）：华南农业大学　　（签章）

2024年 3 月 15 日

法定代表人或授权代表（签字）：

财务部门负责人（签字）：

户名、开户行及账号：华南农业大学、中国工商银行广州工行五山支行、3602002609000315 20

单位通信地址：广东省广州市天河区五山路 483 号

邮编：510642

项目联系人：　曾山

手机电话：

项目负责人（签字）：　　2024年 3 月 15 日

手机电话：

任务书签署

项目承担单位（甲方）：常州亚美柯机械设备有限公司（公章）

项目负责人（签字）：

单位地址：江苏省常州市钟楼经济开发区樱花路19号

邮编：213023

联系人：徐小林

联系电话：

年　月　日

课题承担单位（乙方）：华南农业大学（公章）

课题负责人（签字）：

单位地址：广东省广州市天河区五山路483号

邮编：510642

联系人：卢家欢

联系电话：

年　月　日

三、论文、著作等

3.1 检索证明

SCAULIB202519528

检索证明

根据委托人提供的论文材料，委托人**华南农业大学工程学院 卢家欢** 3 篇论文收录情况如下表。

序号	论文名称	发表刊物及发表的年月卷期/页码等	作者排名	论文等级	作者文中单位	收录情况	影响因子	中科院大类分区
1	Pineapple Detection with YOLOv7-Tiny Network Model Improved via Pruning and a Lightweight Backbone Sub-Network	REMOTE SENSING 出版年：2024 出版日期：AUG 卷期：16 15 页码：- 文献号：2805 文献类型：Article	通讯作者	A类	华南农业大学工程学院	SCI	IF2-year=4.1 IF5-year=4.8 （2024）	地球科学 2区 Top 期刊：否 （2025）
2	基于双曲正切函数的采摘机械臂滑模跟踪控制	华南农业大学学报 出版年：2025 出版日期：2024-12-31 17:37 卷期：46 02 页码：238-245 文献号： 文献类型：期刊论文	通讯作者	B类	华南农业大学工程学院	北大核心	无	无
3	动力电池数字孪生体设计及其全寿命电行为仿真	西南大学学报(自然科学版) 出版年：2024 出版日期：2024-12-06 卷期：46 12 页码：24-30	第一作者	C类	华南农业大学工程学院	北大核心	无	无
		文献号： 文献类型：期刊论文						

说明：论文等级和中科院大类分区按《华南农业大学学术论文评价方案（试行）》划分。

报告免责声明:如未盖章,报告无效

检索员：卢炳卫

华南农业大学图书馆

2025-07-29

SCAULIB202626115

检索证明

根据委托人提供的论文材料，委托人华南农业大学工程学院 卢家欢(学科类型:自然科学) 3 篇论文收录情况如下表。

序号	论文名称	发表刊物及发表的年月卷期/页码等	作者排名	论文等级	作者文中单位	收录情况	影响因子	中科院大类分区
1	Decoupling Analysis of Parameter Inconsistencies in Lithium-Ion Battery Packs Guiding Balancing System Design	ENERGIES 出版年：2025 出版日期：JUN 30 卷期：18 13 页码：- 文献号：3439 文献类型：Article	通讯作者	B 类	华南农业大学工程学院	SCI	IF2-year=3.2 IF5-year=3.1 （2024）	工程技术 4 区 Top 期刊：否 OA 期刊：是 标注：Mega-Journal （2025）
2	Predicting the Evolution of Capacity Degradation Histograms of Rechargeable Batteries Under Dynamic Loads via Latent Gaussian Processes	ENERGIES 出版年：2025 出版日期：JUL 2 卷期：18 13 页码：- 文献号：3503 文献类型：Article	共同通讯作者（倒数第一）	B 类	华南农业大学工程学院	SCI	IF2-year=3.2 IF5-year=3.1 （2024）	工程技术 4 区 Top 期刊：否 OA 期刊：是 标注：Mega-Journal （2025）
3	Analytical prediction of battery capacity degradation trajectories considering future operating condition variability	Chinese Journal of Electrical Engineering 出版年：2025 卷期： 页码：- 文献号： 文献类型：	共同通讯作者（倒数第一）		华南农业大学工程学院	在线发表	无	无

说明：论文等级和中科院大类分区按《华南农业大学学术论文评价方案（试行）》划分。

报告免责声明:如未盖章,报告无效

检索员：刘汝忠
华南农业大学图书馆
2026-03-13

3.2 以第一作者发表本专业论文情况

3.2.1 动力电池数字孪生体设计及其全寿命电行为仿真（C 类）

第 46 卷第 12 期　　西南大学学报（自然科学版）　　2024年12月
Vol. 46　No. 12　　Journal of Southwest University (Natural Science Edition)　　Dec.　2024

DOI：10.13718/j.cnki.xdzk.2024.12.003
卢家欢，徐宇航，邓棋瀚，等. 动力电池数字孪生体设计及其全寿命电行为仿真[J]. 西南大学学报(自然科学版)，2024，46(12)：24-30.

动力电池数字孪生体设计及其全寿命电行为仿真

卢家欢，　徐宇航，　邓棋瀚，　陈纳，
王昱，　曾山，　李杰浩

华南农业大学 工程学院，广州 510642

摘要：在“双碳”战略目标背景下，动力电池作为汽车、储能、农机、移动设备等领域的核心能量源，其重要性日益凸显. 动力电池的全寿命周期特性对用电设备的安全长寿运行至关重要，但准确获取这一特性需要耗费大量时间和资源，且难以模拟实际应用中的复杂工况. 为此，提出并设计了一种动力电池数字孪生体，可快速获取动力电池全寿命周期电行为仿真数据. 实验结果表明：该数字孪生体能精准模拟动力电池在实际应用中的容量衰减轨迹与衰后动态电压行为，为动力电池全生命周期快速模拟及其管理系统开发设计提供模型基础.

关　键　词：锂离子电池；老化；数字孪生
中图分类号：TM912　　**文献标志码**：A
文 章 编 号：1673-9868(2024)12-0024-07
开放科学(资源服务)标识码(OSID)：

Design of a Battery Digital Twin and Its Full-Lifecycle Electrical Behavior Simulation

LU Jiahuan，　XU Yuhang，　DENG Qihan，
CHEN Na，　WANG Yu，　Zeng Shan，　LI Jiehao

College of Engineering，South China Agricultural University，Guangzhou 510642，China

Abstract：In the context of the "Dual Carbon" strategy，batteries have become increasingly important as a core energy source in fields such as automobiles，energy storage，agricultural machinery，and mobile devices. The full life cycle characteristics of batteries are crucial for the safe and long-term operation of electric equipment. However，accurately obtaining these characteristics requires significant time and re-

收稿日期：2024-09-30
基金项目：国家自然科学基金青年基金项目(52407246)；四川省农业科学院开放课题(TFSZHH1001)；广西重点研发计划项目(桂科AB21220058)；广西科技创新基地建设类项目(桂科 ZY22096023).
作者简介：卢家欢，博士，副教授，主要从事新能源装备动力电源管理研究.

sources，and it is difficult to simulate the complex working conditions encountered in real-world applications. To address this，this paper proposes and designs a digital twin of the battery，which can quickly generate the simulation data of the whole life cycle electrical behavior of battery. Experimental results show that this digital twin can accurately simulate the capacity degradation trajectory and post-degradation dynamic voltage behavior of batteries in practical applications，providing a model foundation for rapid life cycle simulations and the development of battery management systems.

Key words：lithium-ion battery；degradation；digital twin

在我国“双碳”战略目标的推动下，以锂离子电池为代表的动力电池凭借无污染、高比能、快速响应等优势，迅速成为移动电子设备、电动汽车、储能电站等重要领域的核心能量源[1-3]. 动力电池全寿命周期内的特性变化对于这些应用的稳定性和长效性至关重要，因此，精准掌握动力电池全寿命周期特性已成为新能源系统设计的关键[4-5].

然而，动力电池的性能受到时间、工况和环境等多种因素的综合影响，其工作行为表现出高度的非线性和不确定性，使得准确预测全寿命周期内的电池性能变化成为重大挑战[6]. 现有的老化测试与实验方法往往耗时长、资源消耗大，且难以模拟实际应用中的复杂工况，这在很大程度上限制了动力电池性能优化和寿命管理的发展[7-10].

近年来，数字孪生技术在航空航天制造等领域崭露头角，其核心在于创建物理系统的数字副本，通过仿真技术生成大量数据，以掌握其全寿命周期内的性能演变规律[11-15]. 将这一技术引入动力电池领域，有望突破传统测试方法的局限，快速、高效地模拟电池的老化轨迹与动态行为，为电池管理系统开发与性能优化提供强有力的支持.

本文提出并设计了一种动力电池数字孪生体，旨在通过仿真技术快速模拟动力电池的老化特性，快速探讨其全寿命周期内的性能演变规律，该设计不仅可提高电池寿命管理的精度和效率，还为动力电池的开发与应用提供了重要的技术支撑.

1　动力电池数字孪生体设计

动力电池数字孪生体设计包括底层模型设计与界面设计. 底层模型设计的主要内容是构建用以描述动力电池全寿命周期老化行为的模型集合，界面设计的主要内容是创建用户与底层模型的交互媒介.

1.1　底层模型设计

动力电池的容量保持率 η 定义为：

$$\eta=\frac{Q}{Q_0}\times 100\% \tag{1}$$

式中：Q_0 为动力电池出厂时的最大可用容量；Q 为动力电池老化后的最大可用容量.

动力电池全寿命周期内的容量衰减轨迹采用双指数模型[16] 进行解析：

$$Q=p_1\cdot \mathrm{e}^{p_2\cdot x_{\mathrm{cyc}}}+p_3\cdot \mathrm{e}^{p_4\cdot x_{\mathrm{cyc}}} \tag{2}$$

式中：p_1，p_2，p_3 和 p_4 为双指数模型参数；x_{cyc} 为循环次数，需要时允许通过安时吞吐量 x_{ah} 表示. x_{cyc} 计算公式如下：

$$x_{\mathrm{cyc}}=q_1\cdot {x_{\mathrm{ah}}}^2+q_2\cdot x_{\mathrm{ah}}+q_3 \tag{3}$$

式中：q_1，q_2 和 q_3 为模型参数.

动力电池电压行为依赖于老化程度，因此可以抽象形式表示为：

$$U_t = g(\boldsymbol{z}(x)) \tag{4}$$

式中：U_t为动力电池端电压，可采用抽象函数$g(\cdot)$表示；$\boldsymbol{z}$为U_t的决定性参数向量，依赖于x(x可为x_{cyc}或x_{ah}).

为了兼顾精度与运算效率，动力电池全寿命周期内的电压行为通过双极化等效电路模型[17-18]进行描述(图1)：

$$\begin{cases} \boldsymbol{z}(x) = [U_{ocv}, R_0, R_{p,1}, \tau_{p,1}, R_{p,2}, \tau_{p,2}] \\ U_t = U_{ocv} - I \cdot R_0 - U_{p,1} - U_{p,2} \\ \tau_{p,1} \cdot \dot{U}_{p,1} = I \cdot R_{p,1} - U_{p,1} \\ \tau_{p,2} \cdot \dot{U}_{p,2} = I \cdot R_{p,2} - U_{p,2} \end{cases} \tag{5}$$

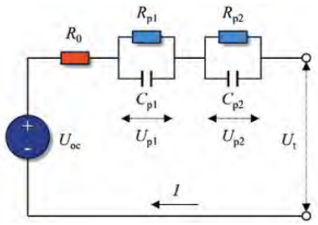

图1 动力电池双极化模型示意图

式中：I为动力电池工作电流；U_{ocv}为开路电压；R_0为欧姆内阻；$U_{p,1}$和$U_{p,2}$为双极化电压；$R_{p,1}$和$R_{p,2}$为双极化电压对应的极化内阻；$\tau_{p,1}$和$\tau_{p,2}$为双极化电压对应的时间常数. U_{ocv},R_0,$R_{p,1}$,$R_{p,2}$,$\tau_{p,1}$,$\tau_{p,2}$构成依赖于x的决定性参数向量，通过求解以下优化问题获得：

$$\hat{\boldsymbol{z}} = \arg\min_{\boldsymbol{z}} \sqrt{\frac{\sum_{i=1}^{M} (U_{t,i} - \hat{U}_{t,i})^2}{M}} \tag{6}$$

式中：$\hat{U}_t$为双极化等效电路模型输出的端电压；M为采样数；$\hat{\boldsymbol{z}}$为决定性参数向量的辨识值. 采用高斯过程回归建立x与决定性参数向量分量z之间的关系：

$$z = f(x) + \varepsilon, \varepsilon \sim N(0, \sigma^2) \tag{7}$$

式中：$f(\cdot)$为x与决定性参数向量分量z之间的潜在关系；ε表示均值为0、方差为σ^2的白噪声. z的先验分布可以根据高斯过程[19-20]定义为：

$$z \sim N(0, \boldsymbol{K}(X, X) + \sigma^2 \boldsymbol{E}) \tag{8}$$

式中：$\boldsymbol{E}$为单位矩阵；$\boldsymbol{K}(X, X)$为协方差矩阵. $\boldsymbol{K}(X, X)$每个位置对应的元素值可通过核函数$k(\cdot)$计算：

$$\begin{bmatrix} k(x_1, x_1) & k(x_1, x_2) & \cdots & k(x_1, x_n) \\ k(x_2, x_1) & k(x_2, x_2) & \cdots & k(x_2, x_n) \\ \vdots & \vdots & & \vdots \\ k(x_n, x_1) & k(x_n, x_2) & \cdots & k(x_n, x_n) \end{bmatrix} \tag{9}$$

式中核函数$k(\cdot)$取平方指数核函数，依赖于参数$\boldsymbol{s}$. 参数$\boldsymbol{s}$通过求解以下优化问题获得：

$$\hat{\boldsymbol{s}} = \arg\max_{\boldsymbol{s}} \log p(z \mid X, \boldsymbol{s}) \tag{10}$$

式中：$p(\cdot)$为边际似然函数，$\hat{\boldsymbol{s}}$为参数$\boldsymbol{s}$的辨识值.

本文以某锂离子电池为例初始化底层模型参数，该电池标称容量为2.6 Ah，上下截止电压分别为4.2 V和2.75 V，最大充放电电流分别为1.3 A和5.2 A.

1.2 界面设计

针对动力电池全寿命周期老化特性，本文设计了如图2所示的动力电池数字孪生体架构及其全寿命电行为仿真流程，以指导界面的友好设计. 根据该流程，用户首先按需选择电池材料体系来构建数字孪生体，例如镍钴锰三元体系、磷酸铁锂体系或其他材料体系. 在确定材料体系后，用户还需要根据应用背景定义动力电池数字孪生体期望经历的老化激励方式，例如期望以累计循环次数或累计安时吞吐量作为老化激

励．为了引导数字孪生体的后续仿真，若选择以累计循环次数作为老化激励，用户需要进一步量化动力电池未来可能经历的标准充放电工况下的总循环次数；若选择以累计安时吞吐量作为老化激励，用户则需要进一步量化动力电池在未来应用可能达到的安时吞吐总量．为了适应动力电池行业的快速发展，所设计的数字孪生体支持更新电池材料体系库与老化激励方式．在完成老化激励设置后，用户可以进行动力电池未来的老化轨迹仿真，可视化所选老化激励方式(即累计循环次数或累计安时吞吐量)与容量或容量保持率之间的关系．不仅如此，在获得详细的老化轨迹后，用户还可以进一步模拟动力电池沿该轨迹老化后的电压行为．具体而言，用户可以给定任意电流激励(包括恒定电流激励与动态电流激励)，然后计算老化后动力电池在面对该种电流激励时所产生的端电压响应．所设计的数字孪生体还支持将仿真所得的动力电池老化轨迹数据与电压行为数据导出，以便用户开展更深入的研究与分析．

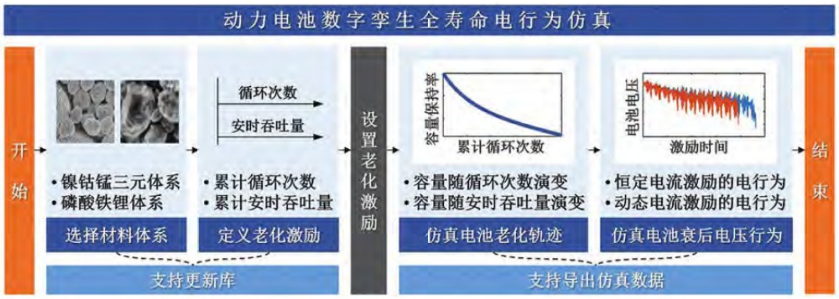

图 2　动力电池数字孪生体架构及其全寿命电行为仿真流程

根据上述应用操作流程，本文分别针对电池老化轨迹仿真模块与老化后电压行为仿真模块设计了相应界面(图 3、图 4)，以便用户操作与展示．

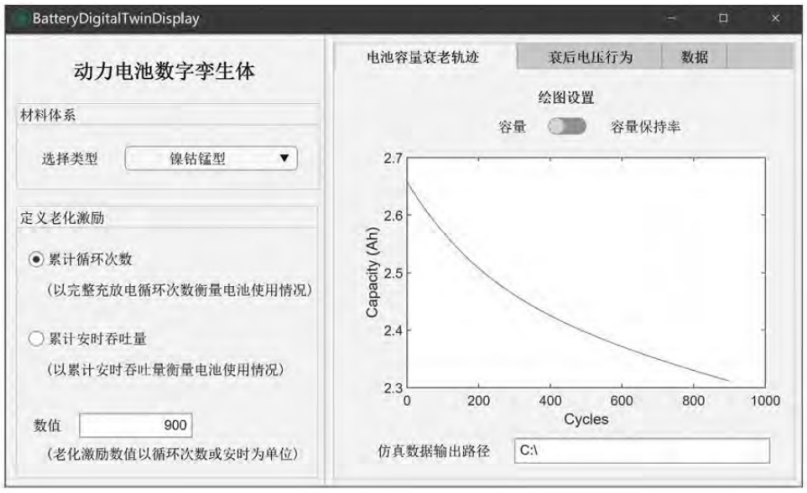

图 3　动力电池老化轨迹仿真模块应用界面

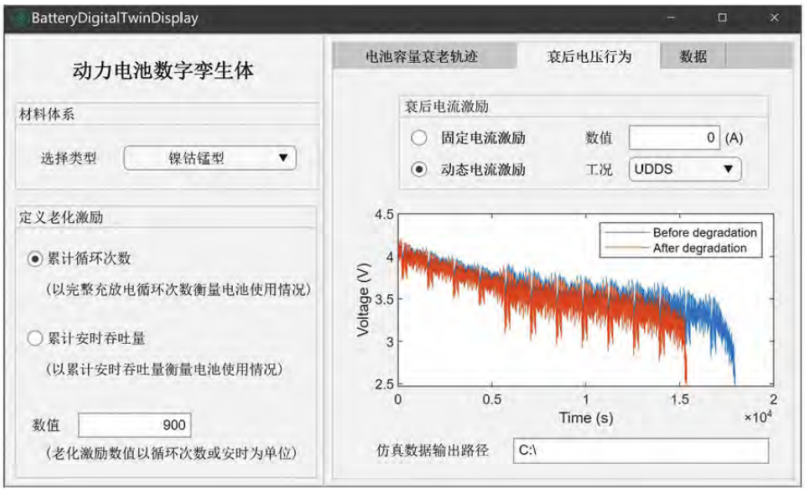

图4 动力电池衰后电压行为仿真模块应用界面

2 动力电池全寿命周期特性仿真

动力电池数字孪生体能够实现全寿命周期老化特性仿真，包括容量衰老轨迹、衰后开路电压以及衰后动态电压行为等仿真.

2.1 容量衰老轨迹仿真

给定期望经历的老化激励，动力电池数字孪生体支持模拟相应激励下的容量衰老轨迹. 为了进行验证，本文以累计经历1 000次循环和累计经历3 000 Ah吞吐量为例，分别模拟相应老化激励方式下的容量衰老轨迹，结果如图5、图6所示.

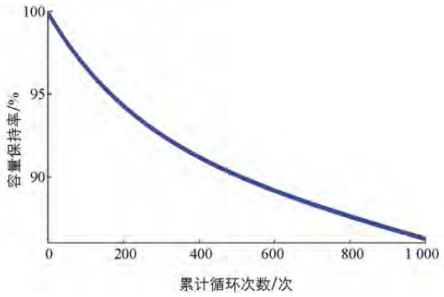

图5 经历1 000次循环的动力电池容量衰老轨迹仿真

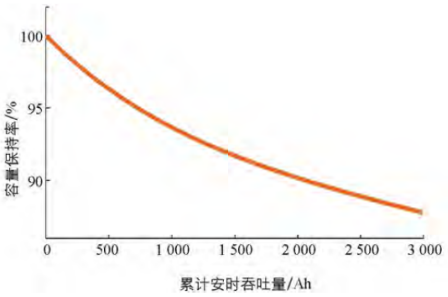

图6 经历3 000 Ah吞吐后的动力电池容量衰老轨迹仿真

图5、图6结果表明，数字孪生体能够有效模拟以累计循环次数和安时吞吐量作为老化激励的非线性容量衰退特性.

2.2 衰后开路电压仿真

全电量区间开路电压曲线反映动力电池热力学特性，是动力电池全寿命周期管理中的必要信息. 一般而言，获取高质量的开路电压曲线依赖于足够长的静置时间或足够小的电流激励，因此在实际开发中

极具挑战.

本文以累计经历 1 000 次循环为老化激励、以 0.05 C 为恒定电流激励进行动力电池衰后开路电压仿真，结果如图 7 所示. 图 7 结果表明，数字孪生体能够有效模拟动力电池关于电量的开路电压曲线. 老化激励前后的仿真结果对比表明，数字孪生体还能够模拟动力电池开路电压的衰老特性.

2.3　衰后动态电压行为仿真

动力电池在实际应用中往往需要满足复杂多变的功率需求，所以通常经历动态电流激励. 因此，掌握动力电池对动态电流激励的动态电压响应行为对于高安全、长寿命用电至关重要. 获取各类潜在电流激励下的动态电压响应曲线依赖于大量的充放电测试，因此在实际开发中难以实现.

本文以累计经历 1 000 次循环为老化激励、以中国轻型汽车行驶工况(CLTC)[21]为动态电流激励进行动力电池衰后动态电压响应仿真，结果如图 8 所示. 图 8 结果表明，数字孪生体能够有效模拟动力电池对于动态电流激励的电压行为特性. 老化激励前后的仿真结果对比表明，数字孪生体还能够模拟动力电池动态电压行为的衰老特性.

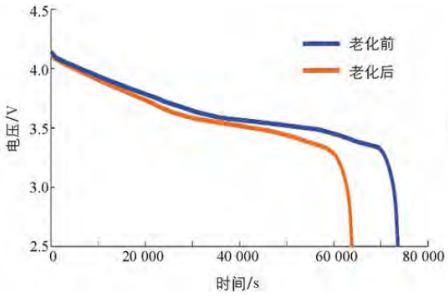

图 7　经历 1 000 次循环前、后的动力电池开路电压特性仿真

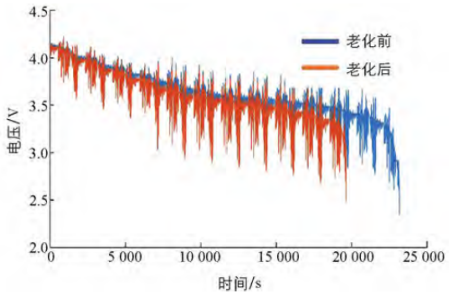

图 8　经历 1 000 次循环前、后对动力电池 CLTC 工况激励的电压响应行为仿真

3　结论

掌握动力电池全寿命周期特性是确保新能源系统装备健康长寿设计的关键前提. 然而，动力电池全寿命周期测试通常耗费大量时间和资源，并且难以充分模拟实际应用中的复杂工况. 本文设计并验证了一种动力电池的数字孪生体，能够模拟其全寿命周期内的电行为. 通过模拟与实际测试对比，数字孪生体不仅能够精确反映电池的容量衰减轨迹，还能够准确再现电池在衰退后的动态电压响应特性. 该方法有效解决了传统电池测试耗时长、资源消耗大的问题，为动力电池全生命周期建模及仿真提供了全新工具. 通过本研究，数字孪生技术为动力电池老化过程的快速评估与预判提供了高效手段，能够广泛应用于电池设计、管理系统开发及多种复杂工况下的电池优化. 此外，所提出的数字孪生体设计框架具有较强的扩展性，不仅能够适应不同类型的电池系统及应用场景，还具备进一步集成更多材料体系的潜力，以适应行业快速发展的需求. 未来的研究可进一步结合更复杂的工况仿真，分析电池系统的多参数耦合行为，并逐步扩展孪生体至多样化的材料体系，以提升动力电池全生命周期预测的精度和适用范围.

参考文献：

[1]　李嘉鑫，李鹏钊，王苗，等. 锂离子电池热管理技术研究进展 [J]. 过程工程学报，2023，23(8)：1102-1117.

[2]　赵延鹏，王峰，杨永发，等. 基于作业工况和退役锂离子电池的电动拖拉机电源系统优化 [J]. 中国农机化学报，2022，

43(2):104-111.
[3] 叶宇剑,袁泉,汤奕. 面向双碳目标的交通网-电网耦合网络中电动汽车负荷低碳优化方法[J]. 中国电力,2023,56(5):72-79.
[4] LU J H, XIONG R, TIAN J P, et al. Deep Learning to Predict Battery Voltage Behavior after Uncertain Cycling-Induced Degradation[J]. Journal of Power Sources, 2023, 581: 233473.
[5] 王桀,熊瑞,穆浩. 温度和老化意识融合驱动的电动车辆锂离子动力电池电量和容量协同估计[J]. 电工技术学报,2020,35(23):4980-4987.
[6] 熊瑞. 动力电池管理系统核心算法[M]. 2版. 北京:机械工业出版社,2022.
[7] 梁新成,张志冬,黄国钧. 锂电池的电化学建模研究[J]. 西南大学学报(自然科学版),2023,45(3):214-221.
[8] 王澎,窦悦珊,赵星,等. 高镍三元锂离子电池衰减机制研究展望[J]. 西南大学学报(自然科学版),2022,44(3):29-43.
[9] 张志刚,张涛,汤爱华,等. 车用锂电池健康状态下快充方法研究综述[J]. 西南大学学报(自然科学版),2022,44(2):194-206.
[10] HU X S, XU L, LIN X K, et al. Battery Lifetime Prognostics[J]. Joule, 2020, 4(2): 310-346.
[11] LU J H, XIONG R, TIAN J P, et al. Deep Learning to Estimate Lithium-Ion Battery State of Health Without Additional Degradation Experiments[J]. Nature Communications, 2023, 14(1): 2760.
[12] WANG W W, WANG J, TIAN J P, et al. Application of Digital Twin in Smart Battery Management Systems[J]. Chinese Journal of Mechanical Engineering, 2021, 34(4): 12-30.
[13] 胡权. 数字孪生体:第四次工业革命的通用目的技术[M]. 北京:人民邮电出版社,2021.
[14] WU B, WIDANAGE W D, YANG S C, et al. Battery Digital Twins: Perspectives on the Fusion of Models, Data and Artificial Intelligence for Smart Battery Management Systems[J]. Energy and AI, 2020, 1: 100016.
[15] 李海峰,王炜. 数字孪生教育应用的教学模式探究——基于美国、瑞士和芬兰数字孪生教育应用的案例分析[J]. 现代教育技术,2021,31(7):12-20.
[16] LIANG J Y, LIU H, XIAO N C. A Hybrid Approach Based on Deep Neural Network and Double Exponential Model for Remaining Useful Life Prediction[J]. Expert Systems with Applications, 2024, 249: 123563.
[17] LI F, ZUO W, ZHOU K, et al. State-of-Charge Estimation of Lithium-Ion Battery Based on Second Order Resistor-Capacitance Circuit-PSO-TCN Model[J]. Energy, 2024, 289: 130025.
[18] LAI X, GAO W K, ZHENG Y J, et al. A Comparative Study of Global Optimization Methods for Parameter Identification of Different Equivalent Circuit Models for Li-Ion Batteries[J]. Electrochimica Acta, 2019, 295: 1057-1066.
[19] LI X Y, WANG Z P, YAN J Y. Prognostic Health Condition for Lithium Battery Using the Partial Incremental Capacity and Gaussian Process Regression[J]. Journal of Power Sources, 2019, 421: 56-67.
[20] LI X Y, YUAN C G, LI X H, et al. State of Health Estimation for Li-Ion Battery Using Incremental Capacity Analysis and Gaussian Process Regression[J]. Energy, 2020, 190: 116467.
[21] LIU Y, WU Z X, ZHOU H, et al. Development of China Light-Duty Vehicle Test Cycle[J]. International Journal of Automotive Technology, 2020, 21(5): 1233-1246.

责任编辑 张枸

3.3 以通讯作者发表本专业论文情况

3.3.1 Pineapple Detection with YOLOv7-Tiny Network Model Improved via Pruning and a Lightweight Backbone Sub-Network（A 类）

remote sensing

MDPI

Article

Pineapple Detection with YOLOv7-Tiny Network Model Improved via Pruning and a Lightweight Backbone Sub-Network

Jiehao Li [1,2], Yaowen Liu [2], Chenglin Li [2], Qunfei Luo [2] and Jiahuan Lu [2,*]

[1] State Key Laboratory of Robotics and Systems, Harbin Institute of Technology, Harbin 150001, China; jiehao.li@ieee.org
[2] Key Laboratory of Key Technology on Agricultural Machine and Equipment, Ministry of Education, College of Engineering, South China Agricultural University, Guangzhou 510642, China
* Correspondence: jhlu@scau.edu.cn

Abstract: High-complexity network models are challenging to execute on agricultural robots with limited computing capabilities in a large-scale pineapple planting environment in real time. Traditional module replacement often struggles to reduce model complexity while maintaining stable network accuracy effectively. This paper investigates a pineapple detection framework with a YOLOv7-tiny model improved via pruning and a lightweight backbone sub-network (the RGDP-YOLOv7-tiny model). The ReXNet network is designed to significantly reduce the number of parameters in the YOLOv7-tiny backbone network layer during the group-level pruning process. Meanwhile, to enhance the efficacy of the lightweight network, a GSConv network has been developed and integrated into the neck network, to further diminish the number of parameters. In addition, the detection network incorporates a decoupled head network aimed at separating the tasks of classification and localization, which can enhance the model's convergence speed. The experimental results indicate that the network before pruning optimization achieved an improvement of 3.0% and 2.2%, in terms of mean average precision and F1 score, respectively. After pruning optimization, the RGDP-YOLOv7-tiny network was compressed to just 2.27 M in parameter count, 4.5×10^9 in computational complexity, and 5.0MB in model size, which were 37.8%, 34.1%, and 40.7% of the original YOLOv7-tiny network, respectively. Concurrently, the mean average precision and F1 score reached 87.9% and 87.4%, respectively, with increases of 0.8% and 1.3%. Ultimately, the model's generalization performance was validated through heatmap visualization experiments. Overall, the proposed pineapple object detection framework can effectively enhance detection accuracy. In a large-scale fruit cultivation environment, especially under the constraints of hardware limitations and limited computational power in the real-time detection processes of agricultural robots, it facilitates the practical application of artificial intelligence algorithms in agricultural engineering.

Keywords: object detection; neural network; YOLOv7-tiny; lightweight; model pruning; pineapple detection

Citation: Li, J.; Liu, Y.; Li, C.; Luo, Q.; Lu, J. Pineapple Detection with YOLOv7-Tiny Network Model Improved via Pruning and a Lightweight Backbone Sub-Network. *Remote Sens.* **2024**, *16*, 2805. https://doi.org/10.3390/rs16152805

Academic Editors: Mohammad Awrangjeb and Pedro Melo-Pinto

Received: 4 June 2024
Revised: 23 July 2024
Accepted: 26 July 2024
Published: 31 July 2024

1. Introduction

Pineapple, a tropical and subtropical fruit celebrated for its distinction, holds the fourth position in global production rankings, with China being a significant contributor. The Guangdong Province, with its extensive cultivation, covering 10% of the province's total 38,960 hectares, stands as the primary pineapple-producing region in China, predominantly focused in Zhanjiang, which is responsible for over 90% of the national output [1–4]. Despite this, domestic pineapple harvesting remains heavily manual, attributed to the scattered planting patterns and the fruit's unique surface, which hinders the adoption of mechanized methods [5–7]. To enhance the efficiency of harvesting and reduce dependence on human labor, the development of mechanized harvesting technology is particularly

important. Mechanized harvesting mainly relies on two key technologies: visual object detection and machine-gripping path control. This article will conduct an in-depth study of lightweight visual network models [8–10].

In the area of technologies for vision, based on monocular vision, Li Bin et al. demonstrated that the approximate centroid of the pineapple area is found using mathematical morphology techniques and cluster analysis, which offers a practical technical solution for field fruit recognition by robots that pick pineapples [11]. He Dongjian et al. performed image binarization and segmentation on pineapple images and determined the fruit centroid position from the target pixel point coordinates, to create an automatic pineapple harvester based on binocular vision. Nevertheless, there are certain drawbacks to these conventional machine-vision recognition techniques, in terms of picking operations' duration and accuracy of recognition [12].

Fruit identification technology built on deep learning and machine learning algorithms has gained a lot of traction in recent years [13–16]. Numerous academics have used it in their specialized fields of fruit production, with impressive outcomes. For instance, Xu Lifeng et al. presented a DenseNet-based enhanced fruit target detection framework that increased the accuracy of clustered fruit detection by combining high-level and low-level semantic information and creating a feature pyramid structure. In the three data sets of apples, mangoes, and apricots, the framework's average detection speed is greater than 40 FPS; the corresponding F1 values are 92.0%, 92.8%, and 83.1% [17]. As network performance advances, there are growing numbers of network layers, resulting in higher demand for processing power and storage capacity and restricting their utilization in contexts with limited resources. Therefore, the key to effectively utilizing pineapple-picking robots is to render lightweight the network model. Against this backdrop, the YOLO (you only look once) series of algorithms, as a popular choice for object detection, has undergone continuous iteration and improvement. From the innovative proposal of YOLOv1 to the network structure optimization of YOLOv2 and then to the introduction of multi-scale prediction in YOLOv3 as well as the integrated innovations of YOLOv4, each iteration has enhanced detection speed and accuracy while also exploring lightweight model designs. In particular, YOLOv7-tiny, as a lightweight version of YOLOv7, has been specially optimized for environments with limited resources by reducing the number of network layers and parameters. It maintains efficient detection performance while effectively controlling the model size. Zhao Pengfei et al. proposed a network model based on adding a DBB (diverse branch block) module to the backbone and combining it with the SimAM attention mechanism to improve YOLOv7-tiny, which is used to detect sweet pepper fruits in farmland environments. Under identical experimental conditions, the mean average precision was 2.21% higher and the model size was 5.4 MB smaller than the original network [18]. Liang Xiaoting et al. proposed a real-time detection method for tomato surface defects that leverages model pruning. They implemented channel and layer pruning techniques to streamline the YOLOv4 network model, resulting in a substantial reduction in model size by 232.40 MB and a decrease in inference time by 10.11 ms. Additionally, they managed to elevate the mean average precision from 92.45% to 94.56% [19]. Kong Yinghui et al. introduced a sophisticated model for flower recognition under complex conditions, based on MobileNets, alongside a model pruning approach. Specifically, they applied the L2 norm method to prune the model, achieving a significant reduction in model size from 46.2 MB to 24.3 MB, which was approximately 50% compression [20].

Considering the significant advantages of model pruning in simplifying model structures and enhancing recognition accuracy over traditional module replacement techniques, this paper optimizes the model through module replacement, followed by pruning, to further refine the substituted model. Initially, a pineapple dataset was constructed. The original YOLOv7-tiny network's backbone was replaced with ReXNet, and lightweight GSConv modules were integrated into the neck network, along with the incorporation of a decoupled head in the detection network that enhanced the model's convergence speed.

The model was then trained, to obtain the pre-pruning version. Subsequently, a group-level pruning method was applied, to remove redundant parameters from the network, followed by fine-tuning, to restore the model's accuracy, ultimately yielding an efficient model that had been compressed, in terms of parameter count, computational requirements, and model size [21]. These improvements were designed to maintain detection accuracy while significantly reducing the model's resource consumption, to meet the application needs of pineapple-picking robots.

The main contributions of this paper are summarized as follows:

- To enhance the flexibility and generalization of the visual model, we collected and constructed a dataset containing images of pineapples in various environments at the pineapple plantation base in Xuwen County, Zhanjiang City, Guangdong Province.
- By replacing the main trunk network, introducing the lightweight GSConv module, and incorporating the decoupled head structure, improvements were made to the YOLOv7-tiny model, enhancing its detection accuracy and efficiency.
- By applying the group-level pruning method based on the analysis of the dependency graph, the model was pruned. This effectively reduced the model's complexity, maintained detection accuracy, and improved the model's deployment efficiency on resource-constrained devices.

The rest of this paper is organized as follows. Section 2 introduces the construction of the dataset materials and the specific methods for the improvement of the visual network. Section 3 presents five comparative experiments that verify the improved network from different perspectives. Section 4 is the conclusion of this paper.

2. Materials and Methods

2.1. Building the Pineapple Dataset

In this research, we constructed a pineapple image dataset, to support and validate our object detection model. The image collection was carried out at a pineapple plantation in Xuwen County, Zhanjiang City, Guangdong Province. During the photography process, we were cognizant of the potential issues that class imbalance could pose for subsequent model training. To address this, we adopted various shooting strategies: selecting a range of shooting angles and capturing images at different times throughout the day, to ensure that the images comprehensively covered the various lighting conditions and occlusion scenarios that pineapples might encounter in their natural growth environment. This collection method enhanced the model's generalization capability in the face of different environmental conditions. Ultimately, we successfully collected approximately 1100 high-resolution RGB pineapple images. To further enhance the effectiveness of model training and the accuracy of validation, we utilized the labeling dataset annotation software to annotate the target areas. There was only one target category annotated, named "pineapple". Figure 1 shows the pineapple under different occlusion and lighting conditions. The collected images were then divided into training, validation, and test sets at a ratio of 70%, 20%, and 10%, respectively. This division ensured that the model could learn thoroughly during the training process and that its performance could be accurately evaluated during the validation and testing phases.

2.2. Improved YOLOv7-Tiny Network Framework

The network proposed in this paper, RGDP-YOLOv7-tiny, is an evolution of the traditional YOLO series, meticulously crafted to address the complexities of large-scale pineapple cultivation environments. It is composed of three integral sub-networks: a backbone network, a neck network, and a detection network. The backbone network, at the heart of the model, is a lightweight ReXNet designed to efficiently extract features from input data while reducing spatial dimensions and computational load. ReXNet incorporates depthwise separable convolutions and inverted residual structures, alongside a channel-wise progressive shrinking strategy, enhancing feature representation and minimizing computational overhead. Building upon the backbone's output, the neck network inte-

grates the innovative GSConv module. This module employs a unique channel-shuffling operation, to improve feature fusion across different channels, thereby augmenting the model's ability to capture nuanced pineapple features amidst varying lighting and weather conditions, as well as the occlusion factors present in the dataset. Transitioning to the detection network, we replaced the original YOLOv7-tiny detection head with a decoupled head structure. This design separates the classification and localization tasks, allowing for a focused enhancement of the model's convergence speed and detection accuracy. Each task now targets specific features, which is instrumental in improving the overall precision of the model.

Figure 1. (**a**) Sunny morning (unobstructed). (**b**) Sunny morning (foliage obstruction). (**c**) Sunny noon (uneven light). (**d**) Sunny noon (sunlit). (**e**) Sunny noon (backlit). (**f**) Evening.

Finally, to compress and optimize the model further, we employ sparse training, to guide the model in discerning dispensable parameters from crucial ones. Subsequently, a group-level pruning method, informed by a dependency graph analysis, is applied, to prune the less important parameters. This structured approach effectively reduces the model's complexity without compromising its performance, aligning with the objectives of lightweight improvement work that begins with refining these three sub-networks. The structure of the RGDP-YOLOv7-tiny network is shown in Figure 2.

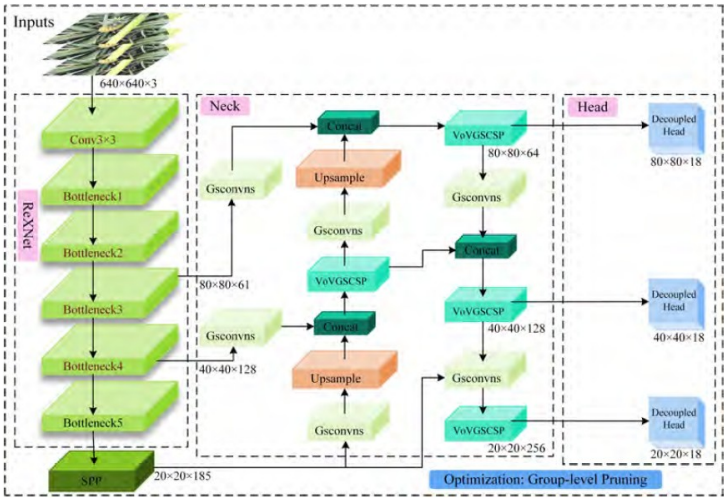

Figure 2. Total network architecture diagram.

2.2.1. YOLOv7-Tiny Network Framework

YOLOv7-tiny is a lightweight version of the YOLOv7 algorithm [22–24]. It aims to maintain high detection accuracy while reducing the complexity of the model and resource consumption during runtime, making it more suitable for deployment in environments with limited resources.

Compared to the overall network architecture of YOLOv7, YOLOv7-tiny has reduced the stacking of convolutional blocks in both the ELAN layer and the SPPCSP layer, which decreases the model's parameter count and computational complexity. In the neck network part, the multi-scale feature fusion method is retained. Through the feature pyramid fusion module and the feature pyramid alignment module, feature maps of different levels are interwoven, to better utilize the information from multi-level features. In the detection head part, standard convolution (SC) is used instead of RepConv, to further reduce the model's parameter count. In the activation function part, LeakyReLU is chosen, to minimize computational expenses [25].

Despite its advantages in lightness and detection speed, YOLOv7-tiny still has some shortcomings: the core of the ELAN layer is one or more aggregation modules that are responsible for effectively fusing the input feature maps, which typically include cross-layer and residual connections. While these connections effectively preserve the information of both low-level and high-level features, they also increase the complexity of the network and, to some extent, the computational load. This paper proposes the use of other lightweight modules for improvement and, on this basis, further compresses the model's computational load through model pruning.

2.2.2. Trunk Replacement

Researchers Dongyoon Han et al. from the NAVER AI Lab proposed Rank Expansion Networks (ReXNet) as an improvement and refinement of the lightweight network structure based on MobileNet [26]. The Google research team created MobileNet [27], a deep neural network architecture, with the express purpose of implementing effective neural network models on embedded systems and mobile devices. It reduces computational load and model size by adopting depthwise separable convolutions (DSC) and inverted residual structures [28].

However, many types of deep networks, including MobileNet, currently exhibit varying degrees of layer bottleneck issues: the low rank of network inputs does not adequately represent high-rank spaces. That is, if the resulting dimensions are relatively high when high-dimensional information is transformed into low-dimensional information then the loss of information is minimal. Conversely, if the resulting dimensions are relatively low, the loss of information is significant. After passing through the ReLU activation function, the loss of information is further exacerbated. The core concept of ReXNet is to incorporate the Swish activation function and to design additional expansion layers, to reduce the rank during each expansion, allowing the input dimensions to gradually approach the output dimensions. This unique channel dimension adjustment strategy not only maintains efficient computation but also significantly enhances the expressiveness of lightweight models in image-recognition tasks and classification tasks. It has not only advanced the design of lightweight models but has also paved new avenues and ideas for the optimization and exploration of network architectures.

With the specific structure described in Table 1, the ReXNet used in this paper is an improved version derived from the second-generation MobileNet architecture. The input image size has been changed from its original 214 × 214 dimensions to 640 × 640. The bottleneck structure, known as MB-bneck, is made up of 17 sequences in total. The squeeze-and-excitation attention mechanism module is integrated into the structures from sequences 5 through 17. Sequences 6, 12, and 17 function as the backbone's three feature output layers, each of which is connected to the neck network. For these three output feature layers, the corresponding output channel numbers are 61, 128, and 185.

Table 1. The network structure of ReXNet.

Sequential	Input	Operator	Output	Stride
1	$640^2 \times 3$	Conv 3 × 3	32	2
2	$320^2 \times 32$	MB-bneck1	16	1
3	$320^2 \times 16$	MB-bneck6	27	2
4	$160^2 \times 27$	MB-bneck6	38	1
5	$160^2 \times 38$	MB-bneck6	50	2
6	$80^2 \times 50$	MB-bneck6	61	1
7	$80^2 \times 61$	MB-bneck6	72	2
8	$40^2 \times 72$	MB-bneck6	84	1
9	$40^2 \times 84$	MB-bneck6	95	1
10	$40^2 \times 95$	MB-bneck6	106	1
11	$40^2 \times 106$	MB-bneck6	117	1
12	$40^2 \times 117$	MB-bneck6	128	1
13	$40^2 \times 128$	MB-bneck6	140	2
14	$20^2 \times 140$	MB-bneck6	151	1
15	$20^2 \times 151$	MB-bneck6	162	1
16	$20^2 \times 162$	MB-bneck6	174	1
17	$20^2 \times 174$	MB-bneck6	185	1
18	$20^2 \times 185$	Conv 1 × 1, pool 7 × 7	1280	1
19	$1^2 \times 1280$	Fc	1000	1

2.2.3. Neck Network Introduces the GSConv Lightweight Module

In convolutional neural networks, DSC refers to an operation where each input channel is convolved with a separate convolutional kernel. The structure of the DSC primarily consists of two parts: depthwise convolution and pointwise convolution. Compared to standard convolution, DSC avoids weight sharing, reducing the number of parameters and the computational cost, and it is often used in the design of lightweight neural networks. As shown in Figure 3, different convolutional structures are depicted.

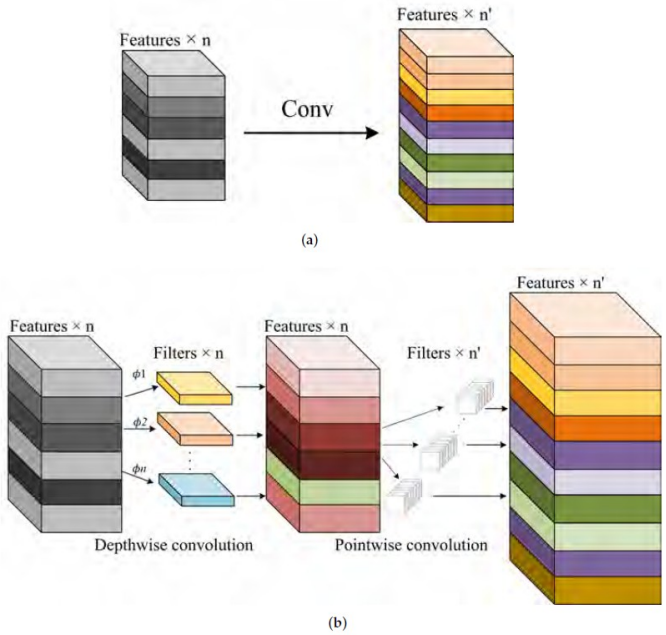

Figure 3. (**a**) Standard convolution. (**b**) Depthwise separable convolution.

The expressions of the parameter quantities P_{sc}, P_{dsc} and the calculation quantities S_{sc}, S_{dsc} of SC and DSC modules are as follows:

$$P_{sc} = C_i \cdot K_w \cdot K_h \cdot C_o \tag{1}$$

$$P_{dsc} = C_i \cdot K_w \cdot K_h + C_o \cdot C_i \tag{2}$$

$$S_{sc} = C_i \cdot K_w \cdot K_h \cdot C_o \cdot W \cdot H \tag{3}$$

$$S_{dsc} = C_i \cdot K_w \cdot K_h \cdot H \cdot W + C_o \cdot C_i \cdot W \cdot H \tag{4}$$

In the formulas, C_i represents the number of input channels, while C_o represents the number of output channels. K_w and K_h are the width and height of the convolutional kernel, respectively. W and H are the width and height of the feature map, respectively.

Since DSC lacks interaction between weights, the detection accuracy of networks built solely with DSC is typically lower. A balance between module weights and detection accuracy must be considered. Therefore, this paper replaces the SC and ELAN modules in YOLOv7-tiny with GSConvns and VoVGSCSP in the neck network [29], respectively. The specific structure is shown in Figure 4.

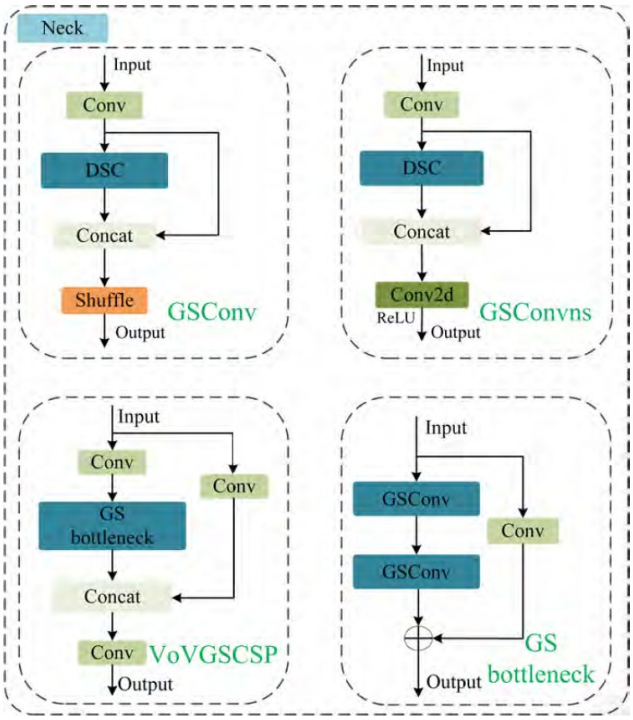

Figure 4. The module structures of GSConv, GSConvns, VOVGSCSP, and GS bottleneck.

The GSConv structure depicted in the diagram is bifurcated into two pathways: the primary path first undergoes SC and DSC operations, followed by a concatenation with a secondary path that has no convolutional operations. Subsequently, a channel shuffle (CS) operation is employed, to permeate the information generated by SC into every segment of the DSC information, altering the channels to a specified dimension. CS is a channel mixing strategy that, by swapping local feature information across various channels, can fully integrate the information from DSC into the input of SC, thereby compensating for the lower detection accuracy inherent in DSC. Gsconvns represents a variant structure of Gsconv, where the original channel shuffle operation is substituted with a two-dimensional convolution followed by an activation function ReLU. This structure also blends the feature information emanating from the DSC output through two-dimensional convolution. VoVGSCSP strongly resembles GSConv, with the distinction that the channel shuffle operation is replaced by a standard convolution, and the DSC are supplanted by a GS bottleneck structure. The bottleneck layer structure, GS bottleneck, is composed precisely of two GSConv units and an SC module. These four configurations are applied to different convolutional layers within the neck network, augmenting the diversity of the network's convolutional operations.

2.2.4. Detection Network Introduces Decouped Head

The detection head in a neural network is an essential component of object detection models, tasked with extracting and predicting the class and location of objects from feature maps. In the early versions of YOLO, the detection heads were typically coupled, mean-

ing that the classification and localization tasks were performed simultaneously within the same network layer. Starting from YOLOv2, the series introduced the anchor box mechanism, which uses a predefined set of bounding boxes to match objects of various sizes. Following YOLOv3, the concept of multi-scale detection was introduced [30], which involves making predictions on feature maps at different layers, to detect objects at various scales. This paper retains the anchor box mechanism and multi-scale detection from the YOLO series and replaces the original coupled head structure with a decoupled head structure [31]. The decoupled head is based on the core idea of separating the classification and localization tasks in object detection. This structural change allows each task to focus on its specific features, thereby improving the model's convergence rate and effectively reducing the number of parameters and computational complexity, thus providing enhanced performance in object-detection tasks. The structure of the decoupled head is illustrated in Figure 5. The numerical values of 256, 128, and 64 in the figure correspond to the number of output channels for the three stages of the neck network, respectively. Cls, Reg, and IoU represent the classification, location, and object score, respectively.

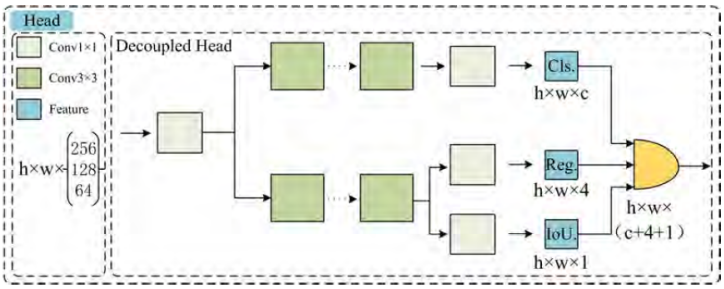

Figure 5. Structure of decoupled head.

2.3. Model Compression

2.3.1. Model Pruning

Model pruning is a deep learning model optimization technique, primarily aimed at reducing the complexity of models and enhancing efficiency. By analyzing the weights in a neural network, pruning technology identifies and removes weights that have a minimal impact on the model's output, thereby reducing the number of model parameters and computational requirements. This simplification can significantly decrease the model's inference time, reducing latency. Additionally, pruning can reduce the model's memory footprint, which helps to decrease the frequency of memory access and data exchange on devices, further lowering power consumption and extending the usage time and battery life of devices. At the same time, a smaller model size is also beneficial for deployment on mobile devices or embedded systems, reducing deployment costs and time.

The main pruning techniques nowadays are channel pruning, layer pruning, and unstructured pruning. Channel pruning reduces the width of the network by removing entire channels from convolutional layers, thereby reducing the model's parameter count and computational complexity. However, this may affect the expressiveness of the features. Layer pruning involves removing entire convolutional layers from the network, which can significantly reduce the model's depth, but may also lead to the loss of more feature information, affecting the model's learning ability. Unstructured pruning is carried out at the weight level, without following the inherent structure of the network. This flexibility allows it to achieve a higher compression ratio without sacrificing network performance, but it may require special optimization strategies to deal with sparsity issues.

This paper utilizes group-level pruning as the model pruning method [32]. This structured pruning technique is applicable to various network architectures. It constructs a

dependency graph to identify and model the structural interdependencies among layers within a neural network, and it groups the structured parameters within the network. Subsequently, parameters with low importance scores, as determined by subsequent sparse training, are pruned. This approach aims to reduce the model's size and expedite the inference process.

The dependency graph is the core of the group-level pruning algorithm. Here is an explanation of the dependency graph: Due to the structural coupling relationships between layers within the same and different layers of a neural network, when one layer is pruned, another layer will also undergo corresponding changes. To achieve structured pruning, we need to analyze the interdependencies of layers, to group parameters: for example, a parameter group $L = \{l_1^-, l_1^+, l_2^-, l_2^+, \ldots, l_n^-, l_n^+\}$, where each l refers to a parameterized layer, including convolutional (Conv2d) layers, batch normalization (BN) layers, and activation function layers, or a non-parameterized operation, such as residual addition. The positive and negative superscripts of l represent the outputs and inputs of the layers, respectively.

By focusing on the dependency relationships between layer inputs and outputs, a layer dependency model is constructed, as shown in Equation (5) for the dependency expression:

$$(l_1^-, l_1^+) \leftrightarrow (l_2^-, l_2^+) \leftrightarrow \cdots \leftrightarrow (l_n^-, l_n^+) \tag{5}$$

The equation includes two types of layer dependencies: inter-layer dependency l_i^+, l_j^- and intra-layer dependency l_i^-, l_i^+. Inter-layer dependency refers to the direct association between adjacent layers in the network, where the output features of one layer serve directly as the input to the next layer, creating an end-to-end connection. Intra-layer dependency refers to the association between the inputs and outputs within a single layer. As shown in Figure 6, the parameter dependency analysis of two standard convolution modules with residual links is performed. The batch normalization layer is l_2 or l_5, and their respective input and output are a pair of intra-layer dependencies and are coupled. However, the inputs and outputs of layer l_4 are not dependent on each other and are independent, yet we can still group them into the same parameter group and prune them with different pruning layouts, to achieve consistent cross-layer pruning. This enhances the efficiency of pruning and the accuracy of model compression.

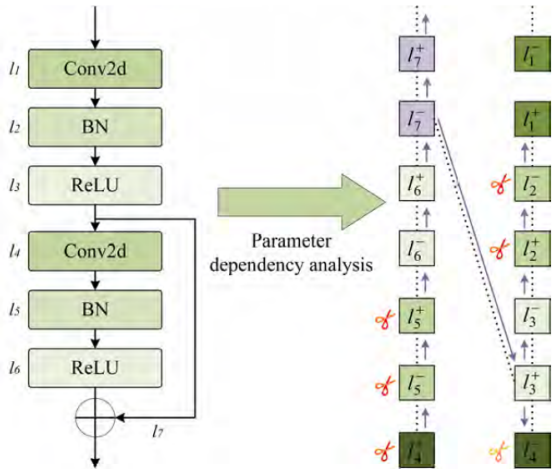

Figure 6. Dependency graph analysis.

2.3.2. Sparse Training

During the process of group-level pruning, batches of parameters are deleted simultaneously. To ensure the effectiveness of pruning, it is necessary to confirm that the deleted parameters are collectively unimportant, meaning their contribution to the network's performance can be disregarded. If the group of parameters includes those that are crucial for the network's predictive ability, removing them may lead to a significant degradation in network performance. In such cases, a strategy of sparse training is required to identify these parameters, allowing them to be safely removed during the pruning process.

This paper introduces a regularization term $H_{g,k}$ for the weight parameter group $g = \{w_1, w_2, \ldots, w_g\}$ with K dimensions that can be pruned. The purpose is to motivate the model to learn which parameters in the group g are expendable for pruning. The specific formulation is as follows:

$$H_{g,k} = \sum_{k=1}^{K} \gamma_k \cdot Q_{g,k} \tag{6}$$

$$Q_{g,k} = \sum_{w \in g} \|w[k]\|_2^2 \tag{7}$$

$$\gamma_k = 2^{\alpha\left(Q_g^{\max} - Q_{g,k}\right)/\left(Q_g^{\max} - Q_g^{\min}\right)} \tag{8}$$

In Equation (6), y is a scaling factor that controls the sparsity strength of the k-th prunable dimension, while $Q_{g,k}$ denotes the importance score of the parameter w in the k-th prunable dimension within the parameter group g.

In Equation (7), $w[k]$ represents the k-th parameter submatrix within the parameter group g, where w refers to the weight parameters of the neural network and k refers to a specific slice of the parameter matrix—that is, a subset selected from the entire parameter matrix. During group-level pruning, this slicing operation allows the algorithm to focus on the submatrix within the current parameters, thereby enabling independent analysis of each parameter group.

In Equation (8), α is a hyperparameter that controls the range of sparsity intensity, while $Q_{\max}$ and $Q_{\min}$ denote the maximum and minimum importance scores, respectively, within the parameter group g, which are used to determine the strength of sparsity.

Utilizing the sparse training algorithm described, we can identify k sets of parameters with varying levels of sparsity. We then select the set with the minimal L2 norm, which has the least detrimental effect on model performance, for group-level pruning of the network structure.

2.4. Model Evaluation Metrics

To evaluate the performance and complexity of the model, this study chose several metrics commonly used in object detection. These include precision, recall, the comprehensive evaluation metric $F1$, average precision (AP), mean average precision (mAP), the count of parameters (Params), the computational load, in terms of floating point operations (FLOPs), and the size of the model. The expressions for calculating the first five metrics are as follows:

$$P = \frac{TP}{TP + FP} \tag{9}$$

$$R = \frac{TP}{TP + FN} \tag{10}$$

$$F1 = \frac{2PR}{P + R} \tag{11}$$

$$AP = \int_0^1 PRdR \tag{12}$$

$$mAP = \frac{1}{C} \sum_{i=0}^{c} AP_i \tag{13}$$

Equation (9) and Equation (10) represent precision and recall, respectively. In these equations, TP indicates true positives, where the actual class of the sample is positive and the prediction is also positive; TN indicates true negatives, where the actual class is negative and the prediction is negative; FP indicates false positives, where the actual class is negative but the prediction is positive; FN indicates false negatives, where the actual class is positive but the prediction is negative. Precision describes the proportion of true positives among the positives predicted by a binary classifier, while recall describes the proportion of actual positives that have been identified.

Equation (11) is the harmonic mean of precision and recall, known as the F1 score. Its value ranges from 0 to 1, with a value closer to 1 indicating better model performance. In practical applications, depending on the specific needs of the problem, we may focus more on either precision or recall, but the F1 score provides a measurement that takes both into account.

Equation (12) measures the performance of detection for a particular class, which can be understood as having recall on the horizontal axis and precision on the vertical axis of a coordinate system; the area where the curve intersects with both axes represents the average precision. The larger the intersecting area, the higher the AP value. Equation (13) calculates mean average precision, which assesses the overall effectiveness of detection across all classes.

The latter three metrics assess the complexity of the model. FLOPs refers to the number of floating-point operations per second, reflecting the amount of computational resources required to execute a neural network model. The number of parameters refers to the total count of learnable parameters within the neural network model, typically including weights and biases. Model size refers to the file size of the model, which affects the deployment efficiency of the model. Smaller models are easier to deploy on devices with limited resources, while larger models require longer transmission times and more bandwidth.

3. Experiments and Analysis

For this paper, we conducted the following four types of experiments: comparative experiments between YOLOv7-tiny and different lightweight backbones; comparative experiments with different pruning methods; comparative experiments under a wide range of pruning ratios; and comparative experiments with different target-detection algorithms and their corresponding pineapple detection visualization. The comparative experiment of pruning methods in Section 3.2 of this article compared the impact of different pruning techniques on the performance of the YOLOv7-tiny model. The experimental results provided a basis for selecting the most effective pruning method. The comparative experiment of pruning multiples in Section 3.3 of this article was an exploration of the depth of the selected pruning technology, with the aim of finding the optimal pruning ratio and achieving the best balance between model complexity and performance. The experiments on different target-detection algorithms in Sections 3.4 and 3.5 of this article expanded the research horizon. The purpose of this section is to show the competitiveness and practicality of RGDP-YOLOv7-tiny in target-detection tasks, especially in resource-constrained environments. Each experiment in this section was based on the results of the previous step, gradually deepened, and, finally, formed a complete research process. The environment configuration of this experiment is shown in Table 2. The batch size of the experiment was set to 16, the training epoch was set to 300, and the image resolution was selected as 640 × 640.

Table 2. Experimental configuration.

Configuration	Parameters
CPU	I5-12600KF
GPU	NVIDIA GeForce RTX 4060 Ti
Operating system	Windows 10
Accelerated environment	CUDA 12.1.0; CUDNN 8.9.4.25
Library	Pytorch 2.1.1; Torch-Pruning 1.3.6

3.1. Lightweight Backbone Comparative Experiment

To explore the performance of different lightweight backbones on YOLOv7-tiny, for this section we conducted a comparative analysis of models optimized at various pruning ratios for each lightweight backbone. YOLOv7-tiny was selected as the base network, and its backbone network was replaced with GhostNet [33], GhostNetv2 [34], FasterNet [35], ReXNet, and MobileNetv3 [36], respectively. Each network was pruned at pruning ratios of 1.0, 2.0, and 2.5. Subsequently, the models were fine-tuned and their performance was compared. The experimental results are presented in Table 3.

Table 3. Comparison of pruning results of YOLOv7-tiny under different backbone networks.

Model	Pruning Ratio	mAP@0.5 (%)	Precision (%)	Recall (%)	F1 Score (%)	Params (M)	FLOPs (10^9)	Model Size (MB)
YOLOv7-tiny	1.0	87.1	92.9	80.2	86.1	6.01	13.2	12.3
	2.0	88.0	93.3	81.7	87.1	3.0	6.5	6.3
	2.5	86.8	89.7	81.7	85.5	2.37	5.2	5.0
GhostNet-YOLOv7-tiny	1.0	88.4	93.1	81.9	87.1	4.29	7.5	9.0
	2.0	80.0	90.3	71.8	80.0	1.76	3.7	3.9
	2.5	79.0	89.0	71.6	79.4	1.4	3.0	3.2
GhostNetv2-YOLOv7-tiny	1.0	89.7	95.2	82.3	88.3	4.59	7.9	9.6
	2.0	80.4	89.0	73.2	80.3	1.9	3.8	4.2
	2.5	80.2	88.8	74.3	80.9	1.5	3.1	3.4
FasterNet-YOLOv7-tiny	1.0	85.5	89.7	79.1	84.1	5.65	11.4	11.6
	2.0	86.0	92.5	79.3	85.4	3.09	5.6	6.5
	2.5	85.4	91.7	78.8	84.8	2.43	4.5	5.1
ReXNet-YOLOv7-tiny	1.0	88.6	93.4	81.7	87.2	6.64	12.0	13.7
	2.0	89.5	94.8	81.7	87.8	3.09	6.0	6.6
	2.5	86.5	92.8	80.7	86.3	2.57	4.7	5.5
MobileNetv3-YOLOv7-tiny	1.0	85.9	93.5	77.6	84.8	4.48	6.7	9.3
	2.0	82.5	89.0	76.2	82.1	1.86	3.3	4.0
	2.5	83.3	94.7	73.9	83.0	1.72	2.6	3.8

The data from Table 3 indicates that at a pruning ratio of 1.0, which means no pruning was applied, the YOLOv7-tiny network with the FasterNet and MobileNetv3 backbones had lower mAP@0.5 and F1 scores compared to the original YOLOv7-tiny. However, when using GhostNet, GhostNetv2, and ReXNet as the backbones, these metrics were

approximately 1.5% higher than the original YOLOv7-tiny. It should be noted that the GhostNet series reduced the parameter count, computational load, and model size, whereas ReXNet saw a slight increase; when the pruning ratio was 2.0, the mAP@0.5, precision, recall, and F1 scores of the GhostNet series experienced a significant decrease, which may be attributed to excessive pruning, causing the model to lose information that was critical for classification and localization tasks. In contrast, ReXNet showed better anti-pruning performance, with its mAP@0.5 and F1 scores increased by 0.9% and 0.6%, respectively, compared to the unpruned state. Compared to the original YOLOv7-tiny at a pruning ratio of 2.0, these improvements were 1.5% and 0.7% higher, respectively; when the pruning ratio reached 2.5, ReXNet's F1 score rose by 0.8% compared to the original YOLOv7-tiny, and although the mAP@0.5 dropped by 0.3%, ReXNet still demonstrated its advantages at this pruning level. Compared to its unpruned state, its parameter count, computational load, and model size were reduced by 39.4%, 39.2%, and 40.1%, respectively. This shows that ReXNet is more robust in structure and can better maintain its performance after pruning.

3.2. The Impact of Different Pruning Methods on Model Performance

To verify the advantages of the pruning methods adopted in this paper, various pruning techniques were applied to the network structure model depicted in Figure 2, followed by subsequent fine-tuning, to further optimize model performance. The specific pruning methods used included a filter pruning method based on the L1 norm (P1), a pruning method that evaluates the importance of neurons through the Taylor expansion of the loss function [37] (P2), a pruning method that assesses network weights based on the second-order derivatives of the objective function [38] (P3), and the group-level pruning method proposed in this paper (P4). The experimental results are shown in Table 4.

Table 4. Comparison results of different pruning methods.

Pruning Methods	Pruning Ratio	mAP@0.5 (%)	Precision (%)	Recall (%)	F1 Score (%)	Params (M)	FLOPs (10^9)	Model Size (MB)
P1	2.0	74.2	87.5	64.5	74.3	4.11	5.7	8.7
P2		83.9	92.1	75.1	82.7	3.64	5.6	7.8
P3		76.9	88.2	67.8	76.7	3.43	5.6	7.4
P4		87.9	92.5	81.7	86.8	2.77	5.7	6.0

According to the comparative experimental results in Table 4, it can be observed that the group-level pruning method achieved the highest levels in key performance indicators, such as mAP@0.5, F1 score, precision, and recall. This indicates that during the pruning process, the group-level pruning method effectively preserved parameters that were crucial for the network's predictive performance, avoiding performance loss due to excessive pruning. Furthermore, from the perspective of model complexity, the group-level pruning method also showed a significant advantage in reducing the number of parameters, the computational load, and the model size. Compared to other pruning methods, it achieved the lowest model complexity, demonstrating greater efficiency in identifying and removing parameters that contribute less to model performance.

In summary, the group-level pruning method not only showed outstanding performance in improving model capabilities but also had a significant advantage in reducing model complexity. To delve deeper into the performance of the group-level pruning method, we analyzed the decline in mAP@0.5 and parameter count as the pruning ratio increased during the pruning process, as illustrated in Figure 7, as well as the channel comparison chart for different pruning methods at a pruning ratio of 2.0, as shown in Figure 8. Through this visualization, we could more directly perceive the group-level pruning method's capacity to balance model efficiency with the maintenance of predictive accuracy.

Figure 7a represents the curve of mAP@0.5 as the pruning ratio increased. It can be observed that for pruning methods P1, P2, and P3, the mAP@0.5 dropped to 0 when the

pruning ratio reached 1.5. In contrast, method P4 maintained the mAP@0.5 of around 80.0%. As the pruning ratio further increased to 2.0, the mAP@0.5 of P4 could still be sustained at approximately 65.0%. This indicates that under the same pruning ratio, the model pruned by P4 had more potential to recover to the initial model's accuracy after fine-tuning compared to the other pruning methods. At different pruning ratios, the impact of P4 pruning on model accuracy was relatively smaller, implying that more significant compression effects can be achieved at a higher pruning ratio. Figure 7b reveals how the model's parameter count changed with the increase in pruning ratio, showing that compared to the other pruning methods, P4 pruning achieved the greatest degree of parameter reduction at any pruning ratio. Integrating these observations, we can conclude that the group-level pruning method used in this paper can maximize model compression at a higher pruning ratio while maintaining model performance.

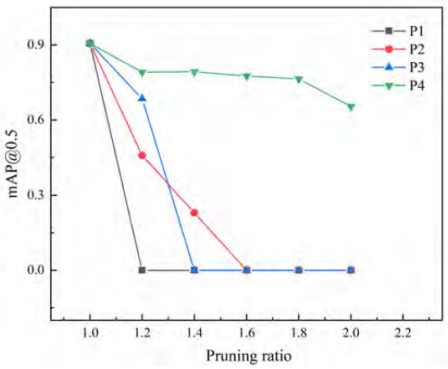

(a)

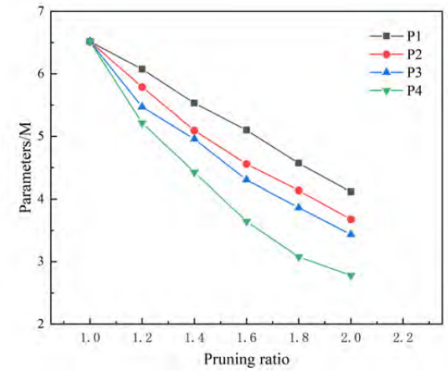

(b)

Figure 7. (**a**) The curve of mAP@0.5 with the incremental increase of pruning ratio. (**b**) The curve of the number of parameters with the incremental increase of pruning ratio.

As illustrated in Figure 8, the vertical axis represents the number of channels and the horizontal axis refers to the detailed convolutional operations within the three main network layers. The term "Base" denotes the model before pruning, while "Prune" indicates the model at a pruning ratio of 2.0. Among the four pruning methods, there was no significant

difference in the channel compression effect in the neck and detection networks. However, in the ReXNet backbone network section, regardless of the pruning method applied, the number of channels could be significantly reduced. Under the P1, P2, and P3 pruning methods, the maximum number of channels in the backbone could be compressed to below 600, 500, and 800, respectively. In contrast, under the P4 pruning method, the maximum number of channels in the backbone could be compressed to below 200, achieving a channel compression ratio of approximately 80%, which was more than 1.6 times higher than that of the other pruning methods. This further confirms the superior model compression efficiency of the group pruning approach.

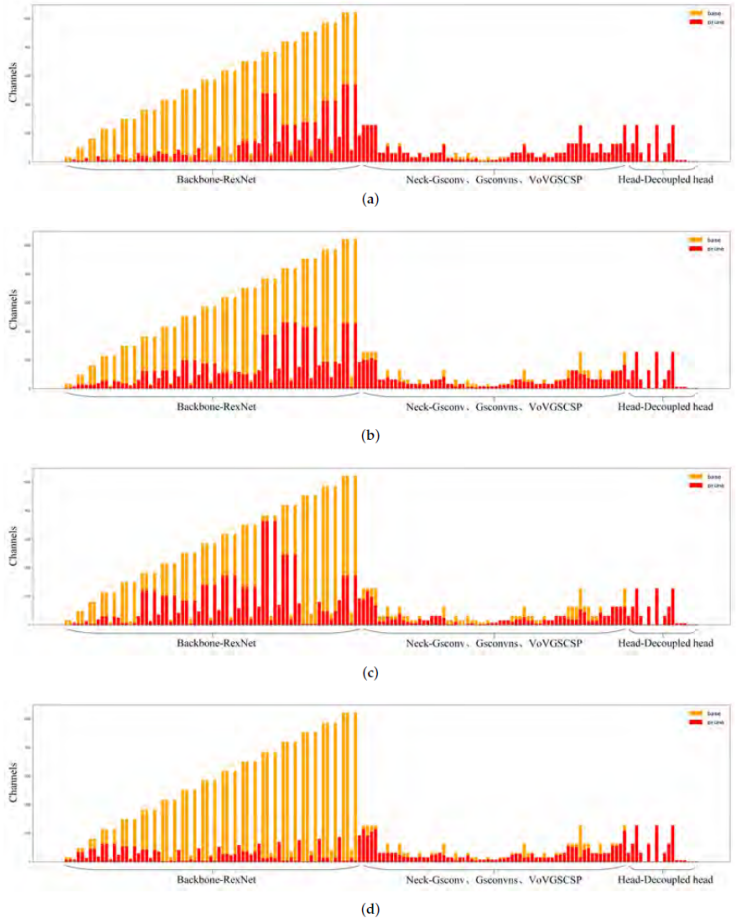

Figure 8. (**a**) P1 pruning. (**b**) P2 pruning. (**c**) P3 pruning. (**d**) P4 pruning.

3.3. The Impact of Different Pruning Ratios on Model Performance

From Figure 7a, it can be observed that the mAP@0.5 for the P4 pruning method did not drop to zero as the pruning ratio increased, unlike the other pruning methods. For

models that mAP@0.5 reduced to zero, their performance could still be improved, to some extent, after subsequent fine-tuning. Therefore, we had reason to further explore the impact on model performance across a broader range of pruning multiples.

In the following experiment, group-level pruning was applied to the network structure model shown in Figure 2, and the pruning ratio was gradually increased in a stepwise manner. The initial pruning ratio was set at 2.0, and it was increased by 0.1 with each step, up to a maximum of 3.0. The final model was obtained through fine-tuning. Detailed experimental data can be found in Table 5.

Table 5. Comparison results at different pruning ratios.

Pruning Ratio	mAP@0.5 (%)	Precision (%)	Recall (%)	F1 Score (%)	Params (M)	FLOPs (10^9)	Model Size (MB)
1.0	90.1	91.6	85.3	88.3	6.52	11.4	13.6
2.0	87.9	92.5	81.7	86.8	2.77	5.7	6.0
2.1	87.4	91.4	81.0	85.9	2.60	5.3	5.7
2.2	87.8	93.1	80.3	86.2	2.49	5.1	5.5
2.3	87.0	92.6	80.2	86.0	2.39	4.9	5.3
2.4	87.7	91.3	82.3	86.6	2.33	4.7	5.1
2.5	87.9	94.9	81.0	87.4	2.27	4.5	5.0
2.6	85.2	89.3	79.7	84.2	2.21	4.3	4.9
2.7	74.4	84.3	68.5	75.6	2.16	4.2	4.8
2.8	74.5	89.6	66.3	76.2	2.09	4.0	4.7
2.9	74.1	88.6	65.2	75.1	2.04	3.9	4.6
3.0	74.3	85.7	65.9	74.5	1.95	3.8	4.4

Based on the data from Table 5, it is evident that before pruning, the completely replaced network model saw an increase of 1.5% in mAP@0.5 and 1.1% in the F1 score over the ReXNet-YOLOv7-tiny model. The parameter count, computational load, and model size were reduced by 0.12×10^6, 0.6×10^9, and 0.01 MB, respectively. Within the pruning ratio range of 2.0 to 2.5, the model's performance remained relatively stable after fine-tuning, with no significant fluctuations. Meanwhile, the complexity metrics of the model, including parameter count, computational load, and model size, continued to decline. However, when the pruning ratio increased beyond 2.6, the model's performance metrics began to decline noticeably and the rate of decrease in the complexity metrics also slowed. This indicated that within the pruning ratio range of 2.0 to 2.5 an equilibrium had been achieved between model performance and complexity. Beyond this range, further pruning began to negatively affect model performance, and the effect of reducing model complexity also gradually diminished. Consequently, the network structure in Figure 2, after a 2.5-times pruning, represents the final improved pruned lightweight pineapple detection network model RGDP-YOLOv7-tiny obtained in this paper. When comparing this model with the YOLOv7-tiny after a 2.5-times pruning, as listed in Table 3, RGDP-YOLOv7-tiny achieved higher compression ratios of 4.6% in parameter count and 3.9% in model size, with a 0.1% reduction in computational load. In short, the improved model's compression effect is more pronounced than the original YOLOv7-tiny.

3.4. Performance Comparison of Different Object-Detection Algorithms

To objectively validate the proposed pruned lightweight pineapple-detection algorithm, this experiment compared six object-detection algorithms: YOLOv5s, YOLOv7, YOLOv7-tiny, YOLOv8s, YOLOv8n, and RGDP-YOLOv7-tiny. The results are shown in Table 6. It can be observed that the RGDP-YOLOv7-tiny network had a parameter count of 2.27 M, a computational load of 4.5×10^9, and a model size of 5.0 MB. These complexity metrics are lower than those of other networks in the YOLO series. At the same time, the YOLOv7 network, with its higher model complexity, achieved mAP@0.5 and F1 scores of 90.0% and 88.0%, respectively, ranking first among all the compared networks. However, the RGDP-YOLOv7-tiny also performed well, reaching 87.9% and 87.4%. These results high-

light that RGDP-YOLOv7-tiny can maintain a high level of pineapple detection accuracy even with relatively lower resource consumption. Specifically, RGDP-YOLOv7-tiny outperformed other YOLO series networks in terms of parameter count, computational load, and model size, which implies not only computational efficiency but also more convenient application in agricultural robots.

Table 6. Comparison of different object-detection algorithms.

Pruning Ratio	mAP@0.5 (%)	Precision (%)	Recall (%)	F1 Score (%)	Params (M)	FLOPs (10^9)	Model Size (MB)
YOLOv5s	85.8	91.5	77.0	83.6	7.02	15.9	14.4
YOLOv7	90.0	93.2	83.3	88.0	37.20	105.1	74.8
YOLOv7-tiny	87.1	92.9	80.2	86.1	6.01	13.2	12.3
YOLOv8n	87.6	92.9	80.2	86.1	3.01	8.2	6.3
YOLOv8s	87.2	90.4	81.1	85.5	11.14	28.6	22.5
RGDP-YOLOv7-tiny	87.9	94.9	81.0	87.4	2.27	4.5	5.0

3.5. Pineapple Detection Visualization

This section employs the Grad-CAM heatmap visualization technique to illustrate the output of deep learning models [39]. The essence of this technology lies in leveraging the gradient information of the model's predictions concerning the input image. The gradients indicate the degree to which each pixel in the input image contributes to the model's output class score. By calculating these gradients and combining them with the model's intermediate feature maps, Grad-CAM can generate a heatmap. The intensity of colors on this heatmap represents the significance of each area to the model's predictive outcome, with highlighted areas indicating areas of greater focus. Specifically, the six object-detection algorithms listed in Table 6 were used to create heatmaps, as shown in Figure 9.

To evaluate the performance and generalization capability of the RGDP-YOLOv7-tiny network in detecting pineapples under various environmental conditions, for this section we tested multiple typical scenarios, including unobstructed, foliage-obstructed, uneven lighting, dim environments, and situations with front and backlighting. The collected field-planted pineapple images were used to generate heatmaps with the Grad-CAM technique, to visualize the model's predicted focus areas. Observing Figure 9, under the soft morning light and unobstructed conditions, the highlighted areas of the YOLOv7 and RGDP-YOLOv7-tiny networks were more concentrated, while the other networks were more dispersed. Under the four different lighting conditions at noon, the highlighted areas of the YOLOv5s, YOLOv7, and RGDP-YOLOv7-tiny networks were larger, showing impressive adaptability to lighting conditions, among which, the highlighted areas of the RGDP-YOLOv7-tiny were more concentrated, indicating that the network maintained high recognition accuracy under complex lighting conditions. Under the foliage obstruction, the level of highlighted areas drawn by the six networks was relatively average and the recognition performance of each network did not differ much. Overall, the heatmaps drawn by the YOLOv7 network had the widest and most concentrated highlighted areas, while the RGDP-YOLOv7-tiny network also demonstrated detection accuracy and generalization capability comparable to YOLOv7 while maintaining a lower parameter volume. This indicates that the RGDP-YOLOv7-tiny network not only maintains high precision in detecting pineapples but also has excellent generalization ability, capable of adapting to a variable field environment.

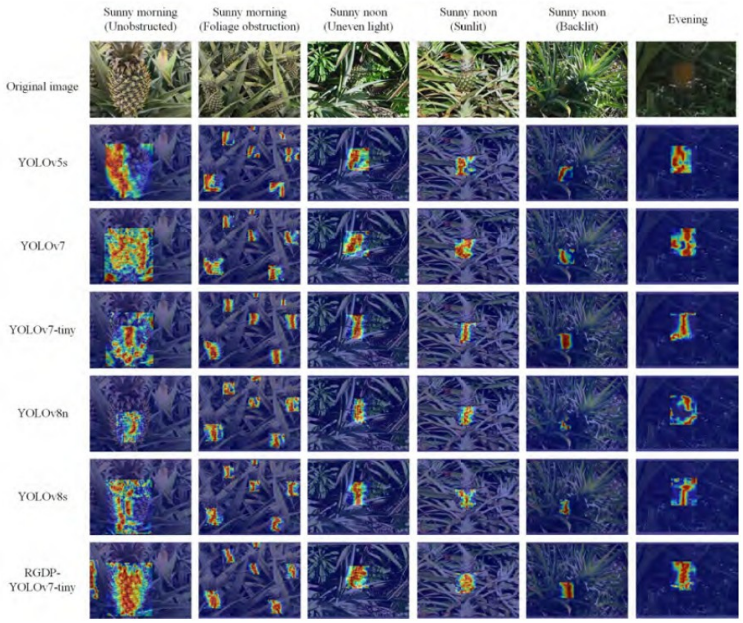

Figure 9. Heatmap visualization.

3.6. Performance of RGDP-YOLOv7-Tiny in Complex Scenarios

For this section, we explored the performance of the RGDP-YOLOv7-tiny model under diverse environmental conditions, through experiments, with a particular focus on its ability to handle false positives and false negatives when identifying targets in complex scenes. Figure 10 shows the results of 10 test images predicted by the RGDP-YOLOv7-tiny model, where green boxes represent true positives, blue boxes indicate false negatives, and red boxes signify false positives. The network detected a total of 132 target boxes, including 107 true positives, 10 false negatives, and 15 false positives. The green boxes predominantly appear in areas with abundant target features, while the blue and red boxes are mainly found in areas with fewer target features—that is, when the distance between the shooter and the target was farther then the resolution of the target object was reduced, leading to increased difficulty in feature extraction, which may be the main reason for missed and false detection. Considering that pineapple-harvesting robots mainly target objects at closer ranges, this network can meet the work requirements of pineapple-harvesting robots in practical applications. However, there is still room for improvement in the performance of long-distance targets. We will continue to explore model optimization strategies to enhance its robustness in different distances and complex environments, ensuring its efficiency and accuracy in actual harvesting operations.

Figure 10. Detection results of the RGDP-YOLOv7-tiny network.

4. Conclusions and Future Works

This paper addressed the application requirements of agricultural robots in large-scale planting environments by proposing an improved object detection model, RGDP-YOLOv7-tiny, designed to accommodate robotic platforms with limited computational resources. The model employs ReXNet as the backbone network, integrates GSConv into the neck network, and introduces a decoupled head in the detection network, ultimately achieving model compression through sparse training and group-level pruning optimization. Our experimental results demonstrated that, although the model's complexity slightly increased before pruning and optimization, there was a 3.0% improvement in mAP@0.5 and a 2.2% improvement in the F1 score, indicating that the model had greater potential for further compression in subsequent pruning processes. After pruning, the RGDP-YOLOv7-tiny model outperformed the original YOLOv7-tiny, with Params, FLOPs, and model size reduced from 6.01, 13.2 × 10^9, and 12.3 MB to 2.27, 4.5 × 10^9, and 5.0 MB, respectively, representing decreases of 37.8%, 34.1%, and 40.7%. Additionally, the mAP@0.5 and F1 scores of RGDP-YOLOv7-tiny also improved by 0.8% and 1.3%, reaching 87.9% and 87.4%, respectively. Despite the significant reduction in size, the mAP@0.5 and F1 scores of RGDP-YOLOv7-tiny remained higher than most of the YOLO series object-detection algorithms. The final heatmap visualization comparison also proved that the model maintains decent generalization performance across different pineapple cultivation environments, providing effective visual detection technology for pineapple agriculture robots. However, different pruning methods and lightweight modules exhibited varying adaptability to convolutional neural networks. In our future research, we plan to explore the adaptability between the various pruning methods and lightweight modules, aiming to further enhance the model's performance under resource-constrained conditions. Additionally, we recognize that the model may have limitations when generalized to a variety of agricultural scenarios, while target-detection tasks are ubiquitous in the agricultural field. Therefore, we can leverage transfer learning technology and make appropriate adjustments and optimizations to extend the framework to broader applications, including the detection of other crop targets, crop disease detection, and weed identification. We believe that, through further research and development, exploring these possibilities in our future work will promote the development of smart agriculture and contribute to the advancement of agricultural robot vision technology.

Author Contributions: Conceptualization, J.L. (Jiehao Li); formal analysis, C.L. and Q.L.; funding acquisition, J.L. (Jiehao Li); investigation, Y.L., C.L. and J.L. (Jiahuan Lu); methodology, J.L. (Jiehao Li), Y.L. and C.L.; project administration, J.L. (Jiehao Li); resources, J.L. (Jiahuan Lu); software, Q.L.; supervision, J.L. (Jiahuan Lu); validation, Q.L.; visualization, Y.L. and C.L.; writing—original draft, J.L. (Jiehao Li) and Y.L.; writing—review and editing, J.L. (Jiehao Li). All authors have read and agreed to the published version of the manuscript.

Funding: This research was funded by 2024 Basic and Applied Research Project of Guangzhou Science and Technology Plan, grant number: 2024A04J4140 and State Key Laboratory of Robotics and Systems (HIT), grant number: SKLRS-2024-KF-08 and The APC was funded by Jiehao Li.

Data Availability Statement: The original contributions presented in the study are included in the article, further inquiries can be directed to the corresponding author.

Acknowledgments: This work was supported by the 2024 Basic and Applied Research Project of Guangzhou Science and Technology Plan under Grant 2024A04J4140, the State Key Laboratory of Robotics and Systems (HIT) under Grant SKLRS-2024-KF-08, and the Young Talent Support Project of Guangzhou Association for Science and Technology under Grant QT2024-006.

Conflicts of Interest: The authors declare no conflicts of interest. The funders had no role in the design of the study; in the collection, analyses, or interpretation of data; in the writing of the manuscript, or in the decision to publish the results.

References

1. Liu, C.; Liu, Y. Current status of pineapple production and research in China. *Guangdong Agric. Sci.* **2010**, *10*, 65–68.
2. Li, D.; Jing, M.; Dai, X.; Chen, Z.; Ma, C.; Chen, J. Current status of pineapple breeding, industrial development, and genetics in China. *Euphytica* **2022**, *218*, 85. [CrossRef]
3. He, F.; Zhang, Q.; Deng, G.; Li, G.; Yan, B.; Pan, D.; Luo, X.; Li, J. Research Status and Development Trend of Key Technologies for Pineapple Harvesting Equipment: A Review. *Agriculture* **2024**, *14*, 975. [CrossRef]
4. Shu, H.; Sun, W.; Xu, G.; Zhan, R.; Chang, S. The Situation and Challenges of Pineapple Industry in China. *Agric. Sci.* **2019**, *10*, 683. [CrossRef]
5. Jiang, T.; Guo, A.; Cheng, X.; Zhang, D.; Jin, L. Structural design and analysis of pineapple automatic picking-collecting machine. *Chin. J. Eng. Des.* **2019**, *26*, 577–586.
6. Li, J.; Dai, Y.; Su, X.; Wu, W. Efficient Dual-Branch Bottleneck Networks of Semantic Segmentation Based on CCD Camera. *Remote Sens.* **2022**, *14*, 3925. [CrossRef]
7. Zhao, D.H.; Zhang, H.; Hou, J.X. Design of Fruit Picking Device Based on the Automatic Control Technology. *Key Eng. Mater.* **2014**, *620*, 471–477. [CrossRef]
8. Pengcheng, B.; Jianxin, L.; Weiwei, C. Research on lightweight convolutional neural network technology. *Comput. Eng. Appl.* **2019**, *16*, 25–35.
9. Li, J.; Li, J.; Zhao, X.; Su, X.; Wu, W. Lightweight detection networks for tea bud on complex agricultural environment via improved YOLO v4. *Comput. Electron. Agric.* **2023**, *211*, 107955. [CrossRef]
10. Liu, X.; Wang, J.; Li, J. URTSegNet: A real-time segmentation network of unstructured road at night based on thermal infrared images for autonomous robot system. *Control Eng. Pract.* **2023**, *137*, 105560. [CrossRef]
11. Li, B.; Ning, W.; Wang, M.; Li, L. In-field pineapple recognition based on monocular vision. *Trans. Chin. Soc. Agric. Eng.* **2010**, *26*, 345–349.
12. Li, X. Design of automatic pineapple harvesting machine based on binocular machine vision. *J. Anhui Agric. Sci.* **2019**, *47*, 207–210.
13. Yang, W.; Rui, Z.; ChenMing, W.; Meng, W.; XiuJie, W.; YongJin, L. A survey on deep-learning-based plant phenotype research in agriculture. *Sci. Sin. Vitae* **2019**, *49*, 698–716.
14. Zheng, Y.; Li, G.; Li, Y. Survey of application of deep learning in image recognition. *Comput. Eng. Appl.* **2019**, *55*, 20–36.
15. Sun, D.; Zhang, K.; Zhong, H.; Xie, J.; Xue, X.; Yan, M.; Wu, W.; Li, J. Efficient Tobacco Pest Detection in Complex Environments Using an Enhanced YOLOv8 Model. *Agriculture* **2024**, *14*, 353. [CrossRef]
16. Chunman, Y.; Cheng, W. Development and application of convolutional neural network model. *J. Front. Comput. Sci. Technol.* **2021**, *15*, 27.
17. Xu, L.; Huang, H.; Ding, W.; Fan, Y. Detection of small fruit target based on improved DenseNet. *J. Zhejiang Univ. (Eng. Sci.)* **2021**, *55*, 377–385.
18. Pengfei, Z.; Mengbo, Q.; Kaiqi, Z.; Yijie, S.; Haoyu, W. Improvement of Sweet Pepper Fruit Detection in YOLOv7-Tiny Farming Environment. *Comput. Eng. Appl.* **2023**, *59*, 329–340.
19. Liang, X.; Pang, Q.; Yang, Y.; Wen, C.; Li, Y.; Huang, W.; Zhang, C.; Zhao, C. Online detection of tomato defects based on YOLOv4 model pruning. *Trans. Chin. Soc. Agric. Eng* **2022**, *6*, 283–292.
20. Yinghui, K.; Chengcheng, Z.; LinLin, C. Flower recognition in complex background and model pruning based on MobileNets. *Sci. Technol. Eng.* **2018**, *18*, 84–88.
21. Li, J.Y.; Zhao, Y.K.; Xue, Z.E.; Cai, Z.; Li, Q. A survey of model compression for deep neural networks. *Chin. J. Eng.* **2019**, *41*, 1229–1239. [CrossRef]
22. Wang, C.Y.; Bochkovskiy, A.; Liao, H.Y.M. YOLOv7: Trainable bag-of-freebies sets new state-of-the-art for real-time object detectors. In Proceedings of the IEEE/CVF Conference on Computer Vision and Pattern Recognition, Vancouver, BC, Canada, 18–22 June 2023; pp. 7464–7475.

23. Zhou, J.; Zhang, Y.; Wang, J. RDE-YOLOv7: An improved model based on YOLOv7 for better performance in detecting dragon fruits. *Agronomy* **2023**, *13*, 1042. [CrossRef]
24. Yang, H.; Liu, Y.; Wang, S.; Qu, H.; Li, N.; Wu, J.; Yan, Y.; Zhang, H.; Wang, J.; Qiu, J. Improved apple fruit target recognition method based on YOLOv7 model. *Agriculture* **2023**, *13*, 1278. [CrossRef]
25. Xu, J.; Li, Z.; Du, B.; Zhang, M.; Liu, J. Reluplex made more practical: Leaky ReLU. In Proceedings of the 2020 IEEE Symposium on Computers and Communications (ISCC), Rennes, France, 7–10 July 2020; IEEE: Piscataway, NJ, USA, 2020; pp. 1–7.
26. Han, D.; Yun, S.; Heo, B.; Yoo, Y. Rethinking channel dimensions for efficient model design. In Proceedings of the IEEE/CVF Conference on Computer Vision and Pattern Recognition, Nashville, TN, USA, 19–25 June 2021; pp. 732–741.
27. Bi, C.; Wang, J.; Duan, Y.; Fu, B.; Kang, J.R.; Shi, Y. MobileNet based apple leaf diseases identification. *Mob. Netw. Appl.* **2022**, *27*, 172–180. [CrossRef]
28. Sun, J.; Tan, W.; Wu, X.; Shen, J.; Lu, B.; Dai, C. Real-time recognition of sugar beet and weeds in complex backgrounds using multi-channel depth-wise separable convolution model. *Trans. Chin. Soc. Agric. Eng. (Trans. CSAE)* **2019**, *35*, 184–190.
29. Zhao, X.; Song, Y. Improved Ship Detection with YOLOv8 Enhanced with MobileViT and GSConv. *Electronics* **2023**, *12*, 4666. [CrossRef]
30. Lin, T.Y.; Dollár, P.; Girshick, R.; He, K.; Hariharan, B.; Belongie, S. Feature pyramid networks for object detection. In Proceedings of the IEEE Conference on Computer Vision and Pattern Recognition, Honolulu, HI, USA, 21–26 July 2017; pp. 2117–2125.
31. Qiu, M.; Huang, L.; Tang, B.H. Bridge detection method for HSRRSIs based on YOLOv5 with a decoupled head. *Int. J. Digit. Earth* **2023**, *16*, 113–129. [CrossRef]
32. Fang, G.; Ma, X.; Song, M.; Mi, M.B.; Wang, X. Depgraph: Towards any structural pruning. In Proceedings of the IEEE/CVF Conference on Computer Vision and Pattern Recognition, Vancouver, BC, Canada, 18–22 June 2023; pp. 16091–16101.
33. Han, K.; Wang, Y.; Tian, Q.; Guo, J.; Xu, C.; Xu, C. Ghostnet: More features from cheap operations. In Proceedings of the IEEE/CVF Conference on Computer Vision and Pattern Recognition, Seattle, DC, USA, 14–19 June 2020; pp. 1580–1589.
34. Tang, Y.; Han, K.; Guo, J.; Xu, C.; Xu, C.; Wang, Y. GhostNetv2: Enhance cheap operation with long-range attention. *Adv. Neural Inf. Process. Syst.* **2022**, *35*, 9969–9982.
35. Chen, J.; Kao, S.h.; He, H.; Zhuo, W.; Wen, S.; Lee, C.H.; Chan, S.H.G. Run, Don't walk: Chasing higher FLOPS for faster neural networks. In Proceedings of the IEEE/CVF Conference on Computer Vision and Pattern Recognition, Vancouver, BC, Canada, 18–22 June 2023; pp. 12021–12031.
36. Howard, A.; Sandler, M.; Chu, G.; Chen, L.C.; Chen, B.; Tan, M.; Wang, W.; Zhu, Y.; Pang, R.; Vasudevan, V.; et al. Searching for mobilenetv3. In Proceedings of the IEEE/CVF International Conference on Computer Vision, Seoul, Republic of Korea, 27 October–2 November 2019; pp. 1314–1324.
37. Molchanov, P.; Mallya, A.; Tyree, S.; Frosio, I.; Kautz, J. Importance estimation for neural network pruning. In Proceedings of the IEEE/CVF Conference on Computer Vision and Pattern Recognition, Long Beach, CA, USA, 15–20 June 2019; pp. 11264–11272.
38. LeCun, Y.; Denker, J.; Solla, S. Optimal brain damage. *Adv. Neural Inf. Process. Syst.* **1989**, *2*, 598–605.
39. Selvaraju, R.R.; Cogswell, M.; Das, A.; Vedantam, R.; Parikh, D.; Batra, D. Grad-cam: Visual explanations from deep networks via gradient-based localization. In Proceedings of the IEEE International Conference on Computer Vision, Venice, Italy, 22–29 October 2017; pp. 618–626.

3.3.2 Predicting the Evolution of Capacity Degradation Histograms of Rechargeable Batteries Under Dynamic Loads via Latent Gaussian Processes（B 类）

energies

MDPI

Article

Predicting the Evolution of Capacity Degradation Histograms of Rechargeable Batteries Under Dynamic Loads via Latent Gaussian Processes

Daocan Wang [1,2], Xinggang Li [2,*] and Jiahuan Lu [3,*]

[1] School of Artificial Intelligence and Automation, Huazhong University of Science and Technology, Wuhan 430074, China
[2] China North Vehicle Research Institute, Beijing 100072, China
[3] College of Engineering, South China Agricultural University, Guangzhou 510642, China
* Correspondence: lixinggang2701@163.com (X.L.); jhlu@scau.edu.cn (J.L.)

Abstract

Accurate prediction of lithium-ion battery capacity degradation under dynamic loads is crucial yet challenging due to limited data availability and high cell-to-cell variability. This study proposes a Latent Gaussian Process (GP) model to forecast the full distribution of capacity fade in the form of high-dimensional histograms, rather than relying on point estimates. The model integrates Principal Component Analysis with GP regression to learn temporal degradation patterns from partial early-cycle data of a target cell, using a fully degraded reference cell. Experiments on the NASA dataset with randomized dynamic load profiles demonstrate that Latent GP enables full-lifecycle capacity distribution prediction using only early-cycle observations. Compared with standard GP, long short-term memory (LSTM), and Monte Carlo Dropout LSTM baselines, it achieves superior accuracy in terms of Kullback–Leibler divergence and mean squared error. Sensitivity analyses further confirm the model's robustness to input noise and hyperparameter settings, highlighting its potential for practical deployment in real-world battery health prognostics.

Keywords: capacity histograms; prediction; rechargeable batteries; degradation

Academic Editor: JongHoon Kim

Received: 23 May 2025
Revised: 23 June 2025
Accepted: 23 June 2025
Published: 2 July 2025

Citation: Wang, D.; Li, X.; Lu, J. Predicting the Evolution of Capacity Degradation Histograms of Rechargeable Batteries Under Dynamic Loads via Latent Gaussian Processes. *Energies* **2025**, *18*, 3503. https://doi.org/10.3390/en18133503

1. Introduction

1.1. Literature Review

Rechargeable batteries, particularly lithium-ion batteries, have gained widespread global application across important fields such as electric vehicles [1], energy storage stations [2], and portable devices [3]. However, even under regular operating conditions, repeated charge and discharge cycling inevitably induces degradation processes, primarily including solid electrolyte interphase (SEI) layer growth leading to irreversible lithium loss, and active material loss reducing lithium storage capacity [4–6]. These degradation mechanisms are strongly influenced by usage profiles, and their cumulative effects typically manifest as observable capacity fade that intensifies over cycling [7,8]. Thus, understanding and predicting battery capacity degradation is crucial for battery configuration and management, helping to prevent unexpected performance losses and safety hazards during usage.

Battery capacity degradation trajectory prediction has long been a core topic in battery research. Early studies focused on developing mathematical models that established relationships between cycle count and capacity degradation trends, using functions such

as linear, polynomial, or exponential models to quantify future degradation [9–11]. Other approaches utilized recursive models, including autocorrelation models and autoregressive integrated moving average (ARIMA) models, to predict future capacity based on historical data [12–14]. While these foundational methods provided useful quantitative frameworks, they have been continually refined and improved upon over time, giving rise to more sophisticated models. Notably, some studies have integrated electrochemical modeling into capacity degradation prediction to enhance physical interpretability. Lyu et al. [15] identified key degradation-related physical parameters using an electrochemical model and extrapolated their evolution via exponential functions to forecast capacity fade. Ren et al. [16] developed a capacity degradation model by coupling a pseudo-two-dimensional electrochemical model, a three-dimensional thermal model, and an SEI formation model, enabling recursive prediction of future capacity loss. Although such semi-quantum models show promise in improving interpretability, their application in real-world scenarios remains limited due to data scarcity and computational complexity. Recent advancements in deep learning technologies have led to the development of even more advanced models, such as neural networks, which aim to bridge the gap between historical data and future predictions [17,18]. For instance, Huang et al. [19] utilized long short-term memory (LSTM) and convolutional neural networks (CNNs) to predict capacity trajectories by incorporating historical capacity, rest time, and internal resistance. Zhao et al. [20] applied multi-channel dependent neural networks to map incremental capacity and capacity differentials to critical future degradation points. Yang et al. [21] employed a CNN–Transformer–Kolmogorov–Arnold network to connect historical charging data with future capacity degradation. Similarly, Du et al. [22] bridged the relationship between historical charge/discharge cycles and future capacity degradation through CNNs. While these approaches have achieved success, they mostly rely on assumptions of constant load conditions, ignoring the dynamic load environments that batteries encounter in real-world applications [23]. As a result, their predictive outcomes may lack practical relevance, particularly when batteries operate under complex dynamic conditions.

In recent years, dynamic load-based battery capacity degradation prediction has emerged as a key research focus. Notably, the National Aeronautics and Space Administration (NASA) released a dataset detailing battery degradation under dynamic load conditions, revealing a nonlinear scatter in capacity degradation, which formed a capacity distribution rather than a single trajectory [24–26]. This starkly contrasts with the continuous degradation trends observed under constant load in earlier studies, prompting widespread academic interest in dynamic load effects on battery performance. Lu et al. [27] further analyzed battery capacity degradation under uncertain current excitation, revealing nonlinear oscillation patterns that emerge when current excitation changes unpredictably. They proposed a method for accurately predicting degradation based on future dynamic excitation plans. Subsequent research [28] confirmed that battery performance during charging and discharging varies based on load conditions, reinforcing the need to consider dynamic loads in capacity predictions.

While these studies incorporate future load plans to account for load capacity dependency, accurate prediction of such plans remains a prerequisite. Obtaining precise future load plans in practical applications is challenging, and the limited availability of degradation samples further complicates the predictive process [29,30]. Therefore, predicting future capacity histograms under dynamic loads without explicit knowledge of future load plans remains a critical issue to address.

To overcome these challenges, this paper presents a Latent Gaussian Process (LGP)-based method for predicting battery capacity histograms, particularly under dynamic load conditions. The contributions of this study are as follows:

(1) Dynamic load capacity prediction: This paper proposes a method for predicting battery capacity degradation histograms that reflect dynamic load conditions, offering a more accurate representation of degradation in real-world scenarios.

(2) Prediction of capacity degradation histograms: In contrast to traditional trajectory-based predictions, this work provides probability histograms of future degradation based on historical distribution patterns, delivering more comprehensive prediction results.

(3) Adaptability to small sample sizes: Compared to deep learning techniques, this approach excels in scenarios with limited data, effectively predicting capacity degradation even with sparse datasets, without the heavy reliance on large data volumes required by deep learning models.

1.2. Article Organization

The rest of the article is organized as follows. Section 2 presents the methodology, followed by Section 3, which discusses the experimental results and performance analysis. Finally, conclusions are drawn in Section 4.

2. Methodology

2.1. Framework of Methodology

The proposed framework aims to predict the future capacity degradation distribution of lithium-ion batteries under dynamic operating conditions. As illustrated in Figure 1, the proposed method consists of three main stages: histogram construction, latent space modeling, and probabilistic forecasting via Gaussian processes.

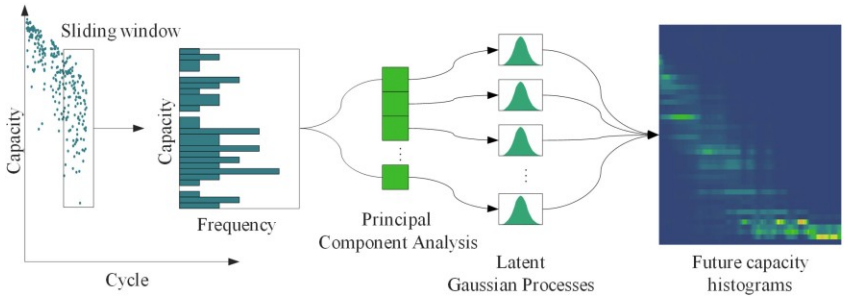

Figure 1. Overview of the proposed prediction framework.

First, a sliding window is applied to the capacity degradation trajectory of the target battery, converting sequential capacity values into a series of histograms that describe the statistical distribution of capacity within each window. This histogram representation transforms the problem from single-point prediction into a distributional forecasting task, allowing the model to capture the inherent stochasticity of battery degradation.

Next, the high-dimensional histograms are projected into a lower-dimensional latent space using principal component analysis. This step extracts the dominant components that capture the major variations in degradation behavior, significantly reducing computational complexity and noise sensitivity.

Then, each principal component is modeled using a separate Gaussian Process. These GPs learn the temporal evolution of latent variables across different cycles, enabling robust extrapolation beyond the observed data.

Finally, the predicted latent components are reconstructed back into the histogram space, yielding forecasts of the full capacity degradation distribution over future cycles.

This approach ensures that inter-bin correlations are preserved and uncertainty is naturally quantified via the GP's posterior variance.

2.2. Battery Capacity Histogram Definition

The battery capacity histogram at the t-th cycle can be represented by a histogram over a sliding window:

$$\boldsymbol{H}(t) = [h_1(t), h_2(t), \ldots, h_K(t)],\ t = 1, 2, \ldots, T \tag{1}$$

where $\boldsymbol{H}(t)$ is the battery capacity histogram at the t-th cycle, K is the total number of bins and $h_k(t)$ is the frequency of capacity in the k-th bin, which is expressed as follows:

$$h_k(t) = \sum_{i=1}^{W} g(Q_i(t) \in B_k) \tag{2}$$

where W is the length of the sliding window, $Q_i(t)$ is the capacity value at the t-th cycle for the i-th measurement within the sliding window, $g(\cdot)$ is the indicator function, which is 1 if the condition inside the parentheses is true (i.e., if the capacity value $Q_i(t)$ falls within bin B_k) and 0 otherwise, and B_k denotes the k-th bin of the predefined capacity histogram, covering a fixed range of capacity values, which can be described as follows:

$$B_k = [Q_{\min} + (k-1) \cdot \Delta Q, Q_{\min} + k \cdot \Delta Q) \tag{3}$$

where ΔQ is the capacity step size, which can be specified based on the chosen resolution, $Q_{\min}$ is the capacity failure threshold and k is the bin index, which ranges from 1 to K. The sum of the histogram bins at each cycle corresponds to the length of the sliding window, as it reflects the number of samples within the sliding window:

$$\sum_{k=1}^{K} h_k(t) = W \tag{4}$$

2.3. Principal Component Analysis

Principal Component Analysis (PCA) [31] is used in this paper to reduce the dimensionality of the observed battery capacity histograms, $\boldsymbol{H}(t)$, and project them into a latent space where the most significant patterns of capacity degradation can be more effectively modeled. Each capacity degradation trajectory is initially represented as a high-dimensional distribution, where each cycle of degradation corresponds to a capacity histogram with multiple bins. However, to model the degradation process effectively, we first reduce the dimensionality of these histograms. This reduction is performed by PCA, which projects the high-dimensional data into a lower-dimensional latent space.

This approach is one of the key reasons why the method is referred to as a Latent Gaussian Process. Instead of directly applying the Gaussian process to the high-dimensional capacity histograms, we first apply PCA to $\boldsymbol{H}(t)$, reducing the data to K-dimensional latent variables. These reduced components are then used as inputs for Gaussian process regression, significantly simplifying the modeling process. This latent space transformation allows us to capture the key features of the degradation behavior while discarding less important details, providing a more efficient and accurate modeling approach.

To prepare the data for PCA, we first center and standardize the capacity histograms $\boldsymbol{H}(t)$ at each cycle. Centering ensures that each distribution has zero mean, and standardization ensures that each feature has unit variance, making the data suitable for PCA:

$$\boldsymbol{H}_c(t) = \boldsymbol{H}(t) - \mu_H \tag{5}$$

where μ_H represents the mean capacity distribution across all cycles.

Next, we calculate the covariance matrix $\boldsymbol{C}$, which captures the relationships between the different bins of the capacity histograms:

$$\boldsymbol{C} = \frac{1}{N-1}\boldsymbol{H}_{\mathrm{c}}(t)^{\mathrm{T}}\boldsymbol{H}_{\mathrm{c}}(t) \tag{6}$$

where N is the number of cycles. This covariance matrix is essential for PCA to identify the correlations between capacity bins.

PCA involves solving the eigenvalue problem for the covariance matrix $\boldsymbol{C}$. The eigenvectors $\boldsymbol{v}_k$ represent the principal components, and the eigenvalues λ_k correspond to the variance explained by each component:

$$\boldsymbol{C}\boldsymbol{v}_k = \boldsymbol{v}_k\,\lambda_k \tag{7}$$

These eigenvectors are ordered by the magnitude of their corresponding eigenvalues, and the principal components with the largest eigenvalues are selected for the latent space.

After identifying the principal components, we project the centered data $\boldsymbol{H}_{\mathrm{c}}(t)$ onto the space spanned by these components:

$$\boldsymbol{Z}(t) = \boldsymbol{H}_{\mathrm{c}}(t)\boldsymbol{V} \tag{8}$$

where $\boldsymbol{Z}(t)$ is the data projected into the lower-dimensional latent space and $\boldsymbol{V}$ is the matrix of eigenvectors (principal components).

The number of principal components d is selected based on the explained variance. We choose d such that the cumulative explained variance exceeds a threshold, ensuring that the most significant patterns in the data are retained. In our case, $d = 5$ components are chosen to represent the most critical variations in capacity degradation behavior, while reducing dimensionality:

$$E = \frac{\sum_{k=1}^{d}\lambda_k}{\sum_{k=1}^{K}\lambda_k} \tag{9}$$

where E is the explained variance ratio. This step ensures that the latent space captures the key degradation features and provides a compact representation of the original high-dimensional data.

2.4. Gaussian Processes

In this study, we perform Gaussian process regression [32] on each of the d principal components derived from the PCA process. Let $\boldsymbol{Z}(t) = [z_1(t), z_2(t), \ldots, z_d(t)]^{\mathrm{T}}$ denote the vector of latent variables (principal components) at cycle t, which corresponds to the battery capacity histogram $\boldsymbol{H}(t)$ projected into the lower-dimensional latent space using PCA. Each component $z_k(t)$ represents the value of the k-th principal component at cycle t.

For each $k \in \{1, 2, \ldots, d\}$, a separate GPR model is used to predict the trajectory of the corresponding latent variable $z_k(t)$ over cycle. The general form of the model for each principal component $z_k(t)$ is given by

$$z_k(t) = f_k(t) + \varepsilon_k(t) \tag{10}$$

where $f_k(t)$ represents the underlying smooth function that governs the evolution of the k-th principal component over time and $\varepsilon_k(t)$ is the Gaussian noise term, capturing the uncertainty or errors in the observations of the k-th component.

Each $f_k(t)$ can be modeled as a Gaussian Process:

$$z_k(t) \sim GP(\mu_k(t), k_k(t, t\prime)) \tag{11}$$

where $\mu_k(t)$ is the mean function, which is assumed to be zero, and $k_k(t, t')$ is the covariance function (kernel), which defines the correlation between cycles for the k-th component. A typical choice for the kernel is the squared exponential kernel, which ensures smoothness and captures correlations between nearby cycles.

The GPR models are trained separately for each of the d principal components, with the observed data used to infer the latent function $f_k(t)$ and the noise term $\varepsilon_k(t)$. After training, these models can predict future values of the $z_k(t)$, allowing us to forecast the battery capacity degradation in the latent space. These predicted latent components $\mathbf{Z}_{\text{pred}}(t)$ are then combined with the inverse PCA transformation to reconstruct the future capacity histograms $\boldsymbol{Y}_{\text{pred}}(t)$:

$$\boldsymbol{Y}_{\text{pred}}(t) = \mathbf{Z}_{\text{pred}}(t)\boldsymbol{V}^{\text{T}} + \mu \tag{12}$$

To obtain normalized histogram values, we apply the Softmax function [33] and scale the predictions by the length of the sliding window to ensure the total sum of the distribution is W:

$$\boldsymbol{Y}^{\text{norm}}_{\text{pred}}(t) = W \cdot \text{Softmax}(\boldsymbol{Y}_{\text{pred}}(t)) \tag{13}$$

where $\boldsymbol{Y}^{\text{norm}}_{\text{pred}}(t)$ is the final output of the proposed method.

2.5. Evaluation Metrics

The performance of the prediction model is evaluated using two key metrics: Kullback–Leibler (KL) divergence and mean squared error (MSE) [34].

The Kullback–Leibler divergence KL measures the difference between the true and predicted distributions, which can be computed as follows:

$$KL = \sum_{k=1}^{K} y^{\text{norm}}_{\text{true},k} \log\left(\frac{y_{\text{true},k}}{y^{\text{norm}}_{\text{pred},k}}\right) \tag{14}$$

The mean squared error MSE evaluates the overall error between the true and predicted distributions, which can be defined as follows:

$$MSE = \frac{1}{K}\sum_{k=1}^{K} (y_{\text{true},k} - y^{\text{norm}}_{\text{pred},k})^2 \tag{15}$$

3. Results

3.1. Datasets

To evaluate the performance of the proposed latent Gaussian process-based model in predicting capacity histogram evolution under dynamic loads, we employed the Randomized Battery Usage 7: Low-Temperature Left-Skewed Random Walk dataset provided by NASA's Prognostics Center of Excellence. This dataset comprises four commercial 18,650 lithium-ion cells (identified as RW13, RW14, RW15, and RW16) that were continuously cycled under a randomized loading protocol designed to emulate real-world current variability. In each cycle, the batteries were first charged to 4.2 V using a constant-current/constant-voltage (CC/CV) scheme and then discharged to 3.2 V following a random walk discharge pattern. During discharge, the current setpoint was updated every 60 s. The new current value was drawn from a customized left-skewed probability distribution favoring lower currents. The available setpoints ranged from 0.5 A to 5.0 A, with selection

probabilities as follows: 0.5 A (7.2%), 1.0 A (14.8%), 1.5 A (19.3%), 2.0 A (21.6%), 2.5 A (14.6%), 3.0 A (10.0%), 3.5 A (6.5%), 4.0 A (4.0%), 4.5 A (1.5%), and 5.0 A (0.5%).

The discharge capacity degradation of four cells (i.e., RW13, RW14, RW15, and RW16) over time under dynamic current loads are shown in Figure 2. It is worth noting that the RW16 curve in Figure 2d presents a visible gap between mid-November and mid-December 2014, which reflects a discontinuity in the original dataset rather than any data preprocessing issue. The results highlight that despite identical testing protocols, the degradation behaviors of different cells under randomized dynamic loads exhibit significant variability. The dynamic loading conditions lead to capacity degradation patterns that are not confined to a single trajectory but instead manifest as dispersed scatter trends. Moreover, the degree of dispersion increases with cycling, emphasizing the stochastic nature of battery aging. This further validates the necessity of capturing the distribution of capacity degradation rather than relying solely on deterministic point estimates when predicting battery health under realistic operating conditions.

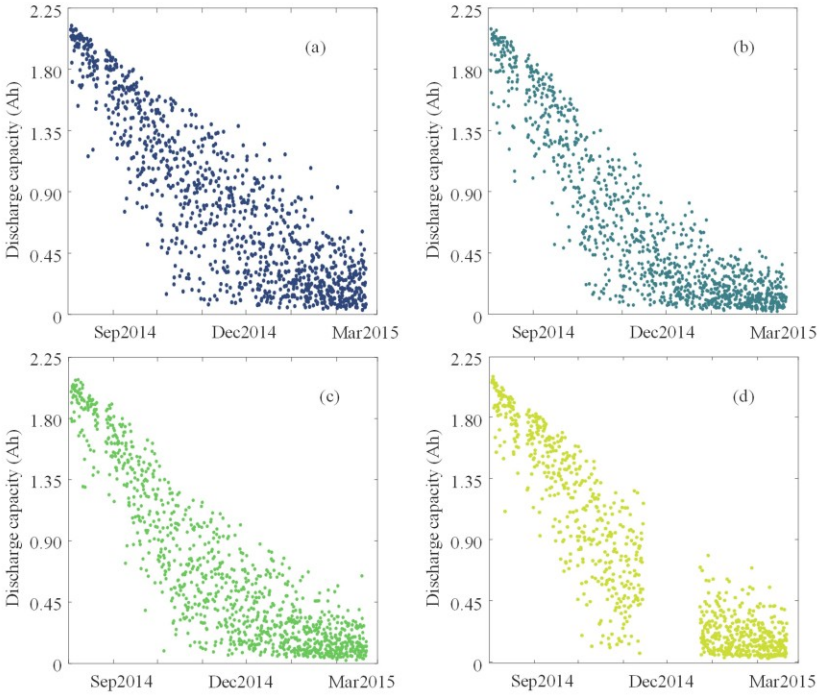

Figure 2. Scatter plot of battery discharge capacity degradation under dynamic load: (**a**) RW13; (**b**) RW14; (**c**) RW15; (**d**) RW16.

3.2. Predictive Performance

To evaluate the predictive performance of the proposed method under a practical small-sample setting, we consider a scenario where the complete degradation trajectory of battery RW13 is available, while only the first 100 cycles of RW14, RW15, and RW16 are observed. The objective is to predict the capacity degradation histograms of RW14–RW16 from the 100th cycle until end-of-life. The prediction results are illustrated in Figure 3.

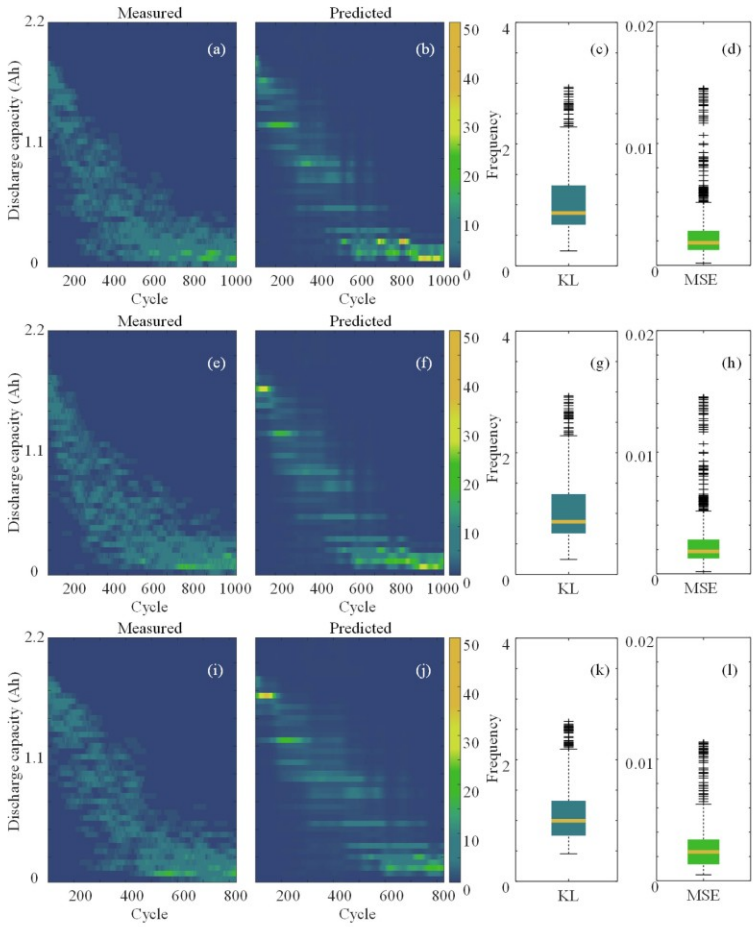

Figure 3. Prediction results on RW14, RW15, and RW16 using the proposed method. (**a**,**e**,**i**): Measured histograms. (**b**,**f**,**j**): Predicted histograms. (**c**,**g**,**k**) and (**d**,**h**,**l**): KL divergence and MSE boxplots from cycle 100 onward.

As shown in Figure 3a,e,i, the actual degradation histograms of RW14–RW16 exhibit considerable variability despite identical test protocols. Nevertheless, leveraging the full degradation data from RW13 and the early-cycle data from each target battery, the proposed method accurately reconstructs the capacity degradation histograms, closely matching the measured histograms in Figure 3b,f,j.

To quantitatively assess prediction accuracy, we report the KL divergence and MSE between the predicted and actual histograms in Figure 3c,g,k and Figure 3d,h,l, respectively. The results show that the maximum KL divergence remains below 3, with the median value under 2, indicating strong distributional consistency. Meanwhile, the maximum MSE does not exceed 0.16, and the median remains below 0.03, confirming the high fidelity of the predicted degradation patterns.

These results demonstrate that the proposed approach can effectively infer future degradation histograms using limited early-cycle data, offering a promising solution for data-efficient battery lifetime prognosis under dynamic operational conditions.

3.3. Comparison with Conventional Baselines

To demonstrate the effectiveness of the proposed Latent GP method, we design three comparative baseline models. The first baseline uses a standard GP without dimensionality reduction, directly modeling the high-dimensional capacity degradation histograms. This model shares the same hyperparameters as the proposed Latent GP to ensure a fair comparison. The second baseline employs an LSTM network, a widely used deep learning approach for time-series forecasting. The LSTM network takes the sliding window of historical capacity histograms as input and iteratively predicts future distributions. The network consists of two LSTM layers (each with 30 hidden units), followed by a fully connected layer for dimensional mapping and ReLU activation to ensure non-negativity of the output. It was trained for 200 epochs using the ADAM optimizer with a learning rate of 0.02 and MSE as the loss function. The third baseline introduces a Monte Carlo Dropout LSTM model, which shares the same architecture and training setup as the standard (MC) LSTM but adds dropout layers with a rate of 0.3 before each LSTM and fully connected layer. During inference, dropout is retained to enable stochastic forward passes that approximate a Bayesian posterior distribution [35]. A total of 30 such passes are performed at each prediction step, and the final prediction is obtained by averaging the results. These comparisons were conducted under the same setup: RW13 served as the reference battery with complete capacity degradation data, and RW14 was the target battery. Predictions began at the 100th cycle. The results are shown in Figure 4.

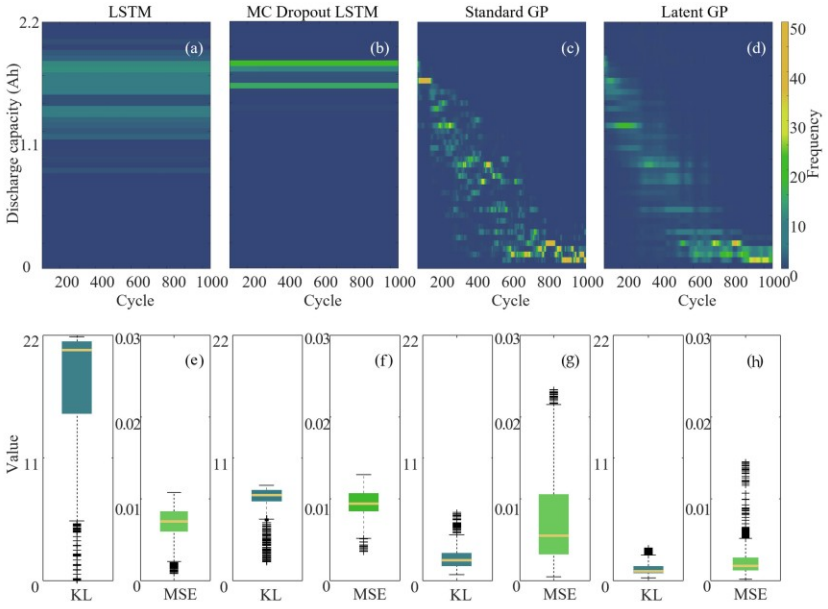

Figure 4. Predictions on RW14 using RW13 as the source, starting from cycle 100. (**a**–**d**): Results from LSTM, MC Dropout LSTM, standard GP, and Latent GP. (**e**–**h**): Corresponding KL divergence and MSE.

Figure 4a–d illustrate that the Latent GP most closely reproduces the measured degradation histograms (cf. Figure 3a). In contrast, the LSTM and MC Dropout LSTM models fail to capture the degradation patterns over time. The MC Dropout variant provides slightly less noisy predictions than the deterministic LSTM but still lacks the ability to track capacity decline. The standard GP performs better than both LSTM-based models but remains less accurate than the Latent GP. Its scattered predictions may result from its inability to model the dominant components of degradation processes.

Figure 4e–h quantify performance using KL divergence and MSE. The LSTM model exhibits the highest KL divergence, often exceeding 20, indicating a significant mismatch with the true distribution. The MC Dropout LSTM reduces the KL divergence to below 9 and achieves a median MSE around 0.01, suggesting that Bayesian approximation improves generalization and robustness. The standard GP maintains KL divergence below 7 but reaches an MSE above 0.02. In contrast, the Latent GP achieves both KL divergence below 3 and MSE below 0.015. These gains are attributed to the use of PCA, which captures the intrinsic structure of histogram evolution and enhances long-term forecast stability.

3.4. Performance with Different Starting Points

To explore the predictive performance under varying data availability, we conducted simulations assuming the complete capacity degradation data of the RW13 battery is known. The target battery in this analysis is RW14. We varied the starting point of prediction, altering the ratio between available historical data and the future degradation trajectory to be predicted. Specifically, the starting points were set at cycles 1, 50, 100, 200, and 500 to simulate different levels of prior information.

The boxplots for KL divergence (Figure 5a) and MSE (Figure 5b) are shown for each starting point. As the number of available cycles increases, both the KL divergence and MSE reduce, indicating that a higher proportion of historical data contributes to improved prediction accuracy. Specifically, when starting from cycle 1, the predictions exhibit higher divergence and error, which steadily decrease as more cycles are included for training. Starting from cycle 100 and beyond provides relatively stable prediction results, with the KL divergence and MSE values remaining low, indicating that predictions based on a larger portion of historical data are more accurate.

These results suggest that the predictive performance improves significantly when more historical data are incorporated, emphasizing the importance of early-cycle data in refining capacity degradation forecasts.

3.5. Sensitivity Analysis

Sensitivity analysis helps evaluate the robustness of the LGP method to design choices and input variations. Thus, we perform a sensitivity analysis focusing on three aspects: the number of principal components retained, the resolution of the capacity histogram (i.e., the number of bins), and the impact of noise in early-cycle data. These experiments are conducted under the same prediction setup used throughout the paper, where the full degradation trajectory of battery RW13 is used for training, and only the first 100 cycles of RW14 are observed for prediction.

We first vary the number of retained principal components in the PCA step. As shown in Figure 6a,d, the model performs best when 3–5 components are kept, balancing dimensionality reduction with information preservation. Including too few components underrepresents structural trends, while including too many can introduce noise, leading to increased prediction error.

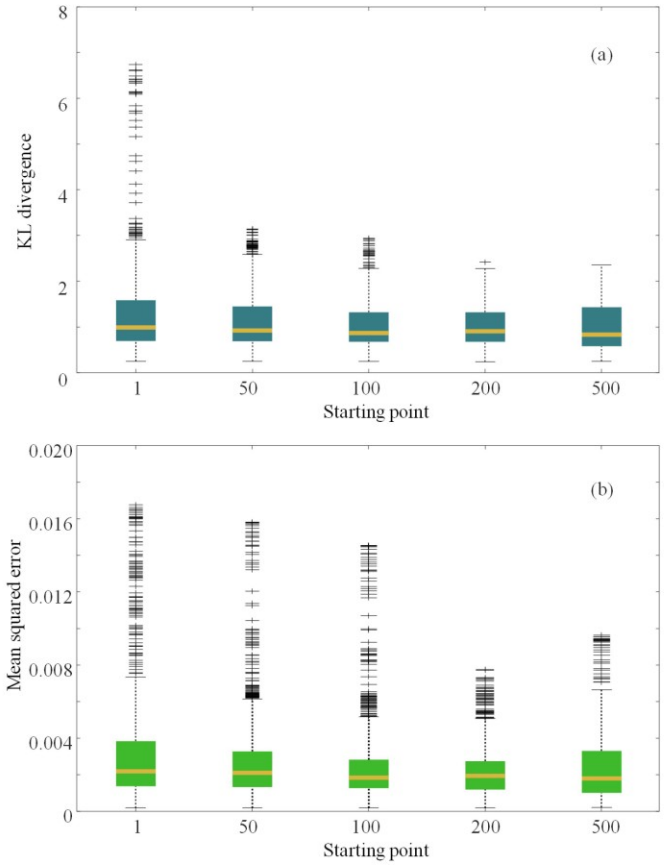

Figure 5. KL divergence (**a**) and MSE (**b**) for predictions starting at cycles 1, 50, 100, 200, and 500.

The effect of histogram resolution is examined by changing the bin width used to discretize capacity into histograms. Specifically, capacity step sizes of 0.1 Ah, 0.05 Ah, 0.025 Ah, and 0.0125 Ah are used, resulting in 23, 45, 89, and 177 bins, respectively. As shown in Figure 6b,e, increasing the number of bins generally reduces the mean squared error (MSE), as finer resolution enables better matching of local histogram structures. However, a noticeable increase in KL divergence is observed at the highest resolution (177 bins). This discrepancy between MSE and KL behavior arises because KL divergence captures the overall distributional shape rather than localized errors. When the histogram has many bins, many of them may become sparsely populated or empty. Although such sparsity reduces the absolute error in individual bins (hence the lower MSE), even minor deviations in the prediction can accumulate across many bins, leading to amplified differences in the probability distribution and thus a higher KL divergence. Furthermore, retaining a fixed number of principal components in the PCA step may limit the model's capacity to fully preserve fine-grained histogram features when the number of bins increases. Since PCA reduces dimensionality based on variance concentration, subtle details captured in high-

resolution histograms may be compressed or lost. This trade-off between representation resolution and latent feature fidelity may also contribute to the divergence trends observed in Figure 6b,e.

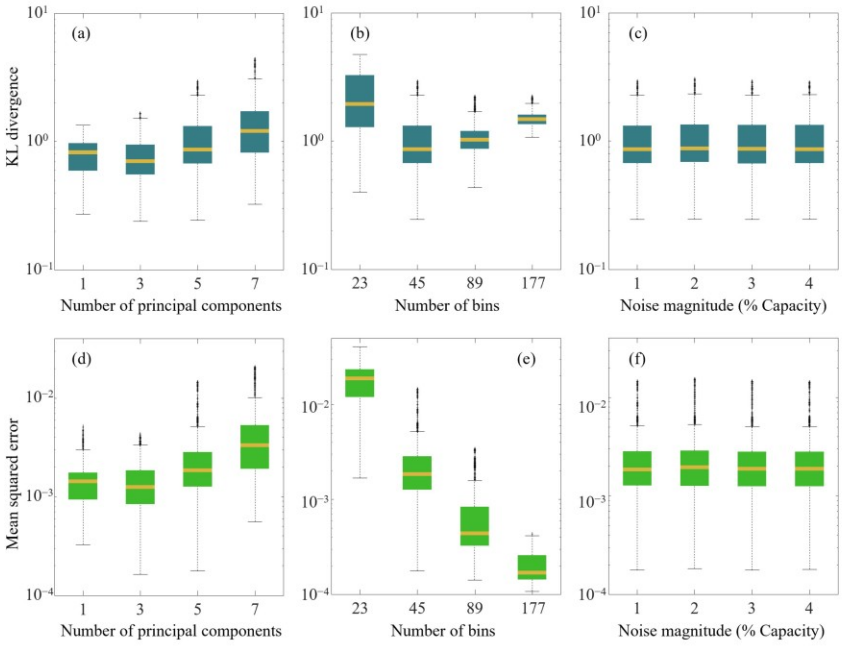

Figure 6. Sensitivity analysis: (**a**,**d**) impact of number of retained principal components; (**b**,**e**) impact of capacity histogram resolution (bin count); (**c**,**f**) impact of early-cycle capacity noise level. Top row: KL divergence; bottom row: MSE.

To evaluate robustness to early-cycle measurement uncertainty, we introduce zero-mean Gaussian white noise to the first 100 capacity values of RW14, with the noise standard deviation set to 1%, 2%, 3%, and 4% of the battery initial capacity. As illustrated in Figure 6c,f, the LGP method demonstrates good stability across all tested noise levels. The KL divergence and MSE remain relatively unchanged, suggesting that the model can tolerate moderate levels of input noise without significant degradation in predictive performance.

These results indicate that the LGP framework is resilient to moderate parameter perturbations and input uncertainty, supporting its potential for deployment in real-world battery life prognosis scenarios.

4. Conclusions

This paper presents a Latent GP model for predicting high-dimensional capacity degradation histograms of lithium-ion batteries under dynamic load conditions. The method combines PCA for latent feature extraction with Gaussian Process regression for temporal prediction, enabling accurate distribution forecasting from limited early-cycle data.

We validated the approach using the publicly available NASA PCoE lithium-ion battery dataset. In our experiments, battery RW13 served as the reference cell with full

degradation data, while RW14, RW15, and RW16 were used as target cells with only partial data available from the first 100 cycles. The proposed method demonstrated strong predictive performance, with KL divergence consistently remaining below 3 and the median MSE below 0.03. Compared to the conventional Gaussian Process method and a two-layer LSTM baseline, the Latent GP produced more accurate and less scattered forecasts of the capacity degradation histograms. In addition, the model maintained stable prediction accuracy across different starting points for forecasting, including the 1st, 50th, 100th, 200th, and 500th cycle, indicating its robustness under conditions of limited data availability.

Although this study was conducted using the commercial 18,650 cells from the NASA dataset, the proposed method is inherently data-driven and does not rely on specific electrochemical formulations. As long as historical capacity degradation data are available, the Latent GP model can, in principle, be extended to batteries with different cathode chemistries.

Future extensions could incorporate cross-cell correlation modeling, generalization to multi-chemistry datasets, and real-time online learning strategies for deployment in embedded battery management systems.

Author Contributions: Conceptualization, J.L. and X.L.; methodology, D.W. and J.L.; validation, D.W. and X.L.; writing—original draft preparation, D.W.; writing—review and editing, J.L. and X.L. All authors have read and agreed to the published version of the manuscript.

Funding: This research was funded by the National Natural Science Foundation of China, Grant Nos. 52441702 and 52407246; Guangdong Basic and Applied Basic Research Foundation, Grant No. 2025A1515010354; Guangzhou Science and Technology Plan, Grant No. 2025A04J3660; Specific University Discipline Construction Project, Grant No. 2023B10564002.

Data Availability Statement: The battery degradation dataset used in this study is publicly available from the NASA Prognostics Center of Excellence. It can be accessed at https://www.nasa.gov/content/prognostics-center-of-excellence-data-set-repository (accessed on 20 May 2025).

Conflicts of Interest: Authors Daocan Wang and Xinggang Li were employed by the company China North Vehicle Research Institute. The remaining authors declare that the research was conducted in the absence of any commercial or financial relationships that could be construed as a potential conflict of interest.

References

1. Adhikari, N.; Bhandari, R.; Joshi, P. Thermal analysis of lithium-ion battery of electric vehicle using different cooling medium. *Appl. Energy* **2024**, *360*, 122781. [CrossRef]
2. Balasundar, C.; Sundarabalan, C.K.; Santhanam, S.N.; Sharma, J.; Guerrero, J.M. Mixed Step Size Normalized Least Mean Fourth Algorithm of DSTATCOM Integrated Electric Vehicle Charging Station. *IEEE Trans. Ind. Inform.* **2023**, *19*, 7583–7591. [CrossRef]
3. Kuzovchikov, S.M.; Zefirov, V.V.; Neudachina, V.S.; Zakharchenko, T.K.; Zybkovets, A.L.; Nikiforov, A.A.; Gusak, D.I.; Reveguk, A.; Kondratenko, M.S.; Yashina, L.V.; et al. Electrolyte refilling as a way to recover capacity of aged lithium-ion batteries. *J. Power Sources* **2024**, *601*, 234257. [CrossRef]
4. Teliz, E.; López-Vázquez, C.; Díaz, V. Degradation study for 18650 NMC batteries at low temperature. *Electrochim. Acta* **2024**, *475*, 143540. [CrossRef]
5. You, H.; Wang, X.; Zhu, J.; Jiang, B.; Han, G.; Wei, X.; Dai, H. Investigation of lithium-ion battery nonlinear degradation by experiments and model-based simulation. *Energy Storage Mater.* **2024**, *65*, 103083. [CrossRef]
6. Li, W.; Li, Y.; Garg, A.; Gao, L. Enhancing real-time degradation prediction of lithium-ion battery: A digital twin framework with CNN-LSTM-attention model. *Energy* **2024**, *286*, 129681. [CrossRef]
7. Oh, S.; Jeon, A.-R.; Lim, G.; Cho, M.K.; Chae, K.H.; Sohn, S.S.; Lee, M.; Jung, S.-K.; Hong, J. Fast discharging mitigates cathode-electrolyte interface degradation of $LiNi_{0.6}Mn_{0.2}Co_{0.2}O_2$ in rechargeable lithium batteries. *Energy Storage Mater.* **2024**, *65*, 103169. [CrossRef]
8. Ansari, S.; Ayob, A.; Hossain Lipu, M.S.; Hussain, A.; Md Saad, M.H. Jellyfish optimized recurrent neural network for state of health estimation of lithium-ion batteries. *Expert Syst. Appl.* **2024**, *238*, 121904. [CrossRef]
9. Xiong, R.; Zhang, Y.; Wang, J.; He, H.; Peng, S.; Pecht, M. Lithium-Ion Battery Health Prognosis Based on a Real Battery Management System Used in Electric Vehicles. *IEEE Trans. Veh. Technol.* **2019**, *68*, 4110–4121. [CrossRef]

10. Xing, Y.; Ma, E.W.M.; Tsui, K.L.; Pecht, M. An ensemble model for predicting the remaining useful performance of lithium-ion batteries. *Microelectron. Reliab.* **2013**, *53*, 811–820. [CrossRef]
11. He, W.; Williard, N.; Osterman, M.; Pecht, M. Prognostics of lithium-ion batteries based on Dempster-Shafer theory and the Bayesian Monte Carlo method. *J. Power Sources* **2011**, *196*, 10314–10321. [CrossRef]
12. Liu, D.; Xie, W.; Liao, H.; Peng, Y. An Integrated Probabilistic Approach to Lithium-Ion Battery Remaining Useful Life Estimation. *IEEE Trans. Instrum. Meas.* **2015**, *64*, 660–670. [CrossRef]
13. Zhou, Y.; Huang, M. Lithium-ion batteries remaining useful life prediction based on a mixture of empirical mode decomposition and ARIMA model. *Microelectron. Reliab.* **2016**, *65*, 265–273. [CrossRef]
14. He, W.; Li, Z.; Liu, T.; Liu, Z.; Guo, X.; Du, J.; Li, X.; Sun, P.; Ming, W. Research progress and application of deep learning in remaining useful life, state of health and battery thermal management of lithium batteries. *J. Energy Storage* **2023**, *70*, 107868. [CrossRef]
15. Lyu, C.; Lai, Q.; Ge, T.; Yu, H.; Wang, L.; Ma, N. A lead-acid battery's remaining useful life prediction by using electrochemical model in the Particle Filtering framework. *Energy* **2017**, *120*, 975–984. [CrossRef]
16. Ren, Y.; Tang, T.; Xia, Q.; Zhang, K.; Tian, J.; Hu, D.; Yang, D.; Sun, B.; Feng, Q.; Qian, C. A data and physical model joint driven method for lithium-ion battery remaining useful life prediction under complex dynamic conditions. *J. Energy Storage* **2024**, *79*, 110065. [CrossRef]
17. Khaleghi, S.; Hosen, M.S.; Van Mierlo, J.; Berecibar, M. Towards machine-learning driven prognostics and health management of Li-ion batteries. A comprehensive review. *Renew. Sustain. Energy Rev.* **2024**, *192*, 114224. [CrossRef]
18. Alsuwian, T.; Ansari, S.; Zainuri, M.A.A.M.; Ayob, A.; Hussain, A.; Lipu, M.H.; Alhawari, A.R.; Almawgani, A.; Almasabi, S.; Hindi, A.T. A review of expert hybrid and co-estimation techniques for SOH and RUL estimation in battery management system with electric vehicle application. *Expert Syst. Appl.* **2024**, *246*, 123123. [CrossRef]
19. Huang, Y.; Zhang, P.; Lu, J.; Xiong, R.; Cai, Z. A transferable long-term lithium-ion battery aging trajectory prediction model considering internal resistance and capacity regeneration phenomenon. *Appl. Energy* **2024**, *360*, 122825. [CrossRef]
20. Zhao, H.; Meng, J.; Peng, Q. Early perception of Lithium-ion battery degradation trajectory with graphical features and deep learning. *Appl. Energy* **2025**, *381*, 125214. [CrossRef]
21. Yang, Y.; Yang, J.; Wu, X.; Fu, L.; Gao, X.; Xie, X.; Ouyang, Q. Battery pack capacity prediction using deep learning and data compression technique: A method for real-world vehicles. *J. Energy Chem.* **2025**, *106*, 553–564. [CrossRef]
22. Du, J.; Zhang, C.; Li, S.; Zhang, L.; Zhang, W. Two-stage prediction method for capacity aging trajectories of lithium-ion batteries based on Siamese-convolutional neural network. *Energy* **2024**, *295*, 130947. [CrossRef]
23. Zafar, M.H.; Mansoor, M.; Houran, M.A.; Khan, N.M.; Khan, K.; Moosavi, S.K.R.; Sanfilippo, F. Hybrid deep learning model for efficient state of charge estimation of Li-ion batteries in electric vehicles. *Energy* **2023**, *282*, 128317. [CrossRef]
24. Xiang, Y.; Fan, W.; Zhu, J.; Wei, X.; Dai, H. Semi-supervised deep learning for lithium-ion battery state-of-health estimation using dynamic discharge profiles. *Cell Rep. Phys. Sci.* **2024**, *5*, 101763. [CrossRef]
25. Fan, Y.; Xiao, F.; Li, C.; Yang, G.; Tang, X. A novel deep learning framework for state of health estimation of lithium-ion battery. *J. Energy Storage* **2020**, *32*, 101741. [CrossRef]
26. Bole, B.; Kulkarni, C.S.; Daigle, M. Adaptation of an electrochemistry-based Li-ion battery model to account for deterioration observed under randomized use. In *PHM 2014—Proceedings of the Annual Conference of the Prognostics and Health Management Society 2014*; Prognostics and Health Management Society: New York, NY, USA, 2014; pp. 502–510.
27. Lu, J.; Xiong, R.; Tian, J.; Wang, C.; Hsu, C.-W.; Tsou, N.-T.; Sun, F.; Li, J. Battery degradation prediction against uncertain future conditions with recurrent neural network enabled deep learning. *Energy Storage Mater.* **2022**, *50*, 139–151. [CrossRef]
28. Lu, J.; Xiong, R.; Tian, J.; Wang, C.; Sun, F. Deep learning to predict battery voltage behavior after uncertain cycling-induced degradation. *J. Power Sources* **2023**, *581*, 233473. [CrossRef]
29. Lu, J.; Xiong, R.; Tian, J.; Wang, C.; Sun, F. Deep learning to estimate lithium-ion battery state of health without additional degradation experiments. *Nat. Commun.* **2023**, *14*, 2760. [CrossRef]
30. Lombardo, T.; Duquesnoy, M.; El-Bouysidy, H.; Årén, F.; Gallo-Bueno, A.; Jørgensen, P.B.; Bhowmik, A.; Demortière, A.; Ayerbe, E.; Alcaide, F.; et al. Artificial Intelligence Applied to Battery Research: Hype or Reality? *Chem. Rev.* **2022**, *122*, 10899–10969. [CrossRef]
31. Nobre, J.; Neves, R.F. Combining Principal Component Analysis, Discrete Wavelet Transform and XGBoost to trade in the financial markets. *Expert Syst. Appl.* **2019**, *125*, 181–194. [CrossRef]
32. Deringer, V.L.; Bartók, A.P.; Bernstein, N.; Wilkins, D.M.; Ceriotti, M.; Csányi, G. Gaussian Process Regression for Materials and Molecules. *Chem. Rev.* **2021**, *121*, 10073–10141. [CrossRef] [PubMed]
33. Valverde, J.M.; Tohka, J. Region-wise loss for biomedical image segmentation. *Pattern Recognit.* **2023**, *136*, 109208. [CrossRef]

34. Van Erven, T.; Harrëmos, P. Rényi divergence and kullback-leibler divergence. *IEEE Trans. Inf. Theory* **2014**, *60*, 3797–3820. [CrossRef]
35. Gal, Y.; Ghahramani, Z. Dropout as a Bayesian approximation. *arXiv* **2015**, arXiv:1506.02157. [CrossRef]

3.3.3 Decoupling Analysis of Parameter Inconsistencies in Lithium-Ion Battery Packs Guiding Balancing System Design（B 类）

energies

MDPI

Article

Decoupling Analysis of Parameter Inconsistencies in Lithium-Ion Battery Packs Guiding Balancing System Design

Yanzhou Duan [1], Wenbin Ye [1], Qiang Zhang [2], Jixu Wang [1] and Jiahuan Lu [3,*]

[1] China Academy of Space Technology Hangzhou Institute, Hangzhou 310024, China; duanyanzhou_leon@163.com (Y.D.); yewenbin@casthz.cn (W.Y.); jxwang503@126.com (J.W.)
[2] China Academy of Space Technology, Beijing 100094, China; zhang007qiang@163.com
[3] College of Engineering, South China Agricultural University, Guangzhou 510642, China
* Correspondence: jhlu@scau.edu.cn

Abstract

Inconsistencies in lithium-ion battery packs pose significant challenges for both electric vehicles and energy storage systems, causing diminished energy utilization and accelerated battery aging. This study investigates the characteristics and aging processes of 32 batteries, creating simulation models for cells and packs based on experimental data. Through a controlled single-variable approach, the decoupled analysis of multi-parameter inconsistencies is carried out. Simulation results demonstrate that parallel-connected packs can maintain charge consistency without the need for external balancing systems, thanks to their self-balancing mechanisms. On the other hand, series-connected packs experience accelerated capacity degradation primarily due to charge inconsistencies linked to differences in Coulombic efficiency (CE) and the initial state of charge (SOC). For packs with minor capacity variations and temperature inconsistencies, a passive balancing current of 0.001 C can effectively eliminate up to 3.8% of capacity loss caused by charge inconsistencies within 15 cycles. Active balancing systems outperform passive ones primarily when there is significant capacity inconsistency. However, for packs that have undergone capacity screening before assembly, both active and passive balancing systems prove to be equally effective. Additionally, inconsistencies in internal resistance have a minimal impact on overall pack capacity but limit the power of both series-connected and parallel-connected packs. These findings offer essential insights for the development of balancing systems within battery management systems.

Keywords: lithium-ion battery; battery pack; inconsistency; passive balancing; active balancing; battery management system

Academic Editor: King Jet Tseng

Received: 30 May 2025
Revised: 24 June 2025
Accepted: 26 June 2025
Published: 30 June 2025

Citation: Duan, Y.; Ye, W.; Zhang, Q.; Wang, J.; Lu, J. Decoupling Analysis of Parameter Inconsistencies in Lithium-Ion Battery Packs Guiding Balancing System Design. *Energies* **2025**, *18*, 3439. https://doi.org/10.3390/en18133439

1. Introduction

As one of the key components driving the development of new energy technologies, lithium-ion batteries have been widely adopted in energy storage systems and new energy vehicles due to their advantages of high energy density and long cycle life [1]. Cells are typically connected in series-parallel configurations to satisfy power and capacity demands. However, inconsistencies in cell parameters can lead to the 'barrel effect', significantly compromising the operational safety and lifespan of the battery pack [2]. Consequently, research on battery consistency management holds critical importance for advancing the efficient utilization of large-scale battery systems.

Battery inconsistency refers to the differences in parameters such as voltage, state of charge (SOC), capacity, and internal resistance among cells of the same specification [3]. As

shown in Figure 1, the differences in external characteristics of batteries arise from the coupled effects of multiple internal and external factors [4]. Externally, critical factors affecting consistency include the resistance of tab welds and connectors [5], thermal management conditions [6], and preload forces exerted on cell surfaces [7]. Internally, variations in the initial state and aging processes of cells lead to inconsistencies in internal parameters like SOC, capacity, and internal resistance [8]. The initial state differences primarily depend on battery materials and manufacturing process quality during steps such as electrode coating and formation [9]. The differences in the aging process are primarily attributed to factors such as Coulombic efficiency (CE), capacity fade rate, and resistance growth rate. These depend not only on the materials and manufacturing techniques but also on the structural design and management strategies of the battery pack [10]. Inconsistent CE induces SOC variations in the short term [11], which indirectly causes uneven depth of discharge (DOD) and further aggravates inconsistent capacity fade rates [12]. Additionally, inconsistent internal resistance causes temperature differences during operation, further affecting CE and capacity fade rate [13].

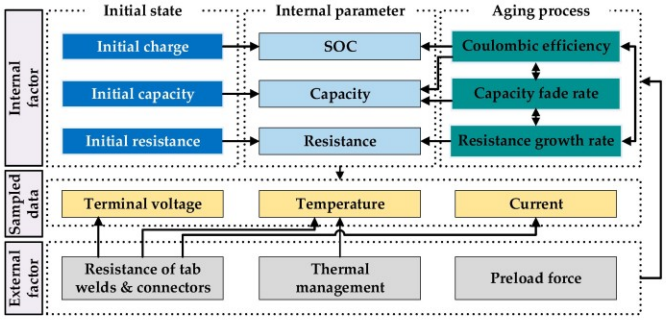

Figure 1. Influencing factors of inconsistency and their relationships.

As demonstrated above, inconsistency evolution is a complex process involving the interaction of multiple factors. Without effective management, it can lead to accelerated capacity fade and significant reduction in service life [14]. Therefore, first, cells must undergo screening prior to pack assembly to enhance initial consistency [15,16]. Second, external inconsistencies should be mitigated through optimized mechanical structures and thermal management systems [17,18]. However, inconsistencies arising from battery aging remain unavoidable. To address this, balancing systems are required to improve the performance of the battery pack after aging.

Common balancing systems are classified into two categories: active and passive balancing systems [19,20]. Active balancing systems transfer energy from high-energy cells to low-energy ones via external circuits [21] or individually charge low-energy cells using external power sources [22]. There is almost no energy loss in this process. Conversely, passive balancing systems dissipate excess energy from high-energy cells through parallel resistors as heat until energy equalization is achieved [23]. This reduces the total system energy, making it also known as dissipative balancing.

Current research suggests that passive balancing is suitable for small-to-medium-sized battery packs with good consistency, offering simple structure and ease of operation. In contrast, complicated active balancing is preferred for high-power application scenarios such as large-scale packs with significant inconsistency [24]. However, detailed studies remain scarce regarding the specific applicability of active and passive balancing under varying battery parameter inconsistencies. Systematic investigation into the impact of cell

parameter inconsistencies on pack performance and the applicability of active and passive balancing is critical for enhancing the efficient and safe utilization of energy. Nevertheless, conducting such research using actual battery packs faces significant challenges due to the following factors:

1. Parameter coupling: The influence of cell parameter inconsistencies on overall pack performance exhibits strong interdependencies [25].
2. Measurement constraints: Key parameters of cells such as capacity, SOC, and CE cannot be directly measured during aging tests without disassembling the pack.
3. Irreversibility and non-reproducibility: Irreversible parameter changes and non-repeatable experimental conditions prevent result verification.

To address these limitations, this paper establishes battery models based on experimental data, with investigations conducted through simulation. The major contributions of this paper are as follows:

1. A controlled single-variable approach is innovatively introduced to inconsistency evolution analysis. Based on the developed battery pack simulation model, this study quantitatively decouples how each factor (e.g., initial capacity, internal resistance, CE) independently drives pack capacity degradation. This solves the problem of unclear fade mechanisms of pack capacity under multi-parameter coupling in traditional experimental science and offers crucial evidence for identifying the main factors of pack capacity fade.
2. Previous studies select active/passive balancing systems based solely on cost and balancing time. The correlation between inconsistency types (SOC/capacity/resistance) and optimal balancing system is systematically proposed for the first time based on decoupling analysis. These findings provide new guidance and a novel dimension for selecting balancing systems.

The remaining sections are organized as follows: Section 2 describes the lithium-ion batteries and experimental protocols employed in this paper. Section 3 presents the methodology for constructing the battery simulation model. Section 4 systematically conducts a decoupling analysis of parameter inconsistencies of battery packs configured in series and parallel. Section 5 discusses the applicability of active and passive balancing. Finally, Section 6 summarizes the findings.

2. Battery Experiment

To comprehensively characterize the probability distribution of battery parameters and mitigate the effects of random experimental errors, 32 lithium nickel manganese cobalt oxide (NMC) batteries of the same batch are selected as test subjects. These cells, sequentially labeled NMC01 to NMC32, exhibit specifications detailed in Table 1.

Table 1. Specifications of NMC batteries.

Parameter	Value
Size	Ø18 × 65 mm
Normal capacity	2.4 Ah
Cut-off voltages	3.0–4.2 V
Max discharge rate	4 C (0~40 °C)
Normal charge rate	0.5 C at 25 °C
Operating temperature	−20–60 °C for discharge and 10–45 °C for charge
Mass	48 g

The experimental platform consists of an ARBIN-BT2000, an environmental simulation chamber, and a host computer. As shown in Figure 2, the experimental procedure mainly

consists of four parts: capacity tests, open-circuit voltage (OCV) tests, hybrid power pulse characteristic (HPPC) tests, and aging cycle tests. Characteristic tests are performed every 100 aging cycles. All tests are conducted at 25 °C.

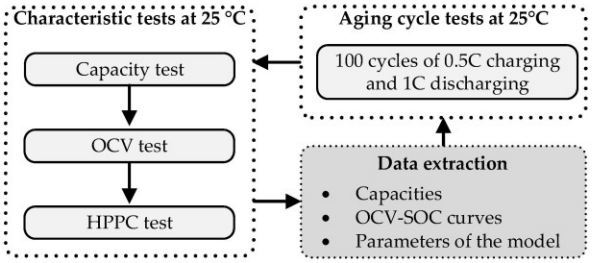

Figure 2. Experimental procedure.

3. Construction of Simulation Model

Battery management algorithms often employ equivalent circuit models, electrochemical models, or neural network models to characterize both long-term and short-term battery behaviors [26,27]. However, the evolution of inconsistencies involves multi-factor coupling effects, and precise modeling of all cells can lead to excessive computational demands. Given that this paper primarily focuses on long-term battery parameter evolution (e.g., capacity and internal resistance), short-term battery behaviors such as concentration polarization are omitted in the modeling framework. Consequently, the simulation model developed in this section incorporates certain simplifications.

3.1. Battery Cell Model

3.1.1. Equivalent Circuit Model

The Rint model is selected in this paper. The model structure is shown in Figure 3. Here, U_t denotes the terminal voltage of the battery, I_L represents the load current (positive during discharge and negative during charge), R_i is the internal resistance, and U_{OCV} is the open-circuit voltage. While R_i and U_{OCV} vary with temperature, changes caused by temperature fluctuations under constant ambient conditions are neglected in this section. Therefore, R_i and U_{OCV} are only related to the aging state and SOC.

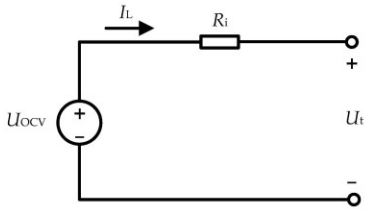

Figure 3. Rint model.

The SOC can be determined using the following equation:

$$z_k = \frac{Q_k}{C_{a,k}} \times 100\%, \tag{1}$$

$$Q_k = Q_0 - \int \eta(I_L + I_B)dt, \tag{2}$$

where z_k denotes the SOC at time k, Q_k represents the remaining charge at time k, $C_{a,k}$ is the capacity, Q_0 indicates the initial charge, I_B denotes the balancing current, and η is the CE. CE is challenging to obtain experimentally. The discharge CE is generally assumed to be approximately 1, while the charge CE is modeled using Equation (3) in this study to characterize its temperature-dependent behavior.

$$\begin{cases} \eta_{dch} = 1 \\ \eta_{chg} = 1 + k_\eta \cdot (T - 298) \end{cases}, \quad (3)$$

where η_{dch} and η_{chg} denote the discharge and charge CE, respectively. T denotes the Kelvin temperature. k_η is the temperature negative correlation coefficient, which is set to -2×10^{-5} in this paper. This implies that the charge CE generally decreases with rising temperature [28].

3.1.2. Thermal Model

The thermal model used in this paper is shown in Equation (4):

$$T = T_0 + \int \left[(I_L + I_B)^2 R_i - q(T - T0)A \right] / (m \cdot C_m) dt, \quad (4)$$

where m is the cell mass, and T_0 is the ambient temperature in Kelvin. C_m indicates the specific heat capacity, taken as 1000 J/(kg·K). A represents the heat dissipation area and is set to 0.0042 m^2. q denotes the heat dissipation coefficient. Optimized thermal management ensures approximate uniformity in heat dissipation across cells. Thus, q is assumed constant at 20 W/(K·m^2) here.

3.1.3. Aging Model

The aging model in this paper is established based on experimental data. As shown in Figure 4a, the cells exhibit good initial consistency in internal resistance, with a mean value of 34.78 mΩ and a standard deviation of 1.53 mΩ.

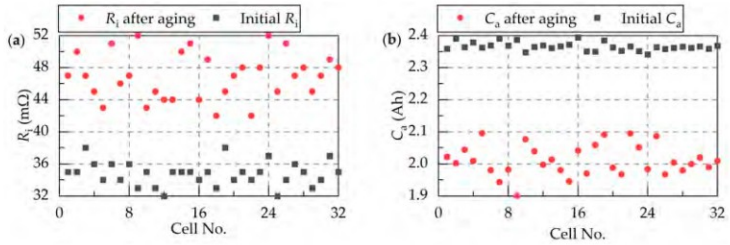

Figure 4. Distributions of internal resistance and capacity across 32 cells. (**a**) Initial internal resistance and internal resistance after aging. (**b**) Initial capacity and capacity after aging.

After 400 aging cycles, the internal resistances increase overall. The inconsistency further aggravates, with the mean value rising to 47.04 mΩ and the standard deviation increasing to 3.08 mΩ. In addition, due to divergent aging trajectories, the cells with the maximum and minimum internal resistance shift after the aging cycles compared to before. Similarly, the capacity distribution is shown in Figure 4b. The initial capacity demonstrates a mean value of 2.36 Ah with a standard deviation of 0.014 Ah. After 400 aging cycles, the capacity exhibits a reduced mean value of 2.01 Ah and an increased standard deviation of 0.05 Ah. It indicates an overall capacity fade and increased inconsistency.

Figure 5 illustrates the internal resistance growth trajectories and capacity fade trajectories of 32 cells over 400 aging cycles.

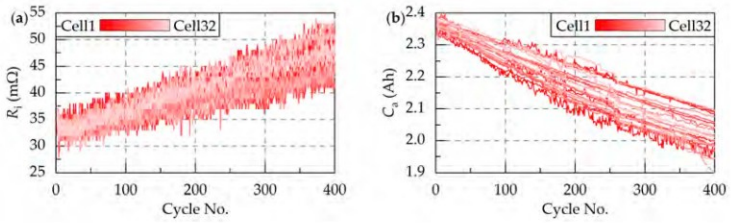

Figure 5. Internal resistance growth trajectories and capacity fade trajectories of 32 cells over 400 aging cycles. (**a**) Internal resistance growth trajectories. (**b**) Capacity fade trajectories.

Based on the experimental data, simplified linear aging models for battery resistance and capacity are established, as shown in Equations (5) and (6), respectively.

$$R_{i,N} = R_{i,0} + k_R \cdot N, \tag{5}$$

$$C_{a,N} = C_{a,0} + k_C \cdot N, \tag{6}$$

where $N \in [0, 400]$ denotes the equivalent cycle number, defined as the ratio of total charge/discharge ampere-hour (Ah) to the rated capacity. $R_{i,N}$ and $C_{a,N}$ represent the internal resistance and capacity at equivalent cycle N. $R_{i,0}$ and $C_{a,0}$ indicate the initial internal resistance and initial capacity, respectively. k_R is the positive internal resistance growth rate, and k_C is the negative capacity fade rate.

3.2. Battery Pack Model

The battery pack model comprises basic models and difference models. The basic models establish relationships between cell-level and pack-level parameters, defining pack capacity, SOC, resistance, and other pack-level parameters under varying topologies and balancing system configurations. Difference models generate parameter variations among cells to simulate inconsistencies. The overall flowchart for constructing the battery pack model is illustrated in Figure 6.

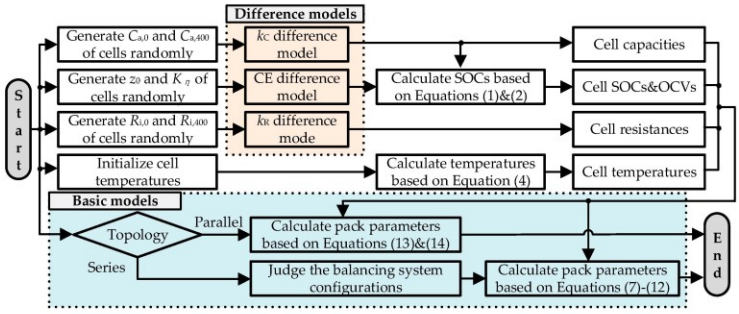

Figure 6. Overall flowchart for constructing the battery pack model.

3.2.1. Basic Model

The calculation methods for parameters such as capacity, internal resistance, and SOC in the battery pack differ from those for the cell. For series-connected battery packs, the

total current equals the main circuit current, and the total voltage and internal resistance correspond to the sum of terminal voltages and internal resistances of all series-connected cells, respectively. However, the definitions of usable capacity and SOC vary with the applied balancing systems [29]. As shown in Figure 7, we take three series-connected cells as an example:

1. Battery packs without balancing systems. Cell 1 exhibits the minimum remaining rechargeable capacity in the initial state, while Cell 2 demonstrates the minimum remaining electric quantity and the smallest total capacity. During charging, Cell 1 gets fully charged first, whereas Cell 2 gets fully discharged first during discharging. This demonstrates that the total pack capacity is constrained by the two cells, and the battery pack state is defined accordingly as follows [30]:

$$C_{\mathrm{a,pack}}^{\mathrm{no}} = \min(C_{\mathrm{a},i} \cdot z_i) + \min\left[C_{\mathrm{a},j} \cdot (1 - z_j)\right], \tag{7}$$

$$z_{\mathrm{pack}}^{\mathrm{no}} = \frac{\min(C_{\mathrm{a},i} \cdot z_i)}{C_{\mathrm{a,pack}}^{\mathrm{no}}} \times 100\%, \tag{8}$$

   where $C_{\mathrm{a,pack}}^{\mathrm{no}}$ and $z_{\mathrm{pack}}^{\mathrm{no}}$ denote the capacity and SOC of the battery pack without the balancing system, and C_{a} and z indicate the capacity and SOC of cells.
2. Battery packs with passive balancing systems. Dissipative resistors continuously discharge Cells 1 and 3 during charging to ensure Cell 2 achieves full charge. Passive balancing is disabled during discharging, allowing Cell 2 (with the minimum remaining electric quantity) to get fully discharged first. Consequently, the theoretical maximum capacity of the battery pack with the passive balancing system equals the capacity of the weakest cell. The battery pack state is defined as follows:

$$C_{\mathrm{a,pack}}^{\mathrm{pa}} = \min(C_{\mathrm{a},i}), \tag{9}$$

$$z_{\mathrm{pack}}^{\mathrm{pa}} = \frac{\min(C_{\mathrm{a},i} \cdot z_i)}{C_{\mathrm{a,pack}}^{\mathrm{pa}}} \times 100\%, \tag{10}$$

   where $C_{\mathrm{a,pack}}^{\mathrm{pa}}$ and $z_{\mathrm{pack}}^{\mathrm{pa}}$ denote the capacity and SOC of the battery pack with the passive balancing system.
3. Battery packs with active balancing systems. Since energy can be transferred among cells, it can theoretically ensure that all cells reach full charge or full discharge simultaneously. The state is defined as follows for the battery pack:

$$C_{\mathrm{a,pack}}^{\mathrm{ac}} = \mathrm{mean}(C_{\mathrm{a},i}), \tag{11}$$

$$z_{\mathrm{pack}}^{\mathrm{ac}} = \frac{\mathrm{mean}(C_{\mathrm{a},i} \cdot z_i)}{C_{\mathrm{a,pack}}^{\mathrm{ac}}} \times 100\%, \tag{12}$$

   where $C_{\mathrm{a,pack}}^{\mathrm{ac}}$ and $z_{\mathrm{pack}}^{\mathrm{ac}}$ denote the capacity and SOC of the battery pack with the active balancing system.

Compared to series-connected battery packs, the basic model of parallel-connected battery packs is relatively simpler. All cells share identical terminal voltages, while the total pack capacity equals the sum of cell capacities. The pack resistance can be calculated using Equation (13):

$$R_{\mathrm{pack}} = \frac{R_1 R_2 \ldots R_n}{R_1 + R_2 + \ldots + R_n}, \tag{13}$$

where R_{pack} denotes the pack resistance, and R_n represents the internal resistance of each cell. Due to the self-balancing mechanism, the OCVs of all cells equalize after prolonged

rest periods [31]. During operation, differences in internal resistance cause varying branch currents. These currents can be calculated according to Equation (14):

$$\begin{bmatrix} 1 & R_1 & 0 & 0 & 0 \\ 1 & 0 & R_2 & \ddots & 0 \\ \vdots & \vdots & 0 & \ddots & 0 \\ 1 & 0 & \dots & 0 & R_n \\ 0 & 1 & 1 & \dots & 1 \end{bmatrix} \begin{bmatrix} U_t \\ I_1 \\ I_2 \\ \vdots \\ I_n \end{bmatrix} = \begin{bmatrix} U_{OCV,1} \\ U_{OCV,2} \\ \vdots \\ U_{OCV,n} \\ I_L \end{bmatrix}, \tag{14}$$

where $U_{OCV,n}$ represents the OCV of the n-th cell, and I_n is the current in each branch.

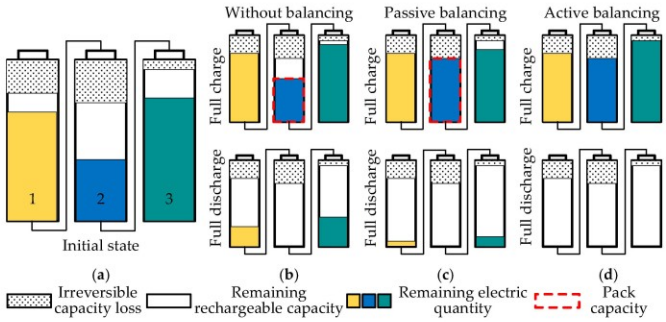

Figure 7. State differences in battery packs with different balancing systems. (**a**) Initial state of the battery packs. (**b**) Battery packs without balancing systems. (**c**) Battery packs with passive balancing systems. (**d**) Battery packs with active balancing systems.

3.2.2. Difference Model

To characterize inconsistency, models for differences in CE, internal resistance, and capacity are added. This section introduces an efficiency variation coefficient K_η to represent the inconsistency in CE among cells, as formulated below:

$$\begin{cases} \eta_{dch,i} = K_{\eta,i} \\ \eta_{chg,i} = K_{\eta,i}\left[1 + k_\eta \cdot (T_i - 298)\right] \end{cases} \tag{15}$$

where the values of K_η are selected based on experimental data, following a normal distribution with a mean of 0.9884 and a standard deviation of 5×10^{-5}.

The difference models for cell capacity and internal resistance are also generated based on experimental data. The initial internal resistances of cells follow a normal distribution with a mean of 34.78 mΩ and a standard deviation of 1.53 mΩ. After 400 aging cycles, the internal resistances conform to another normal distribution with a mean of 47.04 mΩ and a standard deviation of 3.13 mΩ. Initial and post-aging internal resistances for simulated cells are randomly generated using normal distribution functions. The slope of the line connecting the initial point and the aged point represents k_R in Equation (5). Then the internal resistance difference models for each simulated cell can be generated accordingly. The capacity difference models are constructed following a similar methodology.

4. Decoupling Analysis of Inconsistencies

This section employs a controlled single-variable approach to conduct battery pack simulation experiments. The battery parameters are configured according to experimental data, as specified in Table 2.

Table 2. Battery simulation parameter configuration.

Parameters	z_0	$C_{a,0}$	$R_{i,0}$	K_η	$C_{a,400}$	$R_{i,400}$
Expectation	0.5	2.363 Ah	34.78 mΩ	0.9884	2.026 Ah	47.04 mΩ
Standard deviation	0.01	0.03 Ah	1.53 mΩ	5×10^{-5}	0.06 Ah	3.13 mΩ

4.1. Simulation of Battery Pack Connected in Parallel

In parallel-connected battery packs, where all cells maintain identical terminal voltages, self-balancing during prolonged rest periods ensures equal initial SOC. Consequently, the primary factors influencing inconsistency include initial capacity, initial internal resistance, CE, capacity fade rate, and internal resistance growth rate. The simulation focuses on a 12p1s battery pack, and operational conditions are the same as those of aging cycle experiments to maintain degradation trajectory consistency. To reduce simulation time, rest periods between consecutive cycles are omitted.

4.1.1. Inconsistent Initial Capacity

The initial capacities of cells, generated stochastically based on Table 2, are listed in Table 3. The capacity fade rate is set to -7.8×10^{-4} Ah, and the other parameters are all taken as expected values.

Table 3. Initial capacities of cells.

No.	1	2	3	4	5	6	7	8	9	10	11	12
$C_{a,0}$ **(Ah)**	2.34	2.33	2.33	2.35	2.30	2.39	2.38	2.36	2.36	2.34	2.39	2.36

Figure 8a reveals fluctuating branch currents during charging. At the transition from discharge to charge, cells with smaller initial capacities exhibit higher branch currents. After approximately 70 s, branch currents turn to uniform levels. Subsequent current fluctuations show that higher-capacity cells sustain larger branch currents, while lower-capacity cells maintain higher SOC. This phenomenon originates from self-balancing mechanisms driven by capacity inconsistencies. When branch currents equalize, all cells have identical ohmic voltage drops and charge throughput. However, higher-capacity cells show smaller SOC increments and correspondingly smaller SOC increments. To preserve terminal voltage uniformity, branch currents of higher-capacity cells will increase to reduce SOC differences between cells, and ohmic voltage drops will also increase accordingly. As SOC differences decrease progressively, current inconsistencies diminish correspondingly, thus establishing a dynamic equilibrium. Figure 8b,c demonstrate that upon entering the OCV plateau, the differences in both branch currents and OCV are minimized. Charge throughput difference is defined as the difference between the charge/discharge throughput of each branch and the average throughput. As shown in Figure 8d, except during initial cycle transitions, lower-capacity cells consistently have less charge throughput. The curves exhibit fishtail-like expansion throughout the process. During the entire charging cycle, the maximum current difference reaches 0.06 C, the maximum variation of OCV is 5 mV, and the SOC difference remains below 1%.

Following the transition from charging to discharging cycles, the SOC of the cell with the minimum capacity becomes the lowest. Since the discharging rate is higher than the charging rate, Figure 9b,c demonstrate that with an initial capacity difference of 3.8%, the range of branch currents reaches 0.1 C, the range of OCVs attains 8.3 mV, and the range of SOCs exceeds 1%.

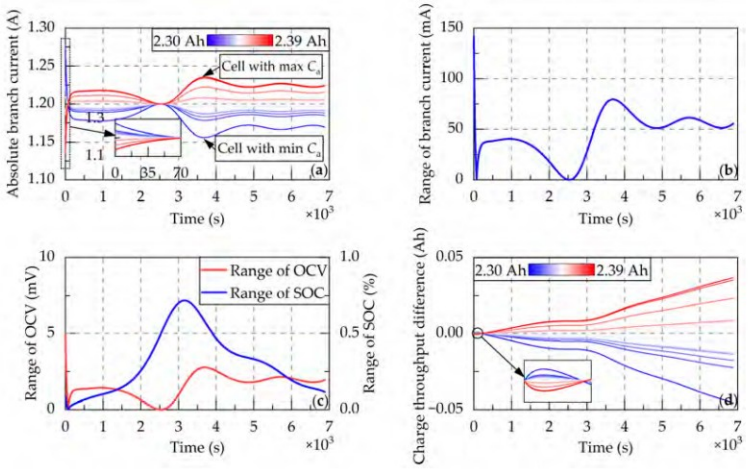

Figure 8. Simulation of the single charging cycle of battery packs with inconsistent initial capacities. (**a**) Absolute values of branch currents. (**b**) Range of branch currents. (**c**) Ranges of OCVs and SOCs. (**d**) Charge throughput differences in cells.

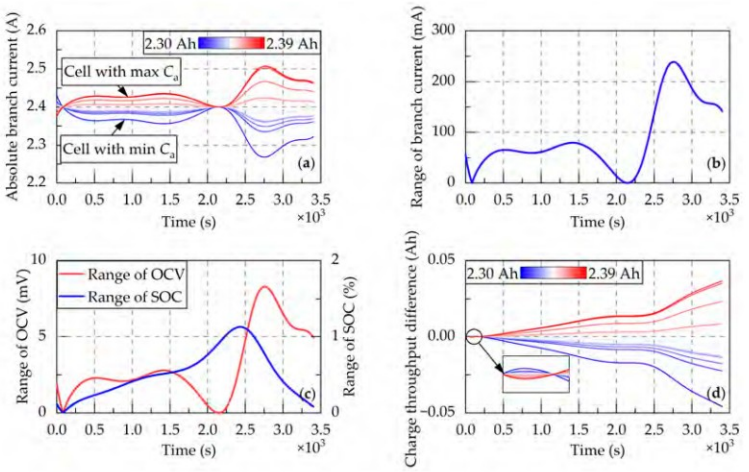

Figure 9. Simulation of the single discharging cycle of battery packs with inconsistent initial capacities. (**a**) Absolute values of branch currents. (**b**) Range of branch currents. (**c**) Ranges of OCVs and SOCs. (**d**) Charge throughput differences in cells.

4.1.2. Inconsistent Initial Internal Resistance

Initial internal resistances of cells, randomly generated based on Table 2, are listed in Table 4. The internal resistance growth rates are set to 0.03 mΩ.

Table 4. Initial internal resistances of cells.

No.	1	2	3	4	5	6	7	8	9	10	11	12
$R_{i,0}$ (mΩ)	35.5	36.4	35.9	34.3	35.2	33.6	36.1	33.0	33.1	33.5	30.3	37.0

Simulation results for a single discharging cycle are shown in Figure 10. The cell with the lowest initial internal resistance exhibits the smallest ohmic voltage drop and the lowest SOC. Upon entering the OCV plateau, discharge currents in lower-resistance branches increase to maintain terminal voltage uniformity, further amplifying the SOC differences. However, after exiting the OCV plateau, the discharge currents in lower-resistance branches rapidly decrease. Figure 10a,d illustrate the dynamic evolution of branch currents and charge throughput differences. Lower-resistance cells initially release more energy, while their discharge rates progressively decrease. The charge throughput difference curves first expand and then contract like a "spindle". Notably, despite identical cell capacities, lower-resistance cells deliver more energy during discharging cycles and absorb more charge during charging cycles, creating differences in C-rates and DOD. Figure 10b,c reveal that given the initial maximum internal resistance difference of 18.1%, the range of branch currents reaches 0.33 C, the range of OCVs attains 40 mV, and the range of SOCs exceeds 5%.

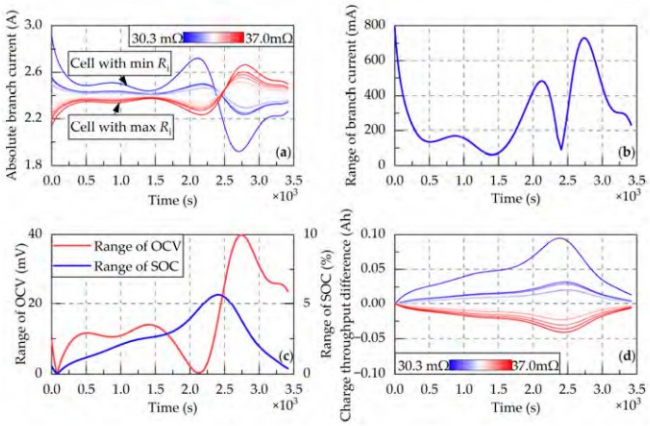

Figure 10. Simulation of the single discharging cycle of battery packs with inconsistent initial internal resistances. (**a**) Absolute values of branch currents. (**b**) Range of branch currents. (**c**) Ranges of OCVs and SOCs. (**d**) Charge throughput differences in cells.

4.1.3. Inconsistent Coulombic Efficiency

Given the small inconsistencies in actual CE, this section amplifies the standard deviation of the efficiency variation coefficient to enhance simulation clarity. The efficiency variation coefficients for cells are specified in Table 5, while other parameters are set to their expected values. CE inconsistencies impact the battery pack on a relatively small timescale. Within a single cycle, CE inconsistencies directly induce SOC differences among cells. As demonstrated in Figure 11 during charging, cells with lower CE have higher branch currents but lower SOC, similar to simulation results with inconsistent initial capacities. The maximum range of branch currents is about 0.02 C, the range of OCVs attains 1.4 mV, and the range of SOCs is less than 0.4%.

Table 5. Efficiency variation coefficients of cells.

No.	1	2	3	4	5	6	7	8	9	10	11	12
K_η (10^{-1})	9.83	9.89	9.91	9.94	9.96	9.89	9.81	9.85	9.83	10.00	9.85	9.92

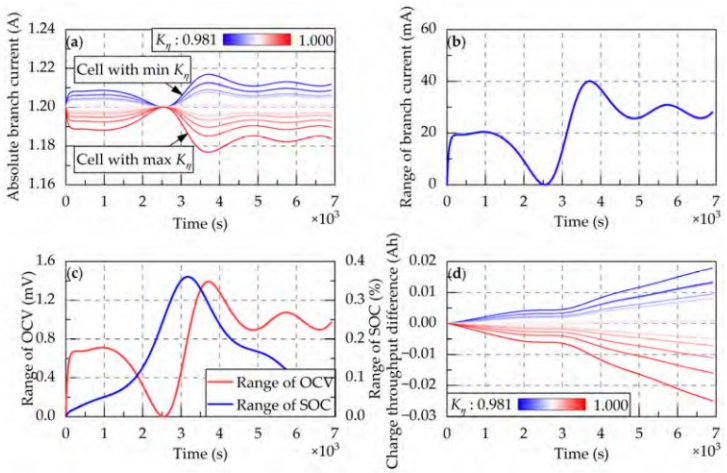

Figure 11. Simulation of the single charging cycle of battery packs with inconsistent CE. (**a**) Absolute values of branch currents. (**b**) Range of branch currents. (**c**) Ranges of OCVs and SOCs. (**d**) Charge throughput differences in cells.

As shown in Figure 12, inconsistencies show no significant progression even after 400 aging cycles. It indicates that parallel-connected battery packs are virtually unaffected by CE inconsistencies.

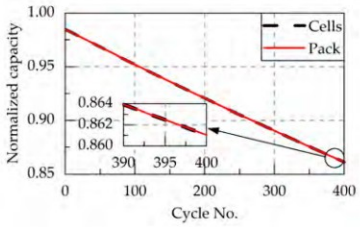

Figure 12. Aging trajectories of the parallel-connected battery pack and cells with inconsistent CE.

4.1.4. Inconsistent Capacity Fade Rate or Resistance Growth Rate

Inconsistent capacity fading rate and resistance growth rate affect the battery pack over a long-term timescale. Their effects resemble those caused by initial capacity and internal resistance inconsistencies. As cycles accumulate, the cumulative impacts of C-rate, DOD, equivalent cycle number, and temperature differences become stronger. This further exacerbates inconsistencies in capacity fade rates and resistance growth rates, ultimately accelerating capacity degradation in parallel-connected battery packs. In extreme cases, it can induce certain cells' actual charge/discharge rates to exceed the maximum limit, causing safety risks [32].

4.2. Simulation of Battery Pack Connected in Series

The simulation focuses on a 12s1p battery pack, and operational conditions are the same as those of aging cycle experiments.

4.2.1. Inconsistent Initial Capacity

The cell parameters align with those in Section 4.1.1. Figure 13a illustrates the fade trajectories of average cell capacity, minimum cell capacity, and pack capacity. The fade trajectory of pack capacity fully overlaps with that of the weakest cell, maintaining a constant offset from the average cell capacity. This demonstrates that the fade rates of series-connected packs are determined solely by the weakest cell, independent of initial capacity inconsistencies. While excessive initial capacity inconsistencies reduce the pack's lifetime average capacity, such effects remain stable and do not gradually expand with aging. Notably, the capacity gaps between the pack and the minimum/average cell capacities represent theoretically recoverable capacity losses through passive or active balancing systems, respectively. As shown in Figure 13b, passive balancing systems cannot restore capacity losses due to initial capacity inconsistencies, while active balancing systems can recover a fixed capacity equal to the difference between average and minimum cell capacities. For packs with an initial capacity range of 3.8%, active balancing systems can restore capacity by approximately 2%. Since cells are typically screened based on initial capacities before assembly, the impact of initial capacity inconsistency on series-connected packs can generally be eliminated.

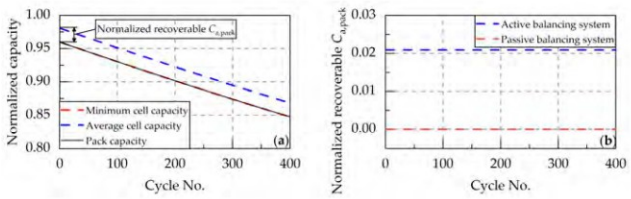

Figure 13. Simulation of series-connected packs with inconsistent initial capacities. (**a**) Fade trajectories of average cell capacity, minimum cell capacity, and pack capacity. (**b**) Theoretical recoverable capacity losses by active or passive systems.

4.2.2. Inconsistent Initial Internal Resistance

The parameters of cells align with those in Section 4.1.2. It should be noted that internal resistance inconsistencies lead to temperature variations, thereby causing differences in CE. However, during the simulation, the temperature difference induced by internal resistance does not exceed 1 °C, resulting in minimal SOC differences. As shown in Figure 14b, the capacity improvement through balancing is nearly zero, so the initial internal resistance inconsistency has almost no effect on the series-connected battery pack's capacity.

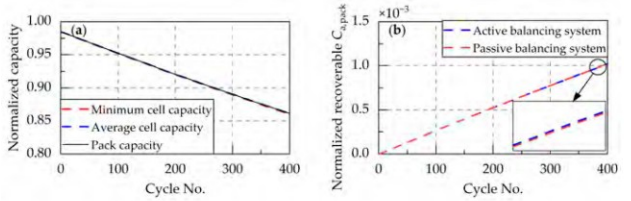

Figure 14. Simulation of series-connected packs with inconsistent initial internal resistances. (**a**) Fade trajectories of average cell capacity, minimum cell capacity, and pack capacity. (**b**) Theoretical recoverable capacity losses by active or passive systems.

4.2.3. Inconsistent Initial SOC

The initial SOCs of cells are generated according to Table 2, as detailed in Table 6. All other parameters are set to their expected values. Figure 15 reveals identical fade trajectories of the minimum cell capacity and average cell capacity, both maintaining a constant offset from the pack capacity fade trajectory. Notably, the recoverable capacity losses through active/passive balancing remain consistent, with normalized values closely matching the initial SOC range. This indicates that initial SOC inconsistencies have no persistent impact on battery packs, as such inconsistencies can be fully eliminated through balancing in the early stage.

Table 6. Initial SOCs of cells.

No.	1	2	3	4	5	6	7	8	9	10	11	12
SOC_0 (%)	50.5	51.8	47.7	50.9	50.3	48.7	49.6	50.3	53.6	52.8	48.7	53.0

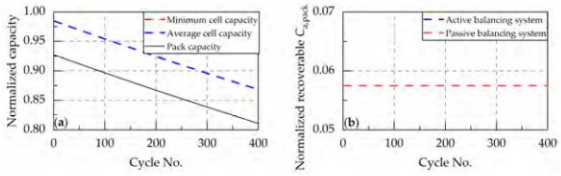

Figure 15. Simulation of series-connected packs with inconsistent initial SOCs. (**a**) Fade trajectories of average cell capacity, minimum cell capacity, and pack capacity. (**b**) Theoretical recoverable capacity losses by active or passive systems.

4.2.4. Inconsistent Coulombic Efficiency

The efficiency variation coefficients are randomly generated based on Table 2 as shown in Table 7, with other parameters set to their expected values.

Table 7. Efficiency variation coefficients of cells.

No.	1	2	3	4	5	6	7	8	9	10	11	12
K_η (10^{-1})	9.8834	9.8844	9.8841	9.8839	9.8840	9.8831	9.8839	9.8847	9.8839	9.8839	9.8835	9.8839

As shown in Figure 16, after 400 aging cycles, the minimum cell capacity retains 86.5% of the rated value, while the pack capacity declines to 81%. This is mainly due to the CE variations causing varying charge throughput across cells. Charge throughput differences accumulate progressively with aging, resulting in pack capacity losses illustrated in Figure 7b. Critically, CE inconsistencies induce negligible capacity variations, as evidenced by nearly identical minimum and average cell capacities in Figure 16a. Figure 16b further demonstrates that both active and passive balancing systems effectively reduce the battery pack capacity loss caused by CE inconsistencies.

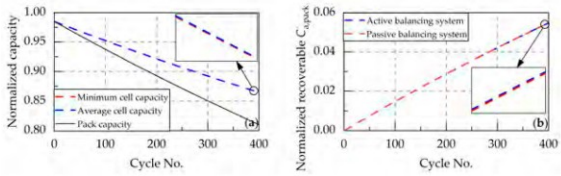

Figure 16. Simulation of series-connected packs with inconsistent CE. (**a**) Fade trajectories of average cell capacity, minimum cell capacity, and pack capacity. (**b**) Theoretical recoverable capacity losses by active or passive systems.

4.2.5. Inconsistent Capacity Fade Rate

The capacity fade rates of cells are set as specified in Table 8, with other parameters assigned their expected values.

Table 8. Capacity fade rates of cells.

No.	1	2	3	4	5	6	7	8	9	10	11	12
k_C $(-10^{-4}$ **Ah)**	8.47	8.53	8.07	7.02	6.20	8.02	8.40	7.85	8.35	10.0	6.87	7.87

Figure 17 demonstrates that the battery pack capacity always equals the minimum cell capacity, while the difference between pack capacity and average cell capacity gradually increases. This pack capacity loss can only be recovered by active balancing systems.

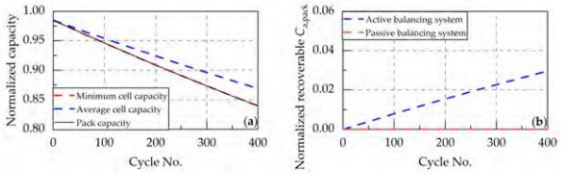

Figure 17. Simulation of series-connected packs with inconsistent capacity fade rates. (**a**) Fade trajectories of average cell capacity, minimum cell capacity, and pack capacity. (**b**) Theoretical recoverable capacity losses by active or passive systems.

4.2.6. Inconsistent Resistance Growth Rate

The resistance growth rates of cells are set as specified in Table 9, with other parameters assigned their expected values.

Table 9. Resistance growth rates of cells.

No.	1	2	3	4	5	6	7	8	9	10	11	12
k_R $(10^{-2}$ **mΩ)**	2.86	2.65	4.16	3.23	2.29	4.38	4.23	2.24	2.22	2.90	3.21	3.73

As shown in Figure 18a, even with a 50% range in resistance growth rates, the minimum cell capacity, average cell capacity, and pack capacity are roughly equal. Figure 18b reveals that increased internal resistance differences indirectly induce minor CE variations, though the recoverable capacity loss through balancing systems remains below 0.1%. These results conclusively demonstrate that inconsistencies in resistance growth rates have a negligible impact on battery pack capacity.

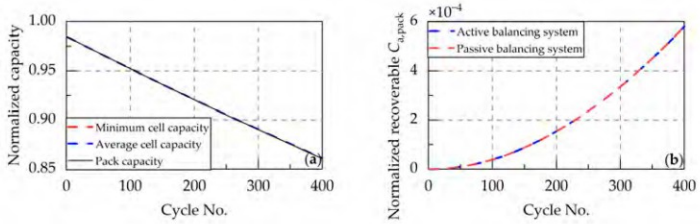

Figure 18. Simulation of series-connected packs with inconsistent resistance growth rates. (**a**) Fade trajectories of average cell capacity, minimum cell capacity, and pack capacity. (**b**) Theoretical recoverable capacity losses by active or passive systems.

5. Discussion

The preceding analysis demonstrates that the self-balancing mechanism in parallel-connected battery packs functionally equates to terminal voltage-based active balancing. Throughout the aging process, normal cell inconsistencies exhibit minimal impact on the capacity of parallel-connected battery packs, so no extra balancing system is needed. However, significant inconsistencies, particularly large differences in internal resistance, can cause individual cells to experience higher current rates than the pack average, accelerating cell aging or causing safety risks. Consequently, pre-assembly screening of capacity and resistance, especially resistance, is critical for parallel-connected packs.

For series-connected battery packs, supplemental balancing systems prove essential. The applicability of the active/passive balancing system is discussed below from three perspectives.

1. Capacity inconsistency. Capacity inconsistencies primarily arise from steady-state differences from initial capacity and dynamic differences caused by varying capacity fade rates. Although CE inconsistencies indirectly contribute to capacity inconsistencies, their impact remains negligible compared to the former factors. As mentioned earlier, passive balancing systems cannot address capacity inconsistencies. Only active balancing systems ensuring full charge and discharge of all cells can achieve theoretical maximum pack capacity, while persistent capacity inconsistencies impose heavy loads on active balancing circuits. For well-managed packs with pre-screened capacities, the costly and complex active balancing systems can be avoided.
2. Resistance inconsistency. Resistance inconsistencies originate from inconsistent initial resistances and resistance growth rates. Large resistance differences can induce thermal differences, indirectly affecting CE and capacity fade rates. However, in packs with optimized thermal management systems, such effects remain negligible. Simulations confirm that resistance inconsistencies do not greatly affect the capacity of series-connected battery packs. However, like parallel-connected packs, they can limit the available power and overall performance. Notably, series-connected packs demand stricter consistency in capacity and charge during pre-assembly screening, with resistance uniformity being comparatively less critical.
3. Charge inconsistency. Initial SOC and CE variations jointly determine charge inconsistency. Initial SOC-induced charge inconsistencies remain constant during cycling, while CE-induced charge differences accumulate with aging. Initial SOC variations can be eliminated early in the pack's life through balancing systems, so their impact is transient. In contrast, CE-induced charge differences are persistent, requiring continuous balancing throughout the pack's life. Simulation experiments show that charge inconsistencies are the main cause of pack capacity fading, while in the case of only inconsistent charge, there is almost no difference in the pack capacity loss that can be restored through passive or active balancing systems. To reduce balancing loads, pre-assembly screening should minimize initial SOC variations, coupled with manufacturing process improvements to reduce CE inconsistencies. Notably, the above simulation is for battery packs with uniform heat dissipation. Long-term aging may amplify thermal inconsistencies, which can further indirectly cause charge differences due to temperature-dependent CE. While balancing systems can address resultant pack capacity losses, an effective thermal management system remains essential throughout the battery's lifecycle, significantly reducing the operational burden on balancing circuits.

Given that passive balancing currents are typically limited, further discussion is required to assess their applicability in packs with large charge inconsistencies. In automotive battery packs, the standard deviation of initial SOC is generally below 0.005, while the

CE standard deviation is less than 3×10^{-5}. Considering extreme cases, this section sets initial SOC and CE standard deviations to 0.01 and 5×10^{-5}, respectively. Furthermore, the cell with the lower initial SOC also has the lower CE. Initial SOCs and efficiency variation coefficients are randomly generated and sorted in ascending order, as detailed in Table 10. Other parameters are set to expected values based on Table 2.

Table 10. Initial SOCs and efficiency variation coefficients of the simulated cells.

No.	1	2	3	4	5	6	7	8	9	10	11	12
SOC_0 (%)	47.9	48.0	48.9	49.2	49.8	50.1	50.5	50.7	51.0	51.4	51.4	51.7
K_η (10^{-1})	9.8831	9.8834	9.8835	9.8839	9.8839	9.8839	9.8839	9.8839	9.8840	9.8841	9.8844	9.8847

Figure 19a presents simulation results without passive balancing. It indicates that the capacity of the battery pack declines rapidly. After approximately 350 aging cycles, the capacity of the battery pack is less than 80% of the rated value. Initial SOC inconsistencies account for a 3.8% capacity loss, while CE differences lead to increasing charge inconsistencies, contributing an additional 9.1% recoverable capacity loss after 400 cycles.

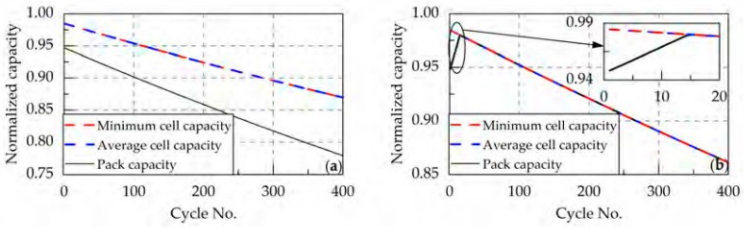

Figure 19. Simulation of series-connected battery packs with inconsistent initial SOC and CE. (**a**) Simulation results without passive balancing. (**b**) Simulation results with passive balancing.

For comparison, the simulation is repeated with passive balancing enabled. The passive balancing current is set to 0.001 C. This indicates that for automotive battery packs with capacities of 100–200 Ah, the balancing current does not exceed 200 mA, consistent with practical implementations [33]. As shown in Figure 19b, capacity losses caused by charge inconsistencies are fully eliminated within approximately 15 cycles. Then, the pack capacity remains equal to the theoretical maximum capacity. These findings confirm that even with severe charge inconsistencies, a 0.001 C passive balancing current remains fully sufficient.

In summary, passive balancing systems cannot recover pack capacity losses caused by capacity inconsistencies. Therefore, active balancing systems are superior for scenarios with significant differences in initial capacities or capacity fade rates, or where fast balancing is required, such as second-life applications or large-scale battery maintenance operations. However, for pre-screened packs exhibiting minimal capacity inconsistencies, passive balancing systems achieve equivalent recoverable pack capacity as active balancing systems. Crucially, the passive balancing remains effective even when initial SOC and CE standard deviations reach 0.01 and 5×10^{-5}, respectively. Given their simple structure and low cost, passive balancing systems are the optimal solution in such scenarios.

6. Conclusions

This study investigates battery pack inconsistencies under multi-parameter coupling conditions. Characterization and aging experiments are conducted on 32 NMC batteries at 25 °C to extract cell parameters and degradation trajectories. The data from these

experiments are used to develop simulation models for both cells and packs. A controlled single-variable approach is used to conduct the decoupled analysis of the impacts of multi-parameter inconsistencies on battery packs. The capacity degradations of series-connected and parallel-connected battery packs are systematically investigated under varying conditions, including inconsistent capacity, internal resistance, charge, and aging rates. Detailed discussions on the applicability of active and passive balancing systems are conducted based on simulation results. Key conclusions are summarized below.

1. Parallel-connected packs can avoid the need for external balancing systems due to self-balancing mechanisms. However, excessive internal resistance inconsistencies may cause individual cells to experience current rates that exceed the pack averages, which accelerates aging and poses safety risks.
2. In series-connected packs, inconsistencies in capacity and charge accelerate degradation, with charge inconsistency caused by different CE and initial SOC being the primary factor. Capacity inconsistency can only be addressed through active balancing systems, while both active and passive balancing systems are effective for packs with charge inconsistencies. Although internal resistance inconsistencies have a relatively minor impact on the capacity of series-connected packs, they do constrain power performance.
3. For packs with well-controlled capacity and thermal uniformity, a passive balancing current of 0.001 C can eliminate up to 3.8% capacity loss within 15 cycles. Therefore, pre-assembly capacity screening and thermal management during operation are critical. Under these conditions, passive balancing systems can significantly reduce complexity and costs.

Future advancements in rapid pack assembly screening technologies and more efficient balancing strategies will enhance pack lifespan and operational safety. Furthermore, constructing more precise system-level thermal models will assist in the prediction of consistency evolution and enable early-stage diagnostics for cells exhibiting consistency deterioration.

Author Contributions: Conceptualization, Y.D. and J.L.; Methodology, Q.Z., J.L. and Y.D.; Software, Investigation, and Validation, Y.D. and W.Y.; Writing—Original Draft, Y.D. and W.Y.; Reviewing and Editing, Q.Z., J.W., J.L. and Y.D. All authors have read and agreed to the published version of the manuscript.

Funding: This research was funded by National Natural Science Foundation of China, Grant 52407246.

Data Availability Statement: The original contributions presented in this study are included in the article. Further inquiries can be directed to the corresponding author.

Conflicts of Interest: The authors declare no conflicts of interest.

References

1. Ashok, B.; Kannan, C.; Mason, B.; Ashok, S.D.; Indragandhi, V.; Patel, D.; Wagh, A.S.; Jain, A.; Kavitha, C. Towards Safer and Smarter Design for Lithium-Ion-Battery-Powered Electric Vehicles: A Comprehensive Review on Control Strategy Architecture of Battery Management System. *Energies* **2022**, *15*, 4227. [CrossRef]
2. Wang, Y.; Zhao, Y.; Zhou, S.; Yan, Q.; Zhan, H.; Cheng, Y.; Yin, W. Impact of Individual Cell Parameter Difference on the Performance of Series–Parallel Battery Packs. *ACS Omega* **2023**, *8*, 10512–10524. [CrossRef] [PubMed]
3. Tian, J.; Fan, Y.; Pan, T.; Zhang, X.; Yin, J.; Zhang, Q. A Critical Review on Inconsistency Mechanism, Evaluation Methods and Improvement Measures for Lithium-Ion Battery Energy Storage Systems. *Renew. Sustain. Energy Rev.* **2024**, *189*, 113978. [CrossRef]
4. Dhanaselvam, J.; Rukkumani, V.; Saravanakumar, K.; Rajesh, R. A Critical Review on Key Issues of Performance Degradation Factors for Lithium-Ion Batteries. *IOP Conf. Ser. Earth Environ. Sci.* **2024**, *1375*, 012021. [CrossRef]

5. Kumar, N.; Ramakrishnan, S.M.; Panchapakesan, K.; Subramaniam, D.; Masters, I.; Dowson, M.; Das, A. In-Depth Evaluation of Micro-Resistance Spot Welding for Connecting Tab to 18,650 Li-Ion Cells for Electric Vehicle Battery Application. *Int. J. Adv. Manuf. Technol.* **2022**, *121*, 6581–6597. [CrossRef]
6. Ghaeminezhad, N.; Wang, Z.; Ouyang, Q. A Review on Lithium-Ion Battery Thermal Management System Techniques: A Control-Oriented Analysis. *Appl. Therm. Eng.* **2023**, *219*, 119497. [CrossRef]
7. Yu, H.; Wang, L.; Zhang, Z.; Li, Y.; Yang, S.; He, X. Insight Understanding of External Pressure on Lithium Plating in Commercial Lithium-Ion Batteries. *Adv. Funct. Mater.* **2024**, *34*, 2406966. [CrossRef]
8. Roy, P.K.; Shahjalal, M.; Shams, T.; Fly, A.; Stoyanov, S.; Ahsan, M.; Haider, J. A Critical Review on Battery Aging and State Estimation Technologies of Lithium-Ion Batteries: Prospects and Issues. *Electronics* **2023**, *12*, 4105. [CrossRef]
9. Schomburg, F.; Heidrich, B.; Wennemar, S.; Drees, R.; Roth, T.; Kurrat, M.; Heimes, H.; Jossen, A.; Winter, M.; Cheong, J.Y.; et al. Lithium-Ion Battery Cell Formation: Status and Future Directions towards a Knowledge-Based Process Design. *Energy Environ. Sci.* **2024**, *17*, 2686–2733. [CrossRef]
10. Uzair, M.; Abbas, G.; Hosain, S. Characteristics of Battery Management Systems of Electric Vehicles with Consideration of the Active and Passive Cell Balancing Process. *World Electr. Veh. J.* **2021**, *12*, 120. [CrossRef]
11. Mohammadi, F. Lithium-Ion Battery State-of-Charge Estimation Based on an Improved Coulomb-Counting Algorithm and Uncertainty Evaluation. *J. Energy Storage* **2022**, *48*, 104061. [CrossRef]
12. Simolka, M.; Heger, J.-F.; Traub, N.; Kaess, H.; Friedrich, K.A. Influence of Cycling Profile, Depth of Discharge and Temperature on Commercial LFP/C Cell Ageing: Cell Level Analysis with ICA, DVA and OCV Measurements. *J. Electrochem. Soc.* **2020**, *167*, 110502. [CrossRef]
13. Spitthoff, L.; Shearing, P.R.; Burheim, O.S. Temperature, Ageing and Thermal Management of Lithium-Ion Batteries. *Energies* **2021**, *14*, 1248. [CrossRef]
14. Lipu, M.S.H.; Hannan, M.A.; Karim, T.F.; Hussain, A.; Hussain, A.; Saad, M.H.M.; Ayob, A.; Miah, M.S.; Miah, M.S.; Miah, M.S.; et al. Intelligent Algorithms and Control Strategies for Battery Management System in Electric Vehicles: Progress, Challenges and Future Outlook. *J. Clean. Prod.* **2021**, *292*, 126044. [CrossRef]
15. Tan, C.M.; Yang, Y.; Kumar, K.J.M.; Mishra, D.D.; Liu, T.-Y. Addressing Practical Challenges of LiB Cells in Their Pack Applications. *Sci. Rep.* **2024**, *14*, 10126. [CrossRef]
16. Xia, B.; Yang, Y.; Zhou, J.; Chen, G.; Liu, Y.; Wang, H.; Wang, M.; Lai, Y. Using Self Organizing Maps to Achieve Lithium-Ion Battery Cells Multi-Parameter Sorting Based on Principle Components Analysis. *Energies* **2019**, *12*, 2980. [CrossRef]
17. Feng, X.-H.; Li, Z.-Z.; Gu, F.-S.; Zhang, M.-L. Structural Design and Optimization of Air-Cooled Thermal Management System for Lithium-Ion Batteries Based on Discrete and Continuous Variables. *J. Energy Storage* **2024**, *86*, 111202. [CrossRef]
18. Zhang, H.; Zhang, Y.; Huang, L.; Song, J.; Huang, Z. Study on the Influence of Connection Structure between Batteries on Battery Pack Performance. *Electronics* **2024**, *13*, 817. [CrossRef]
19. Ashraf, A.; Ali, B.; Alsunjury, M.S.A.; Goren, H.; Kilicoglu, H.; Hardan, F.; Tricoli, P. Review of Cell-Balancing Schemes for Electric Vehicle Battery Management Systems. *Energies* **2024**, *17*, 1271. [CrossRef]
20. Xie, J.; Lin, H.; Qu, J.; Shi, L.; Chen, Z.; Chen, S.; Zheng, Y. Hierarchical Structure-Based Wireless Active Balancing System for Power Batteries. *Energies* **2024**, *17*, 4602. [CrossRef]
21. Sun, W.; Li, Y.; Liu, L.; Mai, R. A Switched-capacitor Battery Equalization Method for Improving Balancing Speed. *IET Electr. Power Appl.* **2021**, *15*, 555–569. [CrossRef]
22. Abareshi, M.; Hamzeh, M.; Farhangi, S.; Alavi, S.M.M. Robust Control of a Forward-converter Active Battery Cell Balancing. *IET Power Electron.* **2023**, *16*, 1271–1280. [CrossRef]
23. Duraisamy, T.; Kaliyaperumal, D. Adaptive Passive Balancing in Battery Management System for E-mobility. *Int. J. Energy Res.* **2021**, *45*, 10752–10764. [CrossRef]
24. Hemavathi, S. Overview of Cell Balancing Methods for Li-ion Battery Technology. *Energy Storage* **2021**, *3*, e203. [CrossRef]
25. Xia, Q.; Yang, D.; Wang, Z.; Ren, Y.; Sun, B.; Feng, Q.; Qian, C. Multiphysical Modeling for Life Analysis of Lithium-Ion Battery Pack in Electric Vehicles. *Renew. Sustain. Energy Rev.* **2020**, *131*, 109993. [CrossRef]
26. Wang, Y.; Tian, J.; Sun, Z.; Wang, L.; Xu, R.; Li, M.; Chen, Z.; Chen, Z.; Chen, Z.; Chen, Z. A Comprehensive Review of Battery Modeling and State Estimation Approaches for Advanced Battery Management Systems. *Renew. Sustain. Energy Rev.* **2020**, *131*, 110015. [CrossRef]
27. Zhou, W.; Zheng, Y.; Pan, Z.; Lu, Q. Review on the Battery Model and SOC Estimation Method. *Processes* **2021**, *9*, 1685. [CrossRef]
28. Lai, X.; Zhou, L.; Zhu, Z.; Zheng, Y.; Sun, T.; Shen, K. Experimental Investigation on the Characteristics of Coulombic Efficiency of Lithium-Ion Batteries Considering Different Influencing Factors. *Energy* **2023**, *274*, 127408. [CrossRef]
29. Zhang, Z.; Cheng, X.; Lu, Z.-Y.; Gu, D.-J. SOC Estimation of Lithium-Ion Battery Pack Considering Balancing Current. *IEEE Trans. Power Electron.* **2018**, *33*, 2216–2226. [CrossRef]
30. Hu, L.; Hu, X.S.; Che, Y.H.; Feng, F.; Lin, X.K.; Zhang, Z.Y. Reliable State of Charge Estimation of Battery Packs Using Fuzzy Adaptive Federated Filtering. *Appl. Energy* **2020**, *262*, 15. [CrossRef]

31. Song, Z.; Yang, X.-G.; Yang, N.; Delgado, F.P.; Hofmann, H.; Sun, J. A Study of Cell-to-Cell Variation of Capacity in Parallel-Connected Lithium-Ion Battery Cells. *eTransportation* **2021**, *7*, 100091. [CrossRef]
32. Gong, X.; Xiong, R.; Mi, C.C. Study of the Characteristics of Battery Packs in Electric Vehicles With Parallel-Connected Lithium-Ion Battery Cells. *IEEE Trans. Ind. Appl.* **2015**, *51*, 1872–1879. [CrossRef]
33. Lv, J.; Song, W.; Feng, Z.; Li, Y.; Ding, Y. Performance and Comparison of Equalization Methods for Lithium Ion Batteries in Series. *Int. J. Energy Res.* **2021**, *45*, 4669–4680. [CrossRef]

3.3.4 基于双曲正切函数的采摘机械臂滑模跟踪控制（B 类）

华南农业大学学报 Journal of South China Agricultural University 2025, 45(0): 1-8 DOI: 10.7671/j.issn.1001-411X.202406029

李杰浩, 刘宏鲜, 罗群斐, 等. 基于双曲正切函数的采摘机械臂滑模跟踪控制 [J]. 华南农业大学学报, 2025, 45(0): 1-8.
LI Jiehao, LIU Hongxian, LUO Qunfei, et al. Trajectory Tracking Sliding Mode Control of Picking Manipulator Based on Hyperbolic Tangent Function[J]. Journal of South China Agricultural University, 2025, 45(0): 1-8.

基于双曲正切函数的采摘机械臂滑模跟踪控制

李杰浩，刘宏鲜，罗群斐，卢家欢

(华南农业大学 工程学院/南方农业机械与装备关键技术教育部重点实验室, 广东 广州 510642)

摘要:【目的】解决机械臂在农业领域应用中末端轨迹跟踪控制问题，确保农业采摘机器人采摘末端高精度轨迹跟踪和系统稳定运行。【方法】提出一种基于双曲正切函数采摘机械臂的滑模跟踪控制方法。根据逆向运动学构建基于工作空间的机械臂动力学模型，设计双曲正切函数的滑模跟踪控制器，由李雅普诺夫函数保证控制系统的渐进稳定性。在 MATLAB/Simulink 环境中搭建机械臂仿真控制系统进行控制算法验证，分析滑模控制器对机械臂末端轨迹的跟踪效果。【结果】仿真试验结果表明，与切换函数滑模控制器相比，基于双曲正切函数的滑模控制器能够实现高精度的轨迹跟踪和稳定控制，提高了末端轨迹跟踪的收敛速度，减小了机械臂末端轨迹跟踪控制误差，并使末端轨迹跟踪曲线的收敛时间减少 50%，有效提高了机械臂采摘系统的实时性和跟踪精度。【结论】研究可为机械臂采摘的实际应用提供有效的控制方法。

关键词: 采摘机械臂；工作空间；滑模控制；双曲正切函数；轨迹跟踪

中图分类号: **文献标志码:** A **文章编号:** 1001-411X(2025)00-0001-08

Trajectory Tracking Sliding Mode Control of Picking Manipulator Based on Hyperbolic Tangent Function

LI Jiehao, LIU Hongxian, LUO Qunfei, LU Jiahuan

(College of Engineering, South China Agricultural University/Key Laboratory of Key Technology on Agricultural Machine and Equipment, Ministry of Education, South China Agricultural University, Guangzhou 510642, China)

Abstract: 【Objective】To solve the problem of endpoint trajectory tracking control in the application of mechanical arms in the agricultural field, and ensure the high-precision trajectory tracking and stable operation of the agricultural picking robot picking end. 【Method】It is suggested to use a hyperbolic tangent function-based sliding mode tracking control approach for a picking robot arm. A model of the manipulator dynamics based on the workspace was built using inverse kinematics, and a sliding mode tracking controller for the hyperbolic tangent function was created. The asymptotic stability of the control system was guaranteed by the Lyapunov function. The simulation control system of the manipulator was built in the MATLAB/Simulink environment to verify the control algorithm, and the tracking effect of the sliding mode controller on the end trajectory of the manipulator was analyzed. 【Result】The simulation test results showed that the sliding mode

收稿日期: 2024–06–21

首发网址:

作者简介: 李杰浩，博士，副教授，主要研究方向为机器人运动驱动与控制技术，E-mail: jiehao.li@scau.edu.cn；通信作者：卢家欢，博士，副教授，主要研究方向为智能装备设计，E-mail: jhlu@scau.edu.cn

基金项目: 广州市科技计划项目 (2024A04J4140)；机器人技术与系统全国重点实验室开放基金 (SKLRS-2024-KF-08)；国家自然科学基金 (62203176)

controller based on the hyperbolic tangent function achieved high-precision trajectory tracking and stable control, improved the convergence speed of the terminal trajectory tracking, reduced the robot end trajectory tracking control error, and reduced the convergence time of the terminal trajectory tracking curve by 50%, effectively improved the real-time performance and tracked accuracy of the robot picking system compared with the switching function sliding mode controller. 【Conclusion】The research can provide an effective control method for the practical application of robotic arm picking.

Key words: Picking manipulator; Workspace; Sliding mode control; Hyperbolic tangent function; Trajectory tracking

农业机械的发展已逐步走向智能化、精细化。机器人技术在农业生产领域的应用将极大地改变农业生产作业方式，实现高效生产[1]。水果、蔬菜采收作业环境极其复杂、劳动强度高、季节性强，常因缺乏足够的劳动力而错失最佳采收时机。实现机器人采摘是果蔬实时采收和低成本收获的有效方案，并且可有效降低劳动强度、提高作业效率[2-4]。

在复杂农业作业环境中，未知干扰易造成农业机器人采摘机械臂末端轨迹的跟踪误差。针对机械臂末端轨迹跟踪控制精度问题，已提出了 PID 控制、ADRC 控制、滑模控制、鲁棒控制、神经网络控制等多种算法[5-9]，但实际应用中往往是多种控制算法互取优势结合使用[10-11]。其中，滑模变结构控制算法[12-13] 含有切换控制项函数，本质上是一种特殊的非线性控制算法，适用于属于多输入多输出的非线性系统的机械臂。张旭辉等[14] 针对传统滑模控制算法在悬臂式掘进机轨迹跟踪控制中存在的缺陷问题，改进传统指数趋近律函数，并引入位姿偏差并增加幂次函数项，同时采用反步法设计新的切换函数以代替符号切换函数，改进后的滑模控制器实现了系统的快速收敛并削弱了系统抖振。Baek 等[15] 在机械臂的控制研究中，采用延时估计技术提出一种自适应滑模控制器，在自适应律函数中添加有关速度的可调正增益和正设计参数，实现了良好的跟踪性能和较小的抖振效应。张蕾等[16] 针对复合扰动对机械臂轨迹跟踪精度的影响，设计了基于非奇异积分终端滑模面的轨迹跟踪控制器，所采用积分项使系统的鲁棒性得到提高，同时采用分数指数项来加快收敛速度。贾华等[17] 针对机械臂模型未知且存在外界干扰时的跟踪控制问题，提出基于动力学模块分块逼近的神经网络终端滑模的控制方案，同时采用多组神经网络分块逼近动力学模型参数实现模型重构和权值在线调整，与整体逼近算法相比，分块逼近使机械臂关节最大稳态误差减少 83.7%，能够抵抗末端负载变化情况。上述研究大多基于机械臂的控制关节角度进行，在实际工程应用中，机械臂的应用多关注于末端轨迹的跟踪控制。

机械臂在实际工程应用上，不仅要考虑外部干扰和不确定性问题，还需要考虑平滑、能耗及避障等方面。Lin 等[18] 在研究气动人工肌肉驱动的机械臂末端圆形轨迹跟踪时，在控制算法中采用遗传算法进行参数识别，设计出高阶滑模反馈控制算法实现圆形轨迹跟踪，仿真结果表明控制器在抵抗外界干扰和建模不确定性方面具有更强的鲁棒性。Wand 等[19] 针对机械臂轨迹跟踪问题提出无模型自适应滑模控制策略，采用延时估计技术对未知动力学模型进行估计，同时设计自适应律来处理延时估计误差，在控制算法中引入改进的漏斗函数来控制跟踪误差，集合成一种基于新型漏斗函数的非奇异快速终端滑模控制器以增强系统的跟踪控制性能。Zhao 等[20] 研究了在没有速度测量情况下机械臂轨迹跟踪问题，提出一种由工作空间期望轨迹估计器、自适应律及速度观测器组成的协作跟踪控制方案，估计器用来产生期望轨迹，观测器可获得工作空间速度，并基于观测器和估计器设计出自适应控制律。倪元相等[21] 研究了基于输出反馈式神经网络的三自由度机械臂轨迹跟踪控制问题，文中提出以 B 样条函数为基函数的人工神经网络，采用基于粒子群优化算法的离线训练方法确定控制器增益，并在关节空间和笛卡儿空间中验证了方案的可行性。

机械臂是一个复杂的非线性系统，而农业作业环境又极其复杂且作业对象物理特性复杂，诸如作业目标自然生长无序可循，每次作业目标其位姿各不相同等，均影响机械臂采摘作业灵活性、反应速度、作业精度，易造成严重的动态扰动[22-23]。实现采摘机械臂灵活、高效、精准作业是研究机械臂跟踪控制的着眼点，本文针对机械臂在农业领域应用中末端轨迹跟踪控制问题，提出基于双曲正切函数的控制策略。在 MATLAB/Simulink 仿真环境中搭建

机械臂控制系统，验证所设计的控制器对轨迹跟踪的有效性。

1　问题描述

1.1　试验平台简介

果蔬采摘机器人主要由无人移动平台、视觉识别系统、机械臂操作系统和末端执行机构组成。基于此搭建实验室环境下的采摘平台，如图 1 所示。控制机械臂末端按期望轨迹到达采摘目标是农业采摘机器人的关键技术之一，本文针对其轨迹跟踪控制问题展开研究，进行二自由度机械臂模型控制算法仿真验证。

图 1　六自由度采摘机械臂

Fig. 1　6-DOF picking manipulator

1.2　坐标转换

数学分析中，机械臂的动力学模型通常是基于关节角度构建的，进而通过设计关节扭矩实现关节角度和角速度的跟踪。但在实际应用中，机械臂的控制是重点研究末端轨迹的稳定跟踪控制，因此需要建立工作空间中机械臂末端节点直角坐标的动力学模型。

如图 2 所示，根据几何关系计算出机械臂末端在工作空间中的位置为：

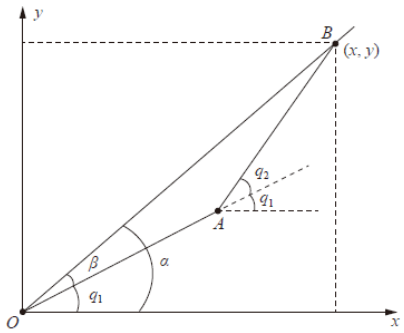

图 2　二自由度机械臂简化图

Fig. 2　Simplified diagram of 2-DOF manipulator

$$\begin{cases} x = l_1\cos q_1 + l_2\cos(q_1+q_2) \\ y = l_1\sin q_1 + l_2\sin(q_1+q_2) \end{cases}, \tag{1}$$

式中：x、y分别为机械臂末端端点横坐标、坐标值；l_1、l_2分别为二自由度机械臂连杆 OA、AB 的长度；q_1、q_2分别为连杆 OA、AB 的关节角度。

依据直角三角形定理得：

$$x^2+y^2 = l_1^2+l_2^2+2l_1l_2\cos(q_2), \tag{2}$$

化简式 (2) 得：

$$q_2 = \arccos\left(\frac{x^2+y^2-l_1^2-l_2^2}{2l_1l_2}\right), \tag{3}$$

根据图 2 中几何关系可得：

$$\alpha = \arctan\frac{y}{x}, x \geq 0, \tag{4}$$

或

$$\alpha = \pi + \arctan\frac{y}{x}, x < 0, \tag{5}$$

在ΔOAB中，根据三角形余弦定理得：

$$l_2^2 = l_1^2 + (x^2+y^2) - 2l_1\sqrt{x^2+y^2}\cos\beta, \tag{6}$$

由式 (6) 可求得：

$$\beta = \arccos\frac{x^2+y^2+l_1^2-l_2^2}{2l_1\sqrt{x^2+y^2}}, \tag{7}$$

从而

$$q_1 = \begin{cases} \alpha-\beta, q_2 > 0 \\ \alpha+\beta, q_2 \leq 0 \end{cases}, \tag{8}$$

定义$z = [x\ y]$, $q = [q_1\ q_2]$,

则

$$\mathrm{d}z = \frac{\partial z}{\partial q}\mathrm{d}q, \tag{9}$$

定义

$$J = \frac{\partial z}{\partial q}, \tag{10}$$

则

$$\mathrm{d}z = J\cdot\mathrm{d}q, \tag{11}$$

其中，$J = \begin{bmatrix} \frac{\partial x}{\partial q_1} & \frac{\partial x}{\partial q_2} \\ \frac{\partial y}{\partial q_1} & \frac{\partial y}{\partial q_2} \end{bmatrix}$，

J——机械臂末端端点速度与机械臂关节速度之间关系的雅可比矩阵。

由式 (1) 可得：

$$\frac{\partial x}{\partial q_1} = -l_1\sin q_1 - l_2\sin(q_1+q_2), \tag{12}$$

$$\frac{\partial x}{\partial q_2} = -l_2 \sin(q_1 + q_2), \tag{13}$$

$$\frac{\partial y}{\partial q_1} = l_1 \cos q_1 + l_2 \cos(q_1 + q_2), \tag{14}$$

$$\frac{\partial y}{\partial q_2} = l_2 \cos(q_1 + q_2), \tag{15}$$

雅可比矩阵$J(q)$则有如下表示：

$$J(q) = \begin{bmatrix} -l_1 \sin q_1 - l_2 \sin(q_1 + q_2) & -l_2 \sin(q_1 + q_2) \\ l_1 \cos q_1 + l_2 \cos(q_1 + q_2) & l_2 \cos(q_1 + q_2) \end{bmatrix}$$

雅可比矩阵求导可得：

$$\dot{J}(q) = \begin{bmatrix} -l_1 \cos q_1 - l_2 \cos(q_1 + q_2) & -l_2 \cos(q_1 + q_2) \\ -l_1 \sin q_1 - l_2 \sin(q_1 + q_2) & -l_2 \sin(q_1 + q_2) \end{bmatrix} \dot{q}_1 + \begin{bmatrix} -l_2 \cos(q_1 + q_2) & -l_2 \cos(q_1 + q_2) \\ -l_2 \sin(q_1 + q_2) & -l_2 \sin(q_1 + q_2) \end{bmatrix} \dot{q}_2$$

根据$J(q)$和$\dot{J}(q)$可知，$J(q)$是由结构决定的，在此假设$J(q)$在有界的工作空间中是非奇异的。

1.3 机械臂建模

基于关节角度的机械臂模型为：

$$D(q)\ddot{q} + C(q,\dot{q})\dot{q} + G(q) = \tau, \tag{16}$$

式中：$q \in R^n$——关节变量向量；

$\tau \in R^n$——执行机构施加的关节扭矩向量；

$D(q) \in R^{n \times n}$——对称正定惯性矩阵；

$C(q,\dot{q}) \in R^{n \times n}$——哥氏力和离心力向量；

$G(q) \in R^n$——重力向量。

在工程实际应用中，为实现机械臂末端轨迹的跟踪控制目标，需要将基于关节角度的动力学方程转换为基于直角坐标的动力学方程，即在直角坐标系下研究末端力与轨迹跟踪目标的数值关系。

在静态平衡状态下，机械臂末端力F与关节力矩τ之间存在线性映射关系，根据虚功原理可知其关系式如下：

$$\tau = J^T(q)F, \tag{17}$$

变形得：

$$F = J^{-T}(q)\tau, \tag{18}$$

由公式 (10) 得:

$$\dot{z} = J \cdot \dot{q}, \tag{19}$$

则有：

$$\dot{q} = J^{-1}\dot{z}, \tag{20}$$

$$\ddot{z} = \dot{J}\dot{q} + J\ddot{q} = \dot{J}J^{-1}\dot{z} + J\ddot{q}, \tag{21}$$

根据式 (21) 可得出关节角加速度为：

$$\ddot{q} = J^{-1}\left(\ddot{z} - \dot{J}J^{-1}\dot{z}\right), \tag{22}$$

将式 (22) 代入式 (16)，可得：

$$DJ^{-1}\left(\ddot{z} - \dot{J}J^{-1}\dot{z}\right) + CJ^{-1}\dot{z} + G = \tau, \tag{23}$$

即：

$$DJ^{-1}\ddot{z} - DJ^{-1}\dot{J}J^{-1}\dot{z} + CJ^{-1}\dot{z} + G = \tau, \tag{24}$$

整理得：

$$DJ^{-1}\ddot{z} + \left(C - DJ^{-1}\dot{J}\right)J^{-1}\dot{z} + G = \tau, \tag{25}$$

等式两边同时乘以J^{-T}可得：

$$J^{-T}\left(DJ^{-1}\ddot{z} + \left(C - DJ^{-1}\dot{J}\right)J^{-1}\dot{z} + G\right) = J^{-T}\tau, \tag{26}$$

同时，考虑建模不确定性，从而得到如下机械臂动力学模型：

$$D_z\ddot{z} + C_z\dot{z} + G_z + \Delta(q,\dot{q},\ddot{q}) = F, \tag{27}$$

其中，$D_z = J^{-T}DJ^{-1}$，$C_z = J^{-T}\left(C - DJ^{-1}\dot{J}\right)J^{-1}$，$G_z = J^{-T}G$，$\|\Delta(q,\dot{q},\ddot{q})\| \le \eta$。

上述机械臂动态方程具有 2 个特性：惯性矩阵D_z对称正定；矩阵$\dot{D}_z - 2C_z$是斜对称的。

1.4 控制目标

在二维直角坐标系中研究二关节机械臂末端轨迹跟踪控制问题，因此，控制器的控制对象是末端端点在横轴和纵轴上的位置和速度。设横轴方向的位置为x，纵轴上的位置为y，记为$z = [x\ y]$。末端轨迹为时间的函数，记为$z(t)$。假设$z_d(t)$是在工作空间中的理想轨迹，则$\dot{z}_d(t)$和$\ddot{z}_d(t)$分别是理想的速度和加速度。

末端轨迹跟踪误差的定义如下：

$$e(t) = z_d(t) - z(t), \tag{28}$$

末端速度跟踪误差：

$$\dot{e}(t) = \dot{z}_d(t) - \dot{z}(t), \tag{29}$$

上述跟踪误差记为控制目标，设计控制器使控制对象能够快速稳定地跟踪期望目标$z_d(t)$和$\dot{z}_d(t)$，即跟踪误差$e(t) \to 0$，$\dot{e}(t) \to 0$。

2 控制器的设计

在传统的滑模控制器设计中，切换控制项通常采用一般切换函数——符号函数或滑模面函数，但此类切换函数会引起控制系统的抖振。为解决这一抖

振问题，采用连续的双曲正切函数代替一般切换函数，双曲正切函数的陡度可调节切换控制的切换程度。

双曲正切函数定义为

$$\tanh\frac{x'}{\varepsilon}=\frac{e^{\frac{x'}{\varepsilon}}-e^{-\frac{x'}{\varepsilon}}}{e^{\frac{x'}{\varepsilon}}+e^{-\frac{x'}{\varepsilon}}},\tag{30}$$

式中，ε——双曲正切函数的陡度且$\varepsilon>0$。

引理 1：针对任意给定的实数x'，存在下面的不等式

$$x'\tanh\left(\frac{x'}{\varepsilon}\right)=\left|x'\tanh\left(\frac{x'}{\varepsilon}\right)\right|=|x'|\left|\tanh\left(\frac{x'}{\varepsilon}\right)\right|\geq 0,\tag{31}$$

$$0\leq|x'|-x'\tanh\left(\frac{x'}{\varepsilon}\right)\leq\mu\varepsilon,\tag{32}$$

式中，$\mu=0.2785$。

引理 2：假设 f，$V:[0,\infty)\in\mathrm{R}$，如果存在$\dot{V}\leq-\alpha V+\mathrm{f}$，$\forall t\geq t_0\geq 0$，则

$$V(t)\leq e^{-\alpha(t-t_0)}V(t_0)+\int_{t_0}^{t}e^{-\alpha(t-\tau)}\mathrm{f}(\tau)\mathrm{d}\tau,\tag{33}$$

式中，α为任意实数。

由轨迹跟踪误差公式得：

$$z(t)=z_d(t)-e(t),\tag{34}$$

求导得：

$$\dot{z}(t)=\dot{z}_d(t)-\dot{e}(t),\tag{35}$$

定义

$$\dot{z}_r(t)=\dot{z}_d(t)+\Lambda e(t),\tag{36}$$

设计滑模函数为

$$s(t)=\dot{z}_r(t)-\dot{z}(t)=\ddot{e}(t)+\Lambda e(t),\tag{37}$$

式中，Λ为正定矩阵。

根据机械臂动力学模型公式 (27)，设计一种具有光滑双曲正切切换的滑模控制器为

$$F=D_z\ddot{z}_r+C_z\dot{z}_r+G_z+Ks+\eta tanh\frac{s}{\varepsilon},\tag{38}$$

式中，K表示控制器的增益且$K>0$。

综上分析，机械臂末端轨迹跟踪控制框图见图 3。

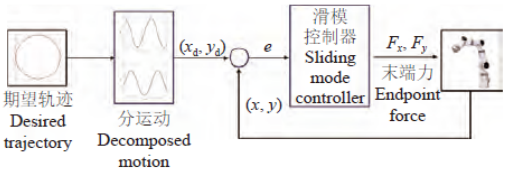

图 3　机械臂跟踪控制框图

Fig. 3　Block diagram of manipulator tracking control

3　稳定性验证

通过构造 Lyapunov 函数来证明所设计的滑模控制器满足系统稳定性的要求。

将控制律式 (38) 代入式 (27) 中，得：

$$D_z\ddot{z}+C_z\dot{z}+G_z+\Delta(q,\dot{q},\ddot{q})=D_z\ddot{z}_r+C_z\dot{z}_r+G_z+Ks+\eta tanh\frac{s}{\varepsilon},\tag{39}$$

将$\dot{z}(t)=\dot{z}_r(t)-s(t)$，$\ddot{z}(t)=\ddot{z}_r(t)-\dot{s}(t)$代入公式 (39) 得：

$$D_z\dot{s}+C_zs+Ks+\eta tanh\frac{s}{\varepsilon}-\Delta(q,\dot{q},\ddot{q})=0$$

由于$D_z(q)$为对称正定，则可定义 Lyapunov 函数为

$$V=\frac{1}{2}s^TD_z(q)s,\tag{40}$$

则

$$\dot{V}=s^TD_z\dot{s}+\frac{1}{2}s^T\dot{D}_zs,\tag{41}$$

由于矩阵$\dot{D}_z(q)-2C_z(q,\dot{q})$是斜对称的，则$s^T\dot{D}_z-2C_zs=0$，即$\frac{1}{2}s^T\dot{D}_zs=s^TC_zs$，代入式 (41) 得：

$$\dot{V}=s^TD_z\dot{s}+s^TC_zs=s^T(D_z\dot{s}+C_zs)=s^T\left(-Ks-\eta\tanh\frac{s}{\varepsilon}+\Delta(q,\dot{q},\ddot{q})\right),\tag{42}$$

根据引理 1，可得：

$$s^T\left(-\eta\tanh\frac{s}{\varepsilon}+\Delta(q,\dot{q},\ddot{q})\right)=-\eta s^T\tanh\frac{s}{\varepsilon}+s^T\Delta(q,\dot{q},\ddot{q})\leq-\eta\|s\|+\eta\mu s+s^T\Delta(q,\dot{q},\ddot{q})\leq\eta\mu s,\tag{43}$$

式中，$\mu=0.2785$

于是

$$\dot{V}\leq-s^TKs+\eta\mu s\leq-\lambda_{\min}(K)s^Ts+\eta\mu s=-\frac{2\lambda_{\min}(K)}{\lambda_{\max}(D_z)}\frac{1}{2}\lambda_{\max}(D_z)s^Ts+\eta\mu s\leq-2\lambda V+b-2\lambda V+b,\tag{44}$$

式中，$\lambda_{\max}(D_x)$为D_x的最大特征值；$\lambda_{\min}(K)$为K的最大特征值。

$$\lambda=\frac{\lambda_{\min}(K)}{\lambda_{\max}(D_z)},\tag{45}$$

$$b=\eta\mu s,\tag{46}$$

根据$\dot{V}\leq-2\lambda V+b$，采用引理 2，可得：

$$V(t) \le e^{-2\lambda(t-t_0)}V(t_0) + \mathrm{b}e^{-2\lambda t}\int_{t_0}^{t} e^{2\lambda t}d\tau = e^{-2\lambda(t-t_0)}V(t_0) + \frac{\mathrm{b}e^{-2\lambda t}}{2\lambda}\left(e^{2\lambda t} - e^{2\lambda t_0}\right) = e^{-2\lambda(t-t_0)}V(t_0) + \frac{\mathrm{b}}{2\lambda}\left(1 - e^{-2\lambda(t-t_0)}\right), \quad (47)$$

则

$$\lim_{t\to\infty} V(t) \le \frac{\eta\mu\varepsilon}{2\lambda}, \quad (48)$$

根据式 (48) 可知，跟踪误差和误差导数渐进收敛，收敛精度取决于ε、λ和η，即ε越小，K 越大，Δ越小，收敛效果就越好。

4 仿真分析

为验证文中所设计的控制器的有效性和可靠性，以上述二自由度机械臂为控制对象，其动力学方程为式 (13)，经过计算可得出相关矩阵表达式如下：

$$D(q) = \begin{bmatrix} \mathrm{p}_1 + \mathrm{p}_2 + 2\mathrm{p}_3\cos q_2 & \mathrm{p}_2 + \mathrm{p}_3\cos q_2 \\ \mathrm{p}_2 + \mathrm{p}_3\cos q_2 & \mathrm{p}_2 \end{bmatrix}, \quad (49)$$

$$C(q,\dot{q}) = \begin{bmatrix} -\mathrm{p}_3\dot{q}_2\sin q_2 & -\mathrm{p}_3(\dot{q}_1 + \dot{q}_2)\dot{q}_2\sin q_2 \\ \mathrm{p}_3\dot{q}_1\sin q_2 & 0 \end{bmatrix}, \quad (50)$$

$$G(q) = \begin{bmatrix} \mathrm{p}_4\mathrm{g}\cos q_1 + \mathrm{p}_5\mathrm{g}\cos(q_1 + q_2) \\ \mathrm{p}_5\mathrm{g}\cos(q_1 + q_2) \end{bmatrix}, \quad (51)$$

式中，$\mathrm{p}_1 = (\mathrm{m}_1 + \mathrm{m}_2)\mathrm{l}_1^2$，$\mathrm{p}_2 = \mathrm{m}_2\mathrm{l}_2^2$，$\mathrm{p}_3 = \mathrm{m}_2\mathrm{l}_1\mathrm{l}_2$，$\mathrm{p}_4 = (\mathrm{m}_1 + \mathrm{m}_2)\mathrm{l}_1$，$\mathrm{p}_5 = \mathrm{m}_2\mathrm{l}_2$。$\mathrm{m}_1$，$\mathrm{m}_2$ 为连杆质量。

在直角坐标系中，假设理想跟踪轨迹为 $x_d = \cos t$，$y_d = \sin t$，根据合成运动知识可知，该轨迹是一个半径为 1.0，圆心为(0.0,0.0)的圆。设置机械臂末端轨迹的初始条件为 $z = [1.0\ 1.0]$，$\dot{z} = [0.0\ 0.0]$，末端实际轨迹按逆时针方向进行跟踪。按式 (3) 和 (8) 将工作空间中的关节末端直角坐标(x，y)转为关节角度坐标(q_1，q_2)。

采用工作空间模式公式 (27) 实现被控对象的描述，针对建模不确定性，取 $\Delta(q,\dot{q},\ddot{q}) = 10\sin t$，滑模控制器取式 (35)，并通过虚功原理式 (17) 转化为控制关节角度的实际控制器。控制器的增益选为 $K = \begin{bmatrix} 30 & 0 \\ 0 & 30 \end{bmatrix}$，$\Lambda = \begin{bmatrix} 15 & 0 \\ 0 & 15 \end{bmatrix}$，$\eta = 12$，$\varepsilon = 0.10$。

为体现本文所用控制算法的有效性和优越性，再设计两种不同的控制算法与之进行对比实验。设计在工作空间中机械臂末端轨迹 PD 控制器和基于传统切换函数的滑模控制器。

PD 控制器的控制律表达式为：

$$F_{PD} = D_z\ddot{z}_r + C_z\dot{z}_r + G_z + K_p e + K_d\dot{e}, \quad (52)$$

式中，K_p、K_d 分别表示 PD 控制算法中的比例系数和微分系数矩阵，

取 $K_p = \begin{bmatrix} 30 & 0 \\ 0 & 30 \end{bmatrix}$，$K_d = \begin{bmatrix} 30 & 0 \\ 0 & 30 \end{bmatrix}$。

基于传统切换函数的滑模控制器的控制律表达式为：

$$F_K = D_z\ddot{z}_r + C_z\dot{z}_r + G_z + \mathrm{K}s, \quad (53)$$

其中，$\mathrm{K} > 0$。

基于以上 3 种控制器，在 MATLAB/Simulink 环境中搭建仿真系统，仿真结果如图 4~6 所示。

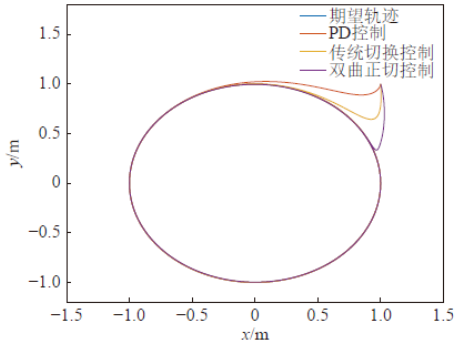

图 4 机械臂末端轨迹跟踪

Fig. 4 Trajectory tracking of the end of the manipulator

从图 4 机械臂末端轨迹跟踪图来看，机械臂末端在 3 种不同算法控制下均能在一定的误差范围内实现圆形轨迹跟踪。跟踪曲线明显表明本文所设计的基于双曲正切的滑模控制器使系统的收敛速度增大。

图 5 a~5d 分别为机械臂末端分运动轨迹跟踪及其误差仿真结果。结合轨迹跟踪图 5a、5b 和误差图 5c、5d 来分析，滑模控制算法在系统收敛时间方面明显由于 PD 控制算法。由图 5b 机械臂末端 y 轴跟踪结果可以看出，切换函数滑模控制器的跟踪开始时间为 1.5s 处，而双曲正切滑模控制器的跟踪开始时间在 1.0s 处，根据 y 轴的速度跟踪误差曲线也可看出，双曲正切控制比切换函数控制在收敛速度方面提高了 50%。

在机械臂末端速度轨迹跟踪曲线图中，双曲正切滑模控制器相比另 2 个控制器来说，尽管其在初始时刻存在较大的误差，但其总体跟踪效果强于切换函数控制器和 PD 控制器，并且速度跟踪的收敛时间降低了 50%，收敛速度相应地提高了 50%。观察图中的跟踪误差曲线可知，本文所提的控制算法

在收敛速度和稳定性方面体现了良好的控制性能，但在响应初始时刻，该算法有急剧地突变，需要对控制算法进行优化以缩小初始变化的误差。根据以上仿真结果及可以看出，该算法在收敛速度方面具有良好的控制性能。

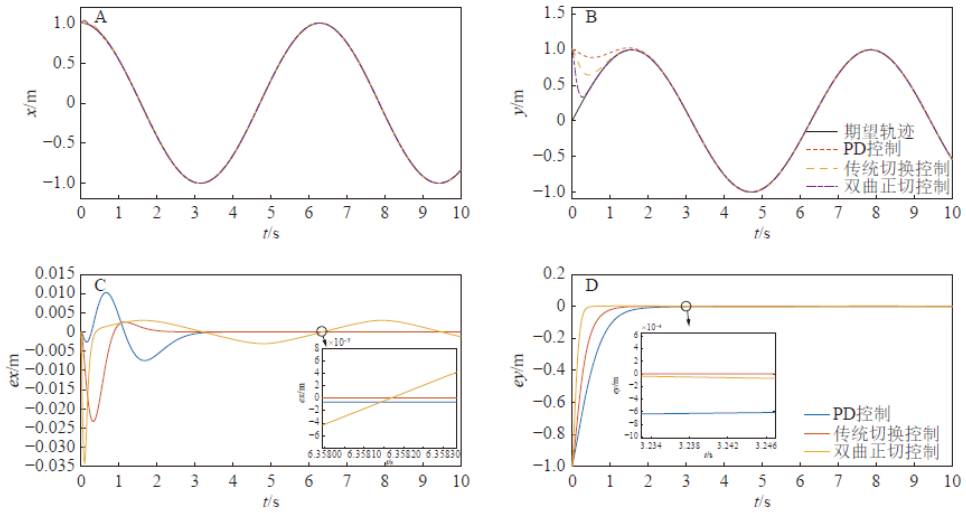

图 5　x 轴和 y 轴轨迹跟踪及其跟踪误差

Fig. 5　Trajectory tracking and tracking errors of x-axis and y-axis

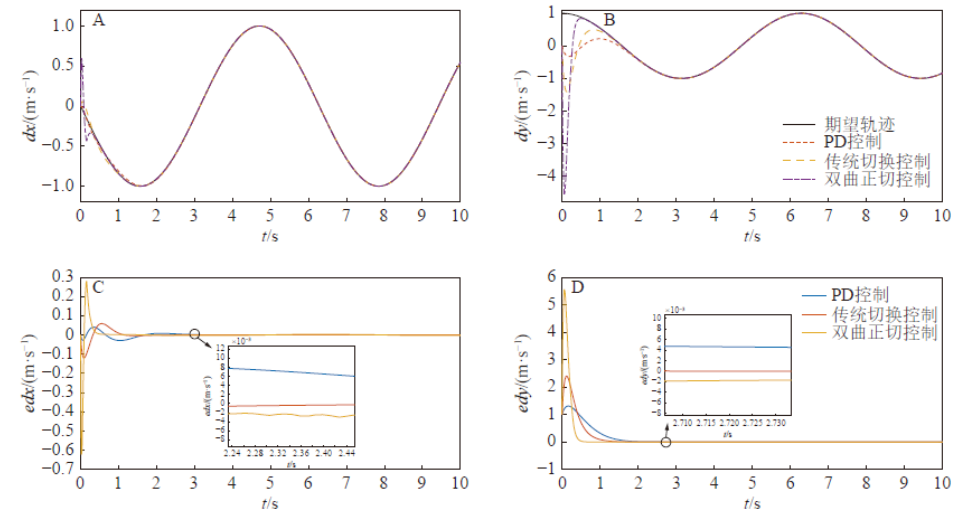

图 6　x 轴和 y 轴的速度跟踪及其跟踪误差

Fig. 6　Velocity tracking and tracking errors of x-axis and y-axis

5　结论

为实现采摘机器人中机械臂末端轨迹高精度跟踪控制，本文提出了一种基于双曲正切函数的滑模控制器。在 Simulink 环境中搭建机械臂控制系统并进行仿真验证，分析比较了 3 种控制器对轨迹跟踪的收敛性能和效果。结果表明：本文设计的滑模控制器能够实现高精度的轨迹跟踪和稳定控制，并使系统收敛时间减少 50%，有效提高了系统收敛速度。研究为后续采摘机械臂奠定了基础。

参考文献：

[1]　刘成良, 贡亮, 苑进, 等. 农业机器人关键技术研究现状与发展趋势[J]. 农业机械学报, 2022, 53(7): 1-22.

[2] 陈青, 殷程凯, 郭自良, 等. 苹果采摘机器人关键技术研究现状与发展趋势[J]. 农业工程学报, 2023, 39(4): 1-15.
[3] 赵春江, 范贝贝, 李瑾, 等. 农业机器人技术进展、挑战与趋势[J]. 智慧农业 (中英文), 2023, 5(4): 1-15.
[4] 孙成宇, 闫建伟, 张富贵, 等. 蔬菜采摘机器人及其关键技术研究进展[J]. 中国农机化学报, 2023, 44(11): 63-72.
[5] LI J H, WANG J Z, PENG H, et al. Fuzzy-torque approximation-enhanced sliding mode control for lateral stability of mobile robot[J]. IEEE Transactions on Systems, Man, and Cybernetics: Systems, 2022, 52(4): 2491-2500.
[6] TRAN D T, TRUONG H V A, AHN K K. Adaptive nonsingular fast terminal sliding mode control of robotic manipulator based neural network approach[J]. International Journal of Precision Engineering and Manufacturing, 2021, 22(3): 417-429.
[7] AHMED S, WANG H P, TIAN Y. Adaptive high-order terminal sliding mode control based on time delay estimation for the robotic manipulators with backlash hysteresis[J]. IEEE Transactions on Systems, Man, and Cybernetics: Systems, 2021, 51(2): 1128-1137.
[8] MA Y J, ZHAO H, LI T. Robust adaptive dual layer sliding mode controller: Methodology and application of uncertain robot manipulator[J]. Transactions of the Institute of Measurement and Control, 2022, 44(4): 848-860.
[9] CHEN J X, LI J M. Fuzzy adaptive iterative learning coordination control of second-order multi-agent systems with imprecise communication topology structure[J]. International Journal of Systems Science, 2018, 49(3): 546-556.
[10] 吴爱国, 刘海亭, 董娜. 机械臂神经网络非奇异快速终端滑模控制[J]. 农业机械学报, 2018, 49(2): 395-404.
[11] 李琦琦, 徐向荣, 张卉. 基于自适应神经网络的机械臂滑模轨迹跟踪控制[J]. 工程设计学报, 2023, 30(4): 512-520.
[12] 刘金琨. 滑模变结构控制 MATLAB 仿真: 先进控制系统设计方法[M]. 3 版. 北京: 清华大学出版社, 2015: 192-195.
[13] 刘金琨. 机器人控制系统的设计与 MATLAB 仿真: 基本设计方法[M]. 北京: 清华大学出版社, 2016: 246-250.
[14] 张旭辉, 李语阳, 杨文娟, 等. 基于改进滑模控制的悬臂式掘进机轨迹跟踪控制[J/OL]. 工程设计学报, 1-12.
[15] BAEK J, JIN M L, HAN S. A new adaptive sliding-mode control scheme for application to robot manipulators[J]. IEEE Transactions on industrial electronics, 2016, 63(6): 3628-3637.
[16] 张蕾, 宋博雄, 田冬雨. 考虑输入饱和的机械臂轨迹跟踪滑模控制[J]. 西安工程大学学报, 2024, 38(2): 85-92.
[17] 贾华, 刘延俊, 王雨, 等. 六轴机械臂神经网络自适应终端滑模控制[J]. 西安交通大学学报, 2022, 56(11): 21-30.
[18] LIN C J, SIE T Y, CHU W L, et al. Tracking control of pneumatic artificial muscle-activated robot arm based on sliding-mode control[J]. Actuators, 2021, 10(3): 66.
[19] WANG H Z, FANG L J, SONG T Z, et al. Model-free adaptive sliding mode control with adjustable funnel boundary for robot manipulators with uncertainties[J]. Review of Scientific Instruments, 2021, 92(6): 0037054.
[20] ZHAO J B, XIU B K, WANG J Z, et al. Adaptive task - space cooperative tracking control for manipulators with a desired trajectory estimator and a velocity observer[J]. International Journal of Robust and Nonlinear Control, 2022, 32(7): 4214-4235.
[21] 倪元相, 刘芳. 输出反馈式神经网络的机械臂轨迹跟踪控制[J/OL]. 南京师大学报 (自然科学版), (2023-09-19)[2024-12-27]. http://kns.cnki.net/kcms/detail/32.1239.n.20230918.1220.002.html.
[22] 陈明. 基于阻抗模型的双机器人对等协作控制研究[D]. 南京: 东南大学, 2018.
[23] 程志江, 李志文, 杜一鸣. 优化自抗扰的移动清洁机械臂轨迹跟踪控制[J]. 计算机集成制造系统, 2023, 29(12): 3993-4000.

【责任编辑 】

3.3.5 Analytical prediction of battery capacity degradation trajectories considering future operating condition variability（ESCI/EI）

This article has been accepted for publication in a future issue of this journal, but has not been fully edited. Content may change prior to final publication.

Analytical Prediction of Battery Capacity Degradation Trajectories Considering Future Operating Condition Variability*

Peng peng[1, 2], *Yang Ruixin*[1*], *Chen Man*[2], Wang *Peng*[1], *Lu Jiahuan*[3*] *and Xiong Rui*[1]
(1. School of Mechanical Engineering, Beijing Institute of Technology, Beijing 100081, China;
2. Energy Storage Research Institute, CSG, PGC, Guangzhou 510630, China;
3. College of Engineering, South China Agricultural University, Guangzhou 510642, China)

Abstract: Accurate prediction of battery capacity degradation trajectories is essential for ensuring device safety, yet existing analytical models often overlook the uncertainties of future operating conditions. This paper presents an analytical approach that incorporates future operating condition variability into capacity degradation trajectory prediction. A dual-exponential model is used to model the nonlinear degradation behaviors, while Box-Cox transformation with variable coefficients is applied to describe the trajectory's dependence on future operating conditions. Additionally, particle filtering is employed to dynamically predict capacity degradation trajectories and confidence intervals under random future conditions. Experimental results show that the proposed approach achieves a median root mean square error below 0.172 A·h using only the first 25 cycles, representing a 52.8% improvement in accuracy over existing methods.

Keywords: Lithium-ion battery; capacity degradation; remaining useful life prediction; analytical modelling; particle filter

1 Introduction

As the demand for clean energy continues to rise, lithium-ion batteries have become essential energy storage devices in applications such as electric vehicles, portable electronics, and electrochemical energy storage systems, thanks to their high energy density, long lifespan, and low environmental impact [1-3]. Their capacity is a critical performance metric but inevitably degrades over time, which directly impacts both device performance and potentially operational safety [4]. Therefore, capacity monitoring is crucial for ensuring the reliability and safety of lithium-ion batteries throughout their lifecycle [5-6].

Predicting battery capacity degradation trajectories is particularly important for estimating the remaining useful life of the battery, evaluating its remaining ampere-hour throughput, and ultimately enhancing device reliability, extending service life, and reducing maintenance costs [7-8]. These predictions play a critical role in preventing capacity failure and optimizing maintenance schedules.

Battery capacity degradation prediction methods can be classified into two categories: deep learning-based approaches and analytical model-based approaches. Deep learning methods, particularly those leveraging large historical datasets, have garnered considerable attention in recent years for their strong data processing capabilities and automatic feature extraction. For example, researchers have used long short-term memory (LSTM) networks to capture the temporal dependencies in battery degradation data and predict future degradation trajectories [9-13]. Other methods, such as deep convolutional neural networks (CNNs), have been applied to mine features from operational data to map degradation patterns [14-17]. While these methods perform well with extensive data, they are highly dependent on the quantity and quality

Corresponding Author, E-mail: yangruixin@bit.edu.cn, jhlu@scau.edu.cn.
Supported by National Natural Science Foundation of China (52477209, 52407246, 52107222) and the Science and Technology Project of China Southern Power Grid Co., Ltd. (STKJXM20210097).
Digital Object Identifier: 10.23919/CJEE.2025.000180

of training data, can be sensitive to noise, and may lack reliability under extreme operating conditions.

In contrast, analytical model-based approaches offer higher interpretability and robustness by explicitly defining the relationship between cycles and capacity through mathematical equations. These models typically use simple functional forms such as linear, polynomial, logarithmic, and exponential equations to map cycle numbers to degradation trajectories, providing stable predictions based on extrapolation [18-21]. However, most existing analytical models assume that future operating conditions will remain consistent with historical data, neglecting variability in future usage conditions. This limitation reduces the accuracy and applicability of predictions in real-world scenarios [22-23]. To address this, some studies integrate deep learning methods that consider both historical degradation patterns and the variability of future operating conditions [24-25]. Despite these efforts, such methods remain fundamentally deep learning-driven, and still face challenges related to data dependency and reliability.

Given these challenges, there is a clear need for analytical modeling methods that account for variability in future operating conditions, offering more robust and reliable predictions for real-world applications. To meet this need, this paper proposes a novel analytical modeling and prediction approach that incorporates variability in future operating conditions into the prediction of battery capacity degradation trajectories. The proposed method utilizes a dual-exponential model to capture the nonlinear decay of battery capacity, applies a Box-Cox transformation with variable coefficients to represent the dependency of degradation trajectories on future conditions, and uses particle filtering to dynamically predict degradation trajectories and their confidence intervals under varying conditions. The effectiveness of this approach is validated using a dataset covering 55 battery samples, with variable operating conditions.

The remainder of this paper is organized as follows: Section 2 presents the dataset of battery capacity degradation under varying operating conditions. Section 3 outlines the proposed analytical modeling and prediction methods. Section 4 discusses the results and analysis, and Section 5 draws the conclusions.

2 Battery degradation data

Batteries in real-world applications are often subjected to dynamic external factors, such as fluctuating currents and temperatures, which lead to varying operating conditions. This variability complicates the prediction of battery capacity degradation trajectories, making it essential to consider how future operating conditions might influence degradation.

For this study, we utilize a battery capacity degradation dataset jointly developed by Beijing Institute of Technology and the Massachusetts Institute of Technology [26]. The dataset includes degradation test data for 55 commercial LR1865SZ lithium-ion batteries (nominal capacity 2.4 A·h, operating voltage range of 3.0 V to 4.2 V, and tested at 25 ℃).

The testing process comprises two phases: an early constant-current cycling phase followed by a random-current cycling phase.

In the early constant-current phase, the batteries are discharged at a constant current of 2*C*, followed by charging at 0.5*C* constant current to 4.2 V. The charging then switches to constant voltage mode until the charging current drops below 0.048 A. In the random-current cycling phase, the batteries are discharged at 3*C* constant current and then charged with a randomly selected current (1*C*, 2*C*, or 3*C*) until reaching 4.2 V.

The resulting battery capacity degradation trajectories from this dataset are shown in Fig. 1, providing a comprehensive view of the impact of varying operating currents on capacity loss.

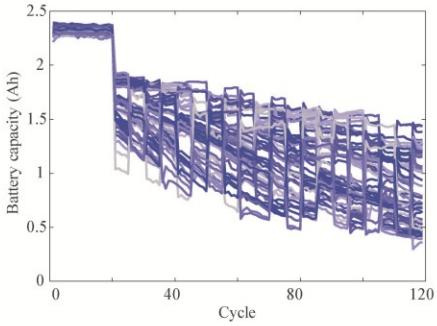

Fig. 1 Battery capacity degradation trajectories under varying current profiles. Different colors indicate different batteries

The test results indicate that the full-life degradation trajectory of the batteries exhibits typical nonlinear characteristics. Under randomly varying current loads, the degradation trajectory displays discontinuous oscillations, which significantly complicate prediction. Therefore, accurately modeling the degradation trajectory requires a method that can capture and handle these discontinuous oscillatory behaviors, ensuring the reliability and precision of the degradation predictions.

3 Methodology

The proposed battery capacity degradation trajectory prediction process, which accounts for future operating condition variability, is shown in Fig. 2. This method is a purely mathematical analytical framework that predicts future capacity degradation based on the battery's historical degradation trajectory and a customized usage plan for the future.

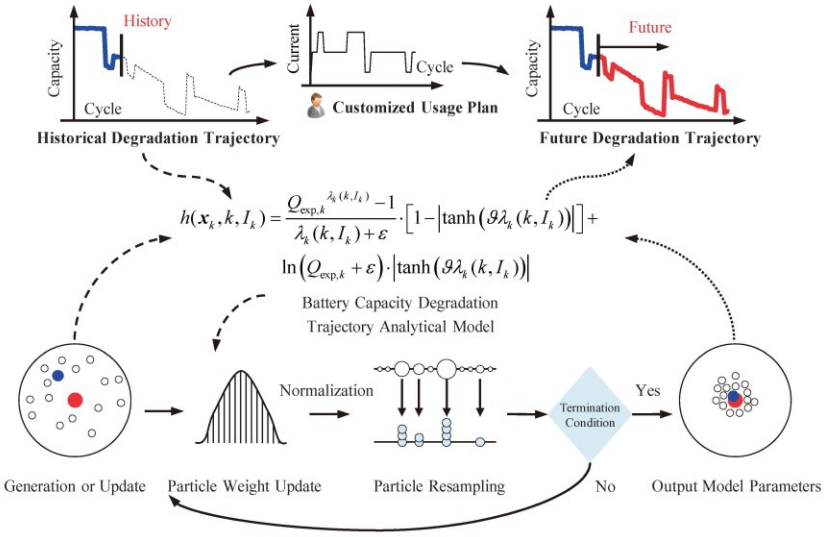

Fig. 2 Flowchart of the proposed prediction method considering future operating profile variability

3.1 Capacity degradation trajectory model

Due to the combined effects of complex physical and chemical processes within the battery, the capacity degradation trajectory generally follows a nonlinear decay pattern. The double-exponential model, which can describe multiple degradation rates, is widely recognized as an effective analytical tool for capturing such nonlinear degradation behaviors [20]. The model can be expressed as

$$Q_{\exp,k}=\left|p_1e^{p_{2,k}}+p_3e^{p_{4,k}}\right| \tag{1}$$

where k represents the cycle number, $Q_{\exp,k}$ is the predicted capacity value of the battery at the k-th cycle in the double-exponential trajectory model, $p_{1,k}$, $p_{2,k}$, $p_{3,k}$ and $p_{4,k}$ are the corresponding model parameters for the k-th cycle, respectively. It is important to note that this model does not account for the variability of operational conditions throughout the entire lifespan of the battery; therefore, it is primarily used in this paper to approximate the overall nonlinear trend of capacity degradation.

To account for the variability of future operating conditions, the future operating current is incorporated into the capacity degradation trajectory model. To capture the discontinuous oscillatory pattern of capacity degradation under varying operating conditions, and inspired by the Box-Cox transformation that improves the normality of data distributions [27-28], we employ a Box-Cox transformation with continuous variable coefficients to describe the dependence of the capacity degradation

trajectory on future varying operating currents. This can be formulated as

$$Q_k = \begin{cases} \dfrac{Q_{\exp,k}^{\ \lambda_k} - 1}{\lambda_k}, & \lambda_k \neq 0 \\ \ln Q_{\exp,k}, & \lambda_k = 0 \end{cases} \tag{2}$$

where Q_k represents the predicted battery capacity at the k-th cycle, considering the variability of future operating conditions, λ_k is the transformation coefficient at the k-th cycle, which depends on both the cycle number and the future operating current plan. Herein, a bivariate non-homogeneous relationship is used to analyze the dependence on both the cycle number and the future operating current plan, which can be written by

$$\lambda_k = q_1 k^{q_2} + q_3 I_k^{q_4} + q_5 k I_k + q_6 \tag{3}$$

where I_k represents the planned operating current for the k-th future cycle. Herein, the discharge current is used as an example to illustrate the effect of considering cycle variability, the parameters $q_{1,k}$, $q_{2,k}$, $q_{3,k}$, $q_{4,k}$, $q_{5,k}$ and $q_{6,k}$ correspond to the transformation coefficients for the k-th cycle, which are used to enhance the model's ability to describe the nonlinearity and discontinuity of the capacity degradation trajectory under future varying operating conditions.

3.2 Parameter update

The update of trajectory model parameters is fundamental for predicting capacity degradation trajectories. Considering the nonlinear and discontinuous nature of the model, this paper employs particle filtering for the parameter update of the degradation trajectory model. Particle filtering is a Monte Carlo-based approximate Bayesian filtering method that can estimate model parameters through the sample mean of a particle set, making it robust to the nonlinear and discontinuous behaviors of the system model [29-30].

To facilitate the parameter update, a state vector x is established based on the constructed trajectory model

$$\boldsymbol{x}_k = \left[\boldsymbol{p}_k, \boldsymbol{q}_k\right]^{\mathrm{T}} \tag{4}$$

where $\boldsymbol{p}_k$ and $\boldsymbol{q}_k$ are the parameter vectors of the double-exponential model and the transformation coefficient vector corresponding to the k-th cycle, respectively. Their mathematical expressions can be written as

$$\begin{cases} \boldsymbol{p}_k = \left[p_{1,k}, p_{2,k}, p_{3,k}, p_{4,k}\right]^{\mathrm{T}} \\ \boldsymbol{q}_k = \left[q_{1,k}, q_{2,k}, q_{3,k}, q_{4,k}, q_{5,k}, q_{6,k}\right]^{\mathrm{T}} \end{cases} \tag{5}$$

Battery aging is typically a long-term process, so the trajectory model parameters are assumed to change slowly over time. The state transition equation can be expressed as

$$\boldsymbol{x}_{k+1} = \boldsymbol{F}\boldsymbol{x}_k + \boldsymbol{w}_k \tag{6}$$

where $\boldsymbol{w}_k$ represents the system process noise at the k-th cycle, assumed to follow a Gaussian distribution with a mean of zero and a corresponding covariance of $\boldsymbol{Q}_{nk}$. $\boldsymbol{F}$ is the state transition matrix, assumed to be an identity matrix.

To relate the state vector to the capacity degradation observations, the system observation equation is established based on the capacity trajectory model

$$Q_k = h(\boldsymbol{x}_k, k, I_k) + v_k \tag{7}$$

where v_k is the system measurement noise for the k-th cycle, assumed to follow a Gaussian distribution with a mean of zero, and the corresponding covariance is R_k. The function $h(\boldsymbol{x}_k, k, I_k)$ is the system observation function, which can be simplified using the hyperbolic tangent function as follows

$$\begin{aligned} h(\boldsymbol{x}_k, k, I_k) = \frac{Q_{\exp,k}^{\ \lambda_k} - 1}{\lambda_k + \varepsilon} \cdot \left[1 - \left|\tanh\left(\vartheta\lambda_k\right)\right|\right] + \\ \ln\left(Q_{\exp,k} + \varepsilon\right) \cdot \left|\tanh\left(\vartheta\lambda_k\right)\right| \end{aligned} \tag{8}$$

where ε is the regularization parameter used to ensure the validity of division and logarithmic operations, and ϑ is the smoothing transition constant used to achieve smooth transitions in the transformation process.

Based on the historical capacity degradation trajectory observations $[Q_1, Q_2, \ldots, Q_k]$, the key to estimating the trajectory model parameters is calculating the probability distribution $P(\boldsymbol{x}_{1:k}|Q_{1:k})$ of the state vector $\boldsymbol{x}_k$. A discrete particle set of size N is constructed to represent the candidate state vectors. Using Monte Carlo simulation principles, the proportion of particles that are close to the true values can be increased by updating based on the observations, which is expected to approximate the model parameters. The particle importance evaluation is the primary step for this update. Based on the

observation function, the importance of each particle can be quantified by measuring the discrepancy between the predicted and actual observation, leading to the weight update equation

$$w_k^i = w_{k-1}^i \frac{P\left(Q_k \middle| \boldsymbol{x}_k^i\right) P\left(\boldsymbol{x}_k^i \middle| \boldsymbol{x}_{k-1}^i\right)}{\Gamma\left(\boldsymbol{x}_k^i \middle| \boldsymbol{x}_{k-1}^i, Q_{1:k}\right)} \tag{9}$$

where w_k^i is the importance weight of the i-th particle corresponding to the state vector in the k-th cycle, i takes values from 1 to N, and $\Gamma(\boldsymbol{x}_k^i|\boldsymbol{x}_{k-1}^i, Q_{1:k})$ is the reference distribution under Bayesian importance sampling, assumed to be the prior density

$$\Gamma\left(\boldsymbol{x}_k^i \middle| \boldsymbol{x}_{k-1}^i, Q_{1:k}\right) = P\left(\boldsymbol{x}_k^i \middle| \boldsymbol{x}_{k-1}^i\right) \tag{10}$$

Thus, the weight update equation simplifies to

$$w_k^i = w_{k-1}^i P\left(Q_k \middle| \boldsymbol{x}_k^i\right) \tag{11}$$

Particle resampling is a critical process to increase the proportion of particles that are close to the true values. To facilitate resampling, particle weights should be normalized

$$w_k^i = \frac{w_k^i}{\sum_{j=1}^{N} w_k^j} \tag{12}$$

Then, by resampling randomly, particles with high weights are duplicated, and those with low weights are eliminated, promoting the particle set to approximate the model parameters

$$\left\{\boldsymbol{x}_k^i, w_k^i\right\}_{i=1}^{N} \to \left\{\boldsymbol{x}_k^i, \frac{1}{N}\right\}_{i=1}^{N} \tag{13}$$

According to the Monte Carlo sampling principle, when the particle set size N tends to infinity, the target probability distribution $P(\boldsymbol{x}_{1:k}|Q_{1:k})$ can be approximated by the following equation

$$P\left(\boldsymbol{x}_{1:k} \middle| Q_{1:k}\right) \approx \frac{1}{N} \sum_{i=1}^{N} w_k^i \delta\left(\boldsymbol{x}_k^i - \boldsymbol{x}_k\right) \tag{14}$$

where $\delta(\cdot)$ is the Dirac delta function.

Finally, the model parameters for the battery capacity degradation trajectory can be approximated as the expectation of the state vector in the particle set, expressed as:

$$\boldsymbol{x}_k^* = \frac{1}{N} \sum_{i=1}^{N} \boldsymbol{x}_k^i \tag{15}$$

where $\boldsymbol{x}_k^*$ is the estimated battery capacity degradation trajectory model parameters for the k-th cycle.

3.3 Capacity degradation trajectory prediction

Let the battery currently be in the k-th cycle, and the target cycle number L to be predicted, along with the corresponding future current plan $[I_{k+1}, I_{k+2}, \ldots, I_{k+L}]$. Based on the capacity degradation trajectory model parameters obtained by particle filtering, the future capacity degradation trajectory can be calculated using the observation function

$$\begin{bmatrix} Q_{k+1} = h(\boldsymbol{x}_k^*, k+1, I_{k+1}) \\ Q_{k+2} = h(\boldsymbol{x}_k^*, k+2, I_{k+2}) \\ \vdots \\ Q_{k+L} = h(\boldsymbol{x}_k^*, k+L, I_{k+L}) \end{bmatrix}^{\mathrm{T}} \tag{16}$$

where $[Q_{k+1}, Q_{k+2}, \ldots, Q_{k+L}]$ is the battery capacity degradation trajectory under the future current plan $[I_{k+1}, I_{k+2}, \ldots, I_{k+L}]$.

Thanks to the particle set used in particle filtering, each candidate particle can index the corresponding candidate model parameter vector. Based on this, a set of candidate capacity degradation trajectories of size N can be generated through Monte Carlo simulation. These trajectories can be approximated by a normal distribution to estimate the confidence intervals for the future capacity degradation trajectory, expressed as

$$\begin{cases} Q_{k,\mathrm{U}} = \dfrac{\sum_{i=1}^{N} Q_k^i}{N} + z(p) \sqrt{\dfrac{\sum_{i=1}^{N} \left| Q_k^i - \dfrac{1}{N} \sum_{i=1}^{N} Q_k^i \right|}{N-1}} \\ Q_{k,\mathrm{L}} = \dfrac{\sum_{i=1}^{N} Q_k^i}{N} - z(p) \sqrt{\dfrac{\sum_{i=1}^{N} \left| Q_k^i - \dfrac{1}{N} \sum_{i=1}^{N} Q_k^i \right|}{N-1}} \end{cases} \tag{17}$$

where $Q_{k,\mathrm{U}}$ and $Q_{k,\mathrm{L}}$ are the upper and lower bounds of the confidence interval for the future capacity degradation trajectory, respectively, Q_k^i is the predicted capacity for the k-th cycle corresponding to the state vector of the i-th particle index, and $z(p)$ is the inverse cumulative distribution function [31], which depends on the confidence level p, and is expressed as:

$$\begin{cases} z(p) = -\sqrt{2} \cdot \varphi(2p) \\ \varphi^{-1}(x) = \dfrac{2}{\sqrt{\pi}} \int_x^{\infty} e^{-t^2} \mathrm{d}t \end{cases} \tag{18}$$

The prediction performance of the trajectory analysis model is evaluated by the root mean square error (RMSE) between the predicted and actual values of the battery degradation trajectory, expressed as

$$E_{\text{rmse}} = \sqrt{\frac{\sum_{i=k+1}^{k+1+L} \left(Q_{\text{test},i} - Q_i\right)^2}{L}} \tag{19}$$

where E_{rmse} is the RMSE between the predicted and actual values, and $Q_{\text{test},i}$ is the actual capacity value for the k-th cycle. To provide a more intuitive representation of the prediction error, the RMSE is also expressed as a percentage of the battery's nominal capacity. This approach allows for a clear display of the prediction error levels in practical applications, making the prediction error comparable across batteries of different capacities.

4 Results and analysis

4.1 Initialization

To validate the predictive performance of the proposed method, this study uses a capacity degradation dataset under varying operating conditions from 55 lithium-ion batteries. Since the proposed method improves upon the double-exponential model by accounting for operational condition variability, a prediction method driven solely by the double-exponential model is chosen as the baseline, with the double-exponential model serving as the observation equation [20]. This comparison allows for the validation of the proposed method's effectiveness and superiority in handling complex operating condition variability, clearly demonstrating the performance improvement of the proposed approach.

During validation, we set the particle size for updating the battery capacity degradation trajectory model parameters to 300, with the system measurement noise covariance set to 0.001. The process noise covariance matrices for the double-exponential model and the proposed method are configured as diag [10^{-5}, 10^{-7}, 10^{-9}, 10^{-6}] and diag [10^{-3}, 10^{-8}, 10^{-3}, 10^{-8}, 10^{-7},10^{-6}, 10^{-6}, 10^{-6}, 10^{-8}, 10^{-6}], respectively. The regularization parameter and smoothing transition parameter are set to 10^{-9} and 10^{-8}.

4.2 Capacity degradation prediction

Historical capacity degradation data form the basis for predicting future trajectories, and the amount of historical data used is a critical factor influencing performance. To simulate varying amounts of historical data, we select six prediction starting points: the 25th, 40th, 55th, 70th, 85th, and 100th cycles. For each starting point, we predict the remaining degradation trajectory of all samples and present the RMSE of the predictions as a box plot, as shown in Fig. 3.

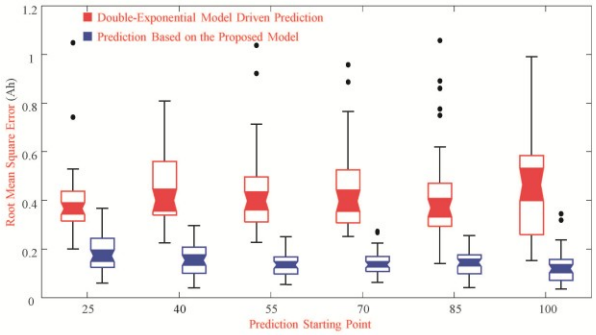

Fig. 3 Statistical comparison of prediction results for battery capacity degradation trajectories

The results show that, regardless of the chosen prediction starting point, the RMSE of predictions driven by the proposed method is significantly lower than that of the double-exponential model. Specifically, the median RMSE for the double-exponential model exceeds 0.365 A·h, indicating limited prediction accuracy. In contrast, the proposed method reduces the median RMSE to below 0.172 A·h, improving accuracy by over 52.8%. This substantial reduction highlights the importance of considering operating condition variability and validates the effectiveness of the proposed method.

Further analysis reveals that as the prediction starting point moves later and more historical data is used, the prediction accuracy driven by the double-exponential model shows little improvement and even deteriorates in some cases. On the other hand, the prediction error of the proposed method decreases as more historical data is incorporated, indicating that the proposed method more effectively utilizes historical data for capacity degradation trajectory prediction. Notably, the proposed method can achieve precise early predictions (with a median RMSE of less than 0.172 A·h) using only the first 25 cycles. After adding data from the subsequent 30 cycles, the relative error falls below 5.6%. This further confirms the efficiency and practicality of the proposed method.

In summary, the proposed method shows significant advantages in historical data utilization, prediction accuracy, and stability, confirming its potential for practical applications.

Three representative battery samples (Samples I to III), which correspond to varying current plans from sparse to frequent, are further selected for in-depth analysis. The prediction results for these samples using both the proposed and baseline methods are shown in Fig. 4, with the 99.7% confidence interval included. We focus on prediction starting points at the 25th, 40th, and 55th cycles, which are crucial for early-stage predictions.

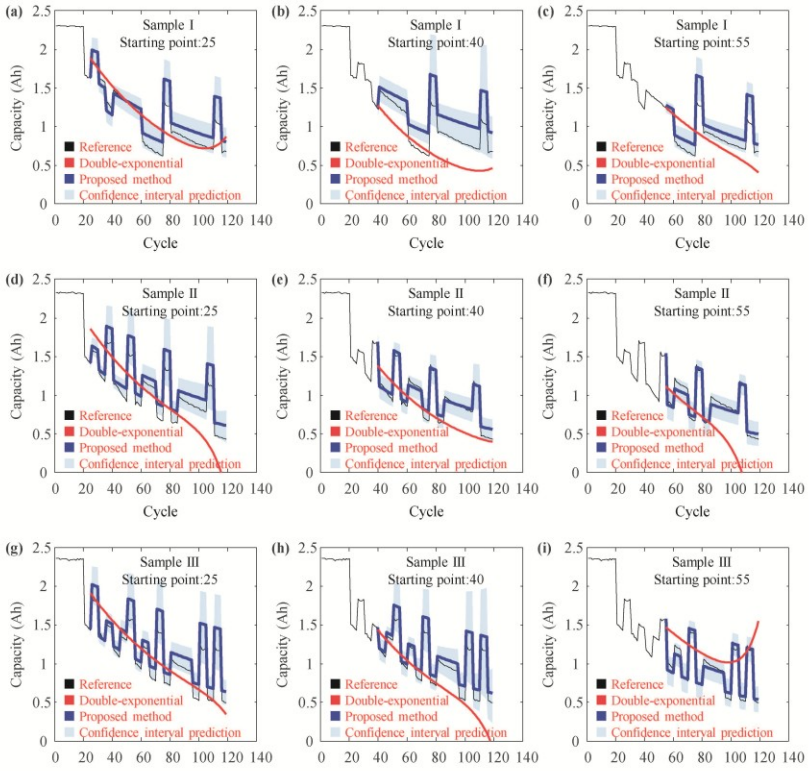

Fig. 4 Battery Capacity Degradation Trajectory Prediction Results: (a) to (c) show the prediction results for Sample I at cycles 25, 40, and 55, respectively; (d) to (f) show the prediction results for Sample II at cycles 25, 40, and 55, respectively; (g) to (i) show the prediction results for Sample III at cycles 25, 40, and 55, respectively.

Figs. 4a to 4c show the predicted degradation trajectories for Battery Sample I, where current

changes are sparse. The results show that predictions based on the double-exponential model fail to capture the oscillatory behavior of the degradation trajectory under varying operating conditions. This is because the double-exponential model cannot adapt to future changes in operating conditions. In contrast, the proposed method accurately captures the discontinuous oscillations caused by changes in operating conditions. Figs. 4d-4f and 4g-4i display predictions for Samples II and III, which correspond to more frequent current changes. The proposed method outperforms the baseline in predicting these oscillations, further validating its robustness.

As more historical data becomes available, predictions based solely on the double-exponential model tend to diverge from the actual measured trajectories, whereas predictions from the proposed method converge more closely to the actual measurements. This pattern aligns with the results shown in Fig. 3 and illustrates the proposed method's superior ability to leverage historical data for more accurate long-term predictions. While the early prediction error is larger when starting at the 25th cycle, the 99.7% confidence interval for this prediction nearly encompasses the actual measured trajectory, suggesting that the proposed method can provide highly reliable early warnings, even with limited data. This stability and reliability are due to the analytically solvable mathematical model incorporated into the proposed method.

In conclusion, the proposed method demonstrates significant advantages in predicting battery capacity degradation trajectories. It not only excels in predicting under various current plans but also provides reliable high-confidence predictions even in data-scarce scenarios. These strengths confirm the method's effectiveness and robustness in practical applications, making it a valuable tool for battery management systems.

5 Conclusions

This paper addresses the limitation of existing battery capacity degradation trajectory models that neglect variability in future operating conditions. We propose a novel modeling and prediction method that incorporates future condition variability, leveraging a double-exponential model to capture the nonlinear decay of capacity, a Box-Cox transformation with variable coefficients to analyze the influence of future operating conditions, and particle filtering to dynamically predict the degradation trajectory and its confidence intervals.

We validated the proposed method using a dataset of 55 battery samples with varying degradation conditions. The results demonstrate that the method captures the discontinuous oscillations in degradation trajectories caused by changes in operating conditions, without relying on deep learning techniques. The method also achieves precise early predictions, with a median RMSE of less than 0.172 Ah using only the first 25 cycles of data, which represents an improvement of 52.8% over the conventional analytical model-based approach.

In addition to improving prediction accuracy and stability, the proposed method accounts for future operating condition variability, making it a more reliable solution for capacity degradation prediction in battery management systems. These findings highlight the potential of the method for practical applications, offering enhanced efficiency and robustness in predicting battery degradation trajectories.

While the double-exponential model and particle filtering are used in this study as illustrative examples. Future work could explore alternative models or more advanced parameter update methods to further enhance prediction performance.

References

[1] J Tian, Y Fan, T Pan, et al. A critical review on inconsistency mechanism, evaluation methods and improvement measures for lithium-ion battery energy storage systems. *Renewable and Sustainable Energy Reviews*, 2024, 189: 113978.

[2] K Li, Y Li, X Rui, et al. Experimental study on the effect of state of charge on failure propagation characteristics within battery modules. *Chinese Journal of Electrical Engineering*, 2023, 9(3): 3-14.

[3] J Gupta, R Maurya, S R Arya. Designing an on-board charger to efficiently charge multiple electric vehicles. *Chinese Journal of Electrical Engineering*, 2023, 9(2): 38-56.

[4] S Vignesh, HS Che, J Selvaraj, et al. State of health (SoH)

estimation methods for second life lithium-ion battery-Review and challenges. *Applied Energy*, 2024, 369: 123542.

[5] Y Mazzi, HB Sassi, F Errahimi. Lithium-ion battery state of health estimation using a hybrid model based on a convolutional neural network and bidirectional gated recurrent unit. *Engineering Applications of Artificial Intelligence*, 2024, 127: 107199.

[6] B Yang, Y Qian, Q Li, et al. Critical summary and perspectives on state-of-health of lithium-ion battery. *Renewable and Sustainable Energy Reviews*, 2024, 190: 114077.

[7] J Lu, R Xiong, J Tian, et al. Deep learning to predict battery voltage behavior after uncertain cycling-induced degradation. *Journal of Power Sources*, 2023, 581: 233473.

[8] S Khaleghi, MS Hosen, JV Mierlo, et al. Towards machine-learning driven prognostics and health management of Li-ion batteries. A comprehensive review. *Renewable and Sustainable Energy Reviews*, 2024, 192: 114224.

[9] Y Zhang, R Xiong, H He, et al. Long short-term memory recurrent neural network for remaining useful life prediction of lithium-ion batteries. *IEEE Transactions on Vehicular Technology*, 2018, 67(7): 5695-5705.

[10] Y Wang, J Zhu, L Cao, et al. Long short-term memory network with transfer learning for lithium-ion battery capacity fade and cycle life prediction. *Applied Energy*, 2023, 350: 121660.

[11] G Lyu, H Zhang, Q Miao. Parallel state fusion LSTM-based early-cycle stage lithium-ion battery RUL prediction under Lebesgue sampling framework. *Reliability Engineering & System Safety*, 2023, 236: 109315.

[12] W Gomez, FK Wang, JH Chou. Li-ion battery capacity prediction using improved temporal fusion transformer model. *Energy*, 2024, 296: 131114.

[13] Z Wang, N Liu, Y Guo. Adaptive sliding window LSTM NN based RUL prediction for lithium-ion batteries integrating LTSA feature reconstruction. *Neurocomputing*, 2021, 466: 178-189.

[14] J Du, C Zhang, S Li, et al. Two-stage prediction method for capacity aging trajectories of lithium-ion batteries based on Siamese-convolutional neural network. *Energy*, 2024, 295: 130947.

[15] X Yang, H Xie, L Zhang, et al. Early-stage degradation trajectory prediction for lithium-ion batteries: A generalized method across diverse operational conditions. *Journal of Power Sources*, 2024, 612: 234808.

[16] M Lin, Y You, J Meng, et al. Lithium-ion battery degradation trajectory early prediction with synthetic dataset and deep learning. *Journal of Energy Chemistry*, 2023, 85: 534-546.

[17] S Kim, H Jung, M Lee, et al. Model-free reconstruction of capacity degradation trajectory of lithium-ion batteries using early cycle data. *ETransportation*, 2023, 17: 100243.

[18] R Xiong, Y Zhang, J Wang, et al. Lithium-ion battery health prognosis based on a real battery management system used in electric vehicles. *IEEE Transactions on Vehicular Technology*, 2018, 68(5): 4110-4121.

[19] Y Xing, EWM Ma, KL Tsui, et al. An ensemble model for predicting the remaining useful performance of lithium-ion batteries. *Microelectronics reliability*, 2013, 53(6): 811-820.

[20] W He, N Williard, M Osterman, et al. Prognostics of lithium-ion batteries based on Dempster–Shafer theory and the Bayesian Monte Carlo method. *Journal of Power Sources*, 2011, 196(23): 10314-10321.

[21] F Yang, D Wang, Y Xing, et al. Prognostics of Li (NiMnCo) O2-based lithium-ion batteries using a novel battery degradation model. *Microelectronics Reliability*, 2017, 70: 70-78.

[22] Z Chen, Q Zhang, J Lu, et al. Optimization-based method to develop practical driving cycle for application in electric vehicle power management: A case study in Shenyang, China. Energy, 2019, 186: 115766.

[23] X Zhao, X Zhao, Q Yu, et al. Development of a representative urban driving cycle construction methodology for electric vehicles: A case study in Xi'an. Transportation Research Part D: Transport and Environment, 2020, 81: 102279.

[24] J Lu, R Xiong, J Tian, et al. Battery degradation prediction against uncertain future conditions with recurrent neural network enabled deep learning. *Energy Storage Materials*, 2022, 50: 139-151.

[25] J Lu, R Xiong, J Tian, et al. Deep learning to predict battery voltage behavior after uncertain cycling-induced degradation. Journal of Power Sources, 2023, 581: 233473.

[26] J Lu, R Xiong, J Tian, et al. Battery Degradation Dataset (Fixed Current Profiles and Arbitrary Uses Profiles). 2022.

https://data.mendeley.com/datasets/kw34hhw7xg/3.

[27] Y Zhang, R Xiong, H He, et al. Lithium-ion battery remaining useful life prediction with Box–Cox transformation and Monte Carlo simulation. *IEEE Transactions on Industrial Electronics*, 2018, 66(2): 1585-1597.

[28] Q Xue, S Shen, G Li, et al. Remaining useful life prediction for lithium-ion batteries based on capacity estimation and box-cox transformation. IEEE Transactions on Vehicular Technology, 2020, 69(12): 14765-14779.

[29] J Prakash, SC Patwardhan, SL Shah. On the choice of importance distributions for unconstrained and constrained state estimation using particle filter. *Journal of Process Control*, 2011, 21(1): 3-16.

[30] S Kim, HJ Park, JH Choi, et al. A novel prognostics approach using shifting kernel particle filter of Li-ion batteries under state changes. IEEE Transactions on Industrial Electronics, 2020, 68(4): 3485-3493.

[31] M Abramowitz, IA Stegun. Handbook of mathematical functions with formulas, graphs, and mathematical tables. Washington: US Govt. Print, 2006.

Peng Peng received a Master degree in Huazhong University of Science and Technology, Wuhan, China, in 2012.He is currently working toward a Ph.D. degree in engineering at Beijing Institute of Technology, Beijing, China.

His research interests include battery state estimation.

Ruixin Yang received dual Ph.D. degrees from Beijing Institute of Technology in China and Swinburne University of Technology in Australia. He is currently an Assistant Professor at Beijing Institute of Technology. His research interests include the basic theory and key technology of battery system management.

He has presided over projects such as the General Program and Youth Program of the National Natural Science Foundation of China, the Joint Fund of the Beijing Natural Science Foundation, etc. He has published more than 40 SCI/Ei papers and has won awards such as the First Prize for Technological Invention of the Chinese Society for Electrical Engineering and the Excellence Award for Chinese Patents.

Man Chen received a Master degree in South China University of Technology, Guangdong, China, in 2005. He is currently works at the China Southern Power Grid Power Generation Co., Ltd, Energy Storage Research Institute. He is research direction is mainly battery body application technology.

Peng Wang received a B.Eng. degree in vehicle engineering from Hefei University of Technology, Anhui, China, in 2021. He is currently working toward a Ph.D. degree in vehicle engineering at Beijing Institute of Technology, Beijing, China.

His research interests include battery aging state estimation.

Jiahuan Lu received the B.Eng. and M.Eng. degrees in vehicle engineering from Northeastern University, Shenyang, China, in 2014 and 2018, respectively, and the Ph.D. degree in mechanical engineering from Beijing Institute of Technology, Beijing, China, in 2023. He is currently an Associate Professor at the College of Engineering, South China Agricultural University, Guangzhou, China.

His research interests include intelligent battery management.

Rui Xiong (Senior Member, IEEE) received the M.Sc.Eng degree in vehicle engineering and the Ph.D. degree in mechanical engineering from Beijing Institute of Technology, Beijing, China, in 2010 and 2014, respectively.

He is a Professor and director of the International Joint Laboratory for Advanced Energy Storage and Application, at the Beijing Institute of Technology, Beijing, China. From 2019 to 2020, he was a Visiting Professor at the Massachusetts Institute of Technology, Cambridge, MA, USA. He has authored more than 200 journal papers, 5 monographs and holds more than 60 patents. His research interests include Electrified vehicles, energy storage, batteries, and machine learning.

Dr. Xiong is an IET Fellow. He has been continuously selected as the HIGHLY CITED RESEARCHER from Clarivate Analytics from 2018 to 2023. He was recipients of the First Prize of China Electrotechnical Society Technology Invention Award (1st awardee), Natural Science Award of the Ministry of Education of China (2nd awardee) and Beijing Municipal Science and Technology Invention First Prize (2nd awardee). He is the Founding Director of the Energy Storage System and Equipment Technical Committee of China Electrotechnical Society. He serves as Founding executive Editor-in-Chief for the new journal Green Energy and Intelligent Transportation. He is also the Founding Chair of the International Conference on Energy storage and electric Intelligent Vehicles (ICEIV) and served as the Conference Chair from 2017 to 2024.

3.4 学术专著

3.4.1 机械工业出版社专著

GT-AutoLion作为系统仿真工具，具有丰富的材料数据库，并且基于GT-SUITE平台可以进行多种材料体系的锂离子电池仿真以及系统集成的多物理仿真。本书介绍了GT-AutoLion的电化学基础、软件模板、求解器、后处理，并针对典型工程仿真应用介绍其仿真流程，同时进行了电池仿真的实例解析。最后，本书还介绍了如何进行电、电化学、电池包热管理以及整车动力系统集成分析的方法。本书可供与锂离子电池相关的车企、电池供应商的工程师和科研人员阅读，也可供高等院校新能源汽车等相关专业师生参考学习。

图书在版编目（CIP）数据

GT-AutoLion 锂离子电池仿真分析与实例解析 / 杨瑞鑫，卢家欢，段砚州编著. -- 北京：机械工业出版社，2025. 2. --（汽车 CAE 工程师从入门到精通系列）.
ISBN 978-7-111-77801-1

Ⅰ. U469. 720. 3

中国国家版本馆 CIP 数据核字第 2025P76C08 号

机械工业出版社（北京市百万庄大街 22 号　邮政编码 100037）
策划编辑：何士娟　　责任编辑：何士娟
责任校对：郑　婕　牟丽英　　责任印制：李　昂
河北宝昌佳彩印刷有限公司印刷
2025 年 5 月第 1 版第 1 次印刷
184mm × 260mm · 12.25 印张 · 303 千字
标准书号：ISBN 978-7-111-77801-1
定价：139.90 元

电话服务　　网络服务
客服电话：010-88361066　　机　工　官　网：www.cmpbook.com
010-88379833　　机　工　官　博：weibo.com/cmp1952
010-68326294　　金　　书　　网：www.golden-book.com
封底无防伪标均为盗版　　机工教育服务网：www.cmpedu.com

3.4.2 中国农业出版社专著

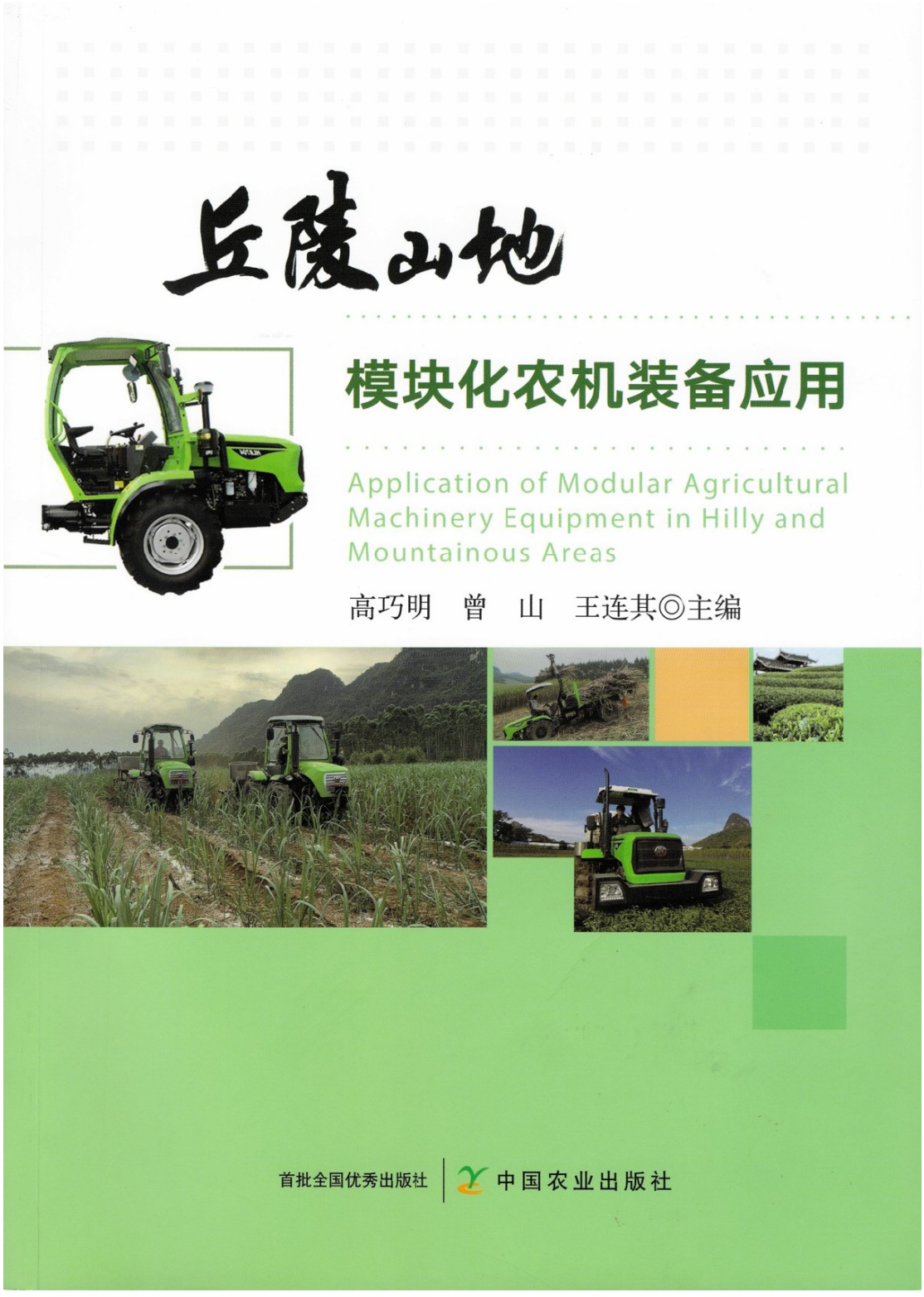

编 委 会 AUTHOR LIST

主　　编　高巧明　曾　山　王连其

副 主 编　洪暹国　王　昱　郑厚贵　黄晓斌

参编人员（以姓氏笔画为序）

马锦林　王玉江　王东雪　韦　维　邓　力
卢广伟　卢家欢　叶　航　付　颖　宁业烈
吕明站　向　宇　许　磊　李玉奇　李杰浩
杨　义　杨　闽　吴文军　吴有根　何英敏
何海华　余玉珠　张　征　张闻宇　陆　静
陆雨薇　陈荣文　林家祥　罗日广　罗光钦
罗朝东　金涛涛　周启平　周林艳　胡　波
姚圣卓　袁丽芸　莫勇武　莫清贵　唐　能
唐人辉　黄　严　黄健友　葛智文　曾福耀
雷文忠　潘延红

图书在版编目（CIP）数据

丘陵山地模块化农机装备应用 / 高巧明，曾山，王连其主编. -- 北京 ：中国农业出版社，2024. 6.
ISBN 978-7-109-32115-1

Ⅰ. S22

中国国家版本馆CIP数据核字第2024LZ0335号

丘陵山地模块化农机装备应用
QIULING SHANDI MOKUAIHUA NONGJI ZHUANGBEI YINGYONG

中国农业出版社出版
地址：北京市朝阳区麦子店街18号楼
邮编：100125
责任编辑：吴洪钟
版式设计：王 晨　　责任校对：吴丽婷
印刷：中农印务有限公司
版次：2024年6月第1版
印次：2024年6月北京第1次印刷
发行：新华书店北京发行所
开本：787mm×1092mm　1/16
印张：15
字数：360千字
定价：90.00元

四、科研成果

4.1 获得知识产权情况

4.1.1 采摘机器人果园作业区域划分方法、装置、设备及介质（A 级）

证书号第8379148号

专利公告信息

发明专利证书

发 明 名 称：采摘机器人果园作业区域划分方法、装置、设备及介质

专 利 权 人：华南农业大学

地　　址：510640 广东省广州市天河区五山路483号

发　明　人：王昱;白振冈;曾山;卢家欢;何昊翔;刘佳豪;钟学成

专　利　号：ZL 2024 1 1377730.3　　授权公告号：CN 119188747 B

专利申请日：2024年09月30日　　授权公告日：2025年10月21日

申请日时申请人：华南农业大学

申请日时发明人：王昱;白振冈;曾山;卢家欢;何昊翔;刘佳豪;钟学成

国家知识产权局依照中华人民共和国专利法进行审查，决定授予专利权，并予以公告。

专利权自授权公告之日起生效。专利权有效性及专利权人变更等法律信息以专利登记簿记载为准。

局长
申长雨

国家知识产权局

2025年10月21日

第 1 页 (共 1 页)

4.2.2 一种菠萝仿形采摘机械手（C 级）

证书号第23508552号

专利公告信息

实用新型专利证书

实用新型名称：一种菠萝仿形采摘机械手

专 利 权 人：华南农业大学

地　　址：510640 广东省广州市天河区五山路483号

发　明　人：范金鹏;李杰浩;吴浩楠;卢家欢

专　利　号：ZL 2024 2 2796373.6　　授权公告号：CN 223515357 U

专利申请日：2024年11月15日　　授权公告日：2025年11月07日

申请日时申请人：华南农业大学

申请日时发明人：范金鹏;李杰浩;吴浩楠;卢家欢

国家知识产权局依照中华人民共和国专利法进行审查，决定授予专利权，并予以公告。

专利权自授权公告之日起生效。专利权有效性及专利权人变更等法律信息以专利登记簿记载为准。

局长
申长雨

国家知识产权局
2025年11月07日

第 1 页 (共 1 页)

4.2.3 一种悬挂式开沟播种铺膜一体机（C 级）

证书号第22843260号

专利公告信息

实用新型专利证书

实用新型名称：一种悬挂式开沟播种铺膜一体机

专 利 权 人：华南农业大学;河北峥嵘农机有限公司

地　　址：510640 广东省广州市天河区五山路483号

发 明 人：曾山;孙家臣;王昱;卢家欢;李杰浩;崔朝辉;苗泉阳;陈晓流
王鹏;陈纳;吕艳婷;罗昊晖;蔡希扬;李承哲;边双印;李建东 -接续页-

专　利　号：ZL 2024 2 1843809.6　　授权公告号：CN 222852635 U

专利申请日：2024年07月31日　　授权公告日：2025年05月13日

申请日时申请人：华南农业大学;河北峥嵘农机有限公司

申请日时发明人：曾山;孙家臣;王昱;卢家欢;李杰浩;崔朝辉;苗泉阳;陈晓流
王鹏;陈纳;吕艳婷;罗昊晖;蔡希扬;李承哲;边双印;李建东 -接续页-

国家知识产权局依照中华人民共和国专利法进行审查，决定授予专利权，并予以公告。

专利权自授权公告之日起生效。专利权有效性及专利权人变更等法律信息以专利登记簿记载为准。

局长
申长雨

国家知识产权局
2025年05月13日

第 1 页 (共 2 页)

4.2.4 一种气动菠萝采摘机械手（C 级）

证书号第22779714号

专利公告信息

实用新型专利证书

实用新型名称：一种气动菠萝采摘机械手

专 利 权 人：华南农业大学

地　　址：510640 广东省广州市天河区五山路483号

发　明　人：李杰浩;吴浩楠;刘宏鲜;李城林;卢家欢

专　利　号：ZL 2024 2 1575109.3　　授权公告号：CN 222786432 U

专利申请日：2024年07月04日　　授权公告日：2025年04月25日

申请日时申请人：华南农业大学

申请日时发明人：李杰浩;吴浩楠;刘宏鲜;李城林;卢家欢

国家知识产权局依照中华人民共和国专利法进行审查，决定授予专利权，并予以公告。

专利权自授权公告之日起生效。专利权有效性及专利权人变更等法律信息以专利登记簿记载为准。

局长
申长雨

国家知识产权局
2025年04月25日

第 1 页 (共 1 页)

4.2 标准情况

4.2.1 T/CAAMM 364-2025（C 级）

中关村储能产业技术联盟自我承诺

中关村储能产业技术联盟发布的T/CNESA 1014—2024《储能用锂离子电池热失控预警算法有效性评测方法》团体标准遵循开放、公平、透明、协商一致和促进贸易和交流的原则，按照在本平台公布的《标准制定程序文件_CNESA》制定。T/CNESA 1014—2024《储能用锂离子电池热失控预警算法有效性评测方法》团体标准规定的内容符合国家有关法律法规和强制性标准的要求，没有侵犯他人合法权益。

中关村储能产业技术联盟在自愿基础上作出本承诺，并对以上承诺内容的真实性负责。

中关村储能产业技术联盟

2024年10月28日

团体详细信息			
团体名称	中关村储能产业技术联盟		
登记证号	社证字第0011714号	发证机关	北京市民政局
业务范围	从事储能产业技术研究，标准制定，承办委托，专业培训，咨询服务，成果转化，共性技术平台，会议会展，国际交流，编辑专业刊物。		
法定代表人/负责人	刘为		
依托单位名称			
通讯地址	北京市海淀区中关村东路66号世纪科贸大厦B座2510		邮编：100190

标准详细信息	
标准状态	现行
标准编号	T/CNESA 1014—2024
中文标题	储能用锂离子电池热失控预警算法有效性评测方法
英文标题	Evaluation methods for the effectiveness of thermal runaway warning algorithms for lithium-ion batteries in energy storage systems
国际标准分类号	27.180
中国标准分类号	F 19
国民经济分类	D441 电力生产
发布日期	2024年10月25日
实施日期	2024年10月25日
起草人	熊瑞、孙潇春、陈泽宇、王晨旭、刘子豪、陈满、王青松、贾彦博、郑翔、杨瑞鑫、梅冰昂、张豪、钱昊、王垒、谢长君、张彩萍、商云龙、郭姗姗、陈奎、马迷娜、卢家欢、王卿
起草单位	北京理工大学、东北大学、南方电网调峰调频发电有限公司储能科研院、中国科学技术大学、中创新航科技集团股份有限公司、北京海博思创科技股份有限公司、武汉理工大学、北京交通大学、山东大学、潍坊学院、西南交通大学、石家庄铁道大学、华南农业大学
范围	
主要技术内容	锂离子电池是当前主流的电化学储能技术路线，但其存在热失控风险，可能引发严重的安全事故，因此开展储能用锂离子电池热失控预警尤为重要。然而，现有热失控预警算法评价维度单一且缺乏统一基准，难以实现有效预警热失控。因此，为确立一种储能用锂离子电池热失控预警算法有效性评测方法，实现测试方法的标准化，特制订本文件，为今后开展储能用锂离子电池热失控预警算法有效性评测工作提供依据。
是否包含专利信息	否
标准文本	不公开

标准公告	
标准发布公告	2024/10/25 20:37:11

首页 上一页 下一页 末页

*由中关村储能产业技术联盟于2024/10/25 20:37:11在团体标准信息平台公布，最后修改时间：2024/10/25 20:37:11

4.2.2 T/CNESA 1014-2024（C 级）

ICS 27.180
CCS F 19

CNESA

团　　体　　标　　准

T/CNESA 1014—2024

储能用锂离子电池热失控预警算法有效性评测方法

Evaluation methods for the effectiveness of thermal runaway warning algorithms for lithium-ion batteries in energy storage systems

2024－10－25 发布　　2024－10－25 实施

中关村储能产业技术联盟　　发 布

中关村储能产业技术联盟是中国社会组织5A级社团，是中国首个专注在储能领域的非营利性国际行业组织。中关村储能产业技术联盟致力于通过影响政府政策的制定和储能应用的推广促进储能产业的健康有序发展。

中关村储能产业技术联盟聚集了优秀的储能技术厂商、新能源产业公司、电力系统以及相关领域的科研院所和高校，覆盖储能全产业链各参与方。中关村储能产业技术联盟在协同政府主管部门研究制定中国储能产业发展战略、倡导产业发展模式、确定中远期产业发展重点方向、整合产业力量推动建立产业机制等工作中，发挥着举足轻重的先锋作用。

The China Energy Storage Alliance（CNESA） is a grade 5A China Social Organization and China's first non-profit organization dedicated to the international energy storage industry. CNESA is committed to the healthy development of the energy storage industry through positive influence of government policy and promotion of energy storage applications.

CNESA's membership body includes domestic and international organizations involved in all aspects of the energy storage industry, from technology manufacturers, renewable energy corporations, research bodies, institutes of higher learning, and more. CNESA partners with government bodies to develop strategies for industry development, determine directions for medium- and long-term industry growth, consolidate efforts to establish a market mechanism, and many other projects that play a crucial role in advancing the energy storage industry in China and abroad.

地址：北京市海淀区北四环西路11号B座310室　　邮编：100190
电话：86-10-65667066　　传真：86-10-65666983
网址：http://www.cnesa.org　　邮箱：standard@cnesa.org

目　　次

前　言

本文件按照GB/T 1.1—2020《标准化工作导则　第1部分：标准化文件的结构和起草规则》的规定起草。

请注意本文件的某些内容可能涉及专利。本文件的发布机构不承担识别专利的责任。

本文件由中关村储能产业技术联盟提出并归口。

本文件起草单位：北京理工大学、东北大学、南方电网调峰调频发电有限公司储能科研院、中国科学技术大学、中创新航科技集团股份有限公司、北京海博思创科技股份有限公司、武汉理工大学、北京交通大学、山东大学、潍坊学院、西南交通大学、石家庄铁道大学、华南农业大学。

本文件主要起草人：熊瑞、孙逢春、陈泽宇、王晨旭、刘子豪、陈满、王青松、贾彦博、郑翔、杨瑞鑫、梅冰昂、张豪、钱昊、王垒、谢长君、张彩萍、商云龙、郭姗姗、陈奎、马迷娜、卢家欢、王卿。

4.3 农业农村部科研平台（T2 级）

广东省发展和改革委员会
广东省农业农村厅 文件

粤发改投资〔2024〕302 号

广东省发展改革委 广东省农业农村厅关于转下达农业专项（种子工程和动植物保护能力提升方向、农业行业能力建设方向）2024 年中央预算内投资计划的通知

广州、珠海、梅州、湛江市发展改革局（委）、农业农村局，华南农业大学，省农业技术推广中心，省农业有害生物预警防控中心：

根据《国家发展改革委关于下达农业行业能力建设和林业执法监管能力提升项目 2024 年中央预算内投资计划的通知》（发改投资〔2024〕995 号）、《国家发展改革委关于下达农业专项（种子工程和动植物保护能力提升方向）2024 年中央预算内投资计划的通知》（发改投资〔2024〕1086 号）、《农业农村部关于下达相关专项 2024 年第三批中央预算内投资农业建设项目任务清单和绩效

国家重大建设项目库、每月27日前在农业农村投资项目管理平台填报项目开工情况、投资完成情况、工程形象进度等数据，严格做好数据填报和审核工作，保证填报数据质量。请市、县发展改革部门做好国家重大建设项目库数据填报提醒、督促、审核工作，提高填报数据质量。国家发展改革委、农业农村部将进行在线监测，并将监测结果作为后续投资安排的重要参考。

四、确保完成绩效目标。本批计划的总体绩效目标是：实施现代种业提升工程，提高种质资源保护利用、品种测试、育种创新和良种繁育能力；推进动植物保护能力提升工程建设，提升动植物疫病监测、诊断、防治能力；改善农业行业基础设施和科研条件。请加强对绩效目标实现情况的监控，发现问题及时纠正，确保绩效目标如期实现。国家发展改革委将适时组织开展绩效评价。

附件：1.广东省农业相关专项2024年中央预算内投资计划及任务清单下达表

2.广东省农业专项（种子工程方向）2024年中央预算内投资计划绩效目标表

3.广东省农业专项（动植物保护能力提升方向）2024年中央预算内投资计划绩效目标表

4.广东省农业专项（农业行业能力建设方向）2024年中央预算内投资计划绩效目标表

（此页无正文）

广东省发展改革委

广东省农业农村厅

2024年9月6日

（联系人及电话：省发展改革委 张一帆，020-83133092；
省农业农村厅 何少明，020-37289381）

序号	任务名称	建设性质	建设规模	建设地点	拟开工年份	拟建成年份	投资类别	总投资	已下达投资	本次下达投资	年度建设内容	任务性质	投资安排方式	项目（法人）单位	项目责任人	日常监管直接责任单位	日常监管直接责任单位监管责任人	备注
4	广东省大埔县病死畜禽无害化收集处理场建设项目	新建	建设无害化处理厂房、清洗车间、冷库等设施2800平方米，购置病死畜禽处理机、专业运输车辆、智能监控系统等设备5台（套）。	梅州市大埔县	2024	2025	合计	1239		1239	土建工程/仪器设备购置	约束性任务	投资补助	梅州兴合肥业有限公司	张美英	大埔县农业农村局	吴国章	
							中央预算内投资	200		200								
							地方预算内投资											
							企业自有资金	1039		1039								
							银行贷款											
三	农业行业能力建设项目		建设农业科研试验基础设施项目1个				合计	1993		1993								
							中央预算内投资	1395		1395								
							地方预算内投资											
							企业自有资金	598		598								
							银行贷款											
1	农业农村部蔬菜（叶菜）全程机械化科研试验基础设施建设项目	新建	改造温室1000平米，购置仪器设备92台（套）。	广州市增城区	2021	2025	合计	1993		1993	田间工程/仪器设备购置	约束性任务	直接投资	华南农业大学	李松	广东省农业农村厅	李振柱	
							中央预算内投资	1395		1395								
							地方预算内投资											
							企业自有资金	598		598								
							银行贷款											

培训，并适当地采取施工技术考核手段，进一步强化施工专业性，保证项目施工人员技术能力，不断提升施工技术管理人员的业务素质及管理水平。

8.2 项目运行期组织机构、职能与管理方式

8.2.1 组织机构设置方案

该项目完成后，由华南农业大学负责运行管理。

项目科研基地设主任、副主任各 1 名，负责基地日常运营管理。同时，根据实际需要聘请国内知名专家组成学术指导委员会，协助主任决定科研基地的研究方向和中长期规划，审定研究课题和评价学术、科研成果，指导和检查研究进展等工作。

8.2.2 组织机构管理措施

1、科研技术管理

对每个研究方向实行专人管理，仪器实行专人负责制，进行操作和仪器利用开发培训，负责实验仪器的使用管理和日常维护等。

2、制度化管理

项目建成后，要建立管理制度，保障项目长期高效运行。通过建立管理制度，严格工作规范，将装备技术研究与集成示范推广工作完全分开，确保装备技术研究的科学、准确、公正和公平。

（1）经费来源采取多渠道争取经费，改善科研条件：积极争取国家级和省部级的支持，多方面筹集经费，改善项目区基础设施及研究条件。同时，加强软件服务，为进行高水平研究和产生高水平的研究成果创造良好的条件。

（2）制定一系列的工作管理制度，如《仪器设备管理办法》《保安管理暂行办法》和《编制外劳动用工管理暂行办法》等规章制度，使科研基地管理更规范、更科学，科研项目在科研基地内实施的严谨性、可靠性能得到保证。

8.3 劳动定员

8.3.1 人员配置

本项目运营团队主要由工程学院研究人员组成，团队共有技术人员 15 人，其中正高职称人员 6 人，副高职称人员 6 人，中级职称 3 人，专业领域涉及设施育苗、智能农机、农业信息化工程、基地土地资源管理等领域。运营团队人员结构合理、专业扎实、经验丰富，具有很好的团队合作传统。具体劳动定员明细如下表所示。

表 8-1　项目劳动定员明细表

序号	姓名	性别	出生年月	职务/职称	主要研究方向
1	幸松	男	[illegible]	教授	设施园艺智能装备
2	齐龙	男	[illegible]	副院长/研究员	农业机械化工程
3	曾山	男	[illegible]	研究员	智能农机装备
4	臧英	女	[illegible]	教授	精准种植、智能农机装备
5	罗红梅	女	[illegible]	教授	设施园艺智能装备
6	王在满	男	[illegible]	研究员	精准种植、智能农机装备
7	牟英辉	男	[illegible]	副教授	设施园艺智能装备
8	杨文武	男	[illegible]	副教授	智能农机装备
9	张明华	男	[illegible]	副研究员	蔬菜种植机械化、智能农机装备
10	王昱	女	[illegible]	副教授	智能农机装备
11	马锐军	男	[illegible]	副教授	农业信息化工程
12	李杰浩	男	[illegible]	副教授	智能农机装备
13	张闻宇	男	[illegible]	助理研究员	智能农机装备
14	卢家欢	男	[illegible]	副教授	智能农机装备
15	王伟峰	男	[illegible]	助理研究员	基地管理、土地资源管理

五、其他业绩

5.1 指导学生参加学科竞赛

5.1.1 指导完成创新创业训练项目（国家级）

国家级大学生创新训练计划平台

首 页　历年项目　结题项目　年度进展报告　通知公告　咨询问答

当前位置：首页 / 立项项目 / 学生查询 / 芒果挂果及其成熟度智能识别与自动无损采摘系统设计

项目编号: 202410564078

项目名称: 芒果挂果及其成熟度智能识别与自动无损采摘系统设计

项目类型: 创新训练项目

项目类别: 一般项目

重点支持领域:

所属学校: 华南农业大学

项目实施时间: 至

所属学科门类: 工学

所属专业大类: 自动化类

立项时间: 2024-11-19 00:00:00.000

项目成员:

姓名	年级	学号	所在院系	专业	联系电话	E-mail	是否主持人
涂镇	*		*	*	*	*	第一主持人
杨健	*		*	*	*	*	否
刘泽为	*		*	*	*	*	否
林祥烨	*		*	*	*	*	否

指导教师:

姓名	单位	专业技术职务	指导教师类型
卢家欢		副教授	第一指导教师

5.1.2 指导参加学科竞赛（C 级）

荣誉证书

常婉婷、刘家齐、黄俊涛、梁晓瑜、周晓柔同学：

你（们）的作品《低碳有形——基于智慧物联的锂离子电池缺陷检测系统》在“菱朗杯”第九届广东省汽车与农机电子环保大赛中表现优异，荣获

二等奖

指导老师：卢家欢

特发此证，以资鼓励。

广东省电子学会 广东省汽车行业协会 广东省机械行业协会

广东省电子信息行业协会 广东省测量控制技术与装备应用促进会 广东省仪器仪表行业协会

2024 年 12 月 30 日

5.1.3 指导参加大学生创新大赛（校级）

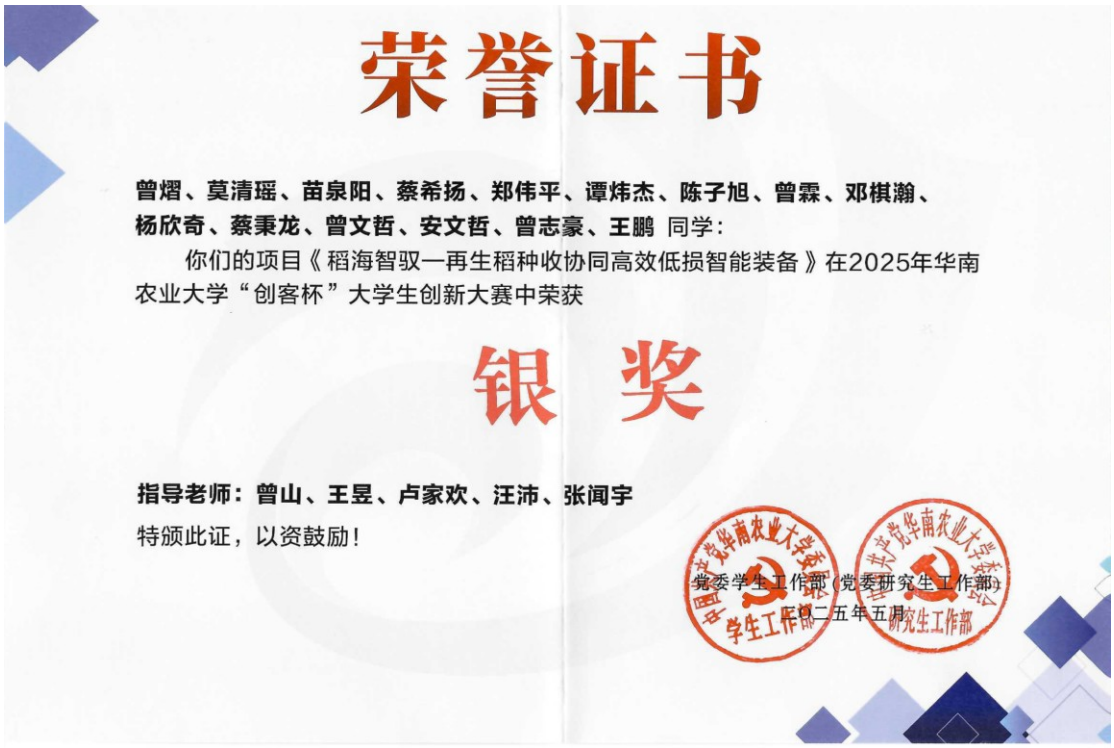

荣誉证书

曾熠、莫清瑶、苗泉阳、蔡希扬、郑伟平、谭炜杰、陈子旭、曾霖、邓棋瀚、杨欣奇、蔡秉龙、曾文哲、安文哲、曾志豪、王鹏 同学：

你们的项目《稻海智驭—再生稻种收协同高效低损智能装备》在2025年华南农业大学“创客杯”大学生创新大赛中荣获

银 奖

指导老师：曾山、王昱、卢家欢、汪沛、张闻宇

特颁此证，以资鼓励！

党委学生工作部（党委研究生工作部）

二〇二五年五月

5.2 个人荣誉

5.2.1 优秀指导教师（省部级）

荣誉证书

卢家欢老师在广东省“菱朗杯”第八届广东省汽车与农机电子环保大赛中指导学生成绩突出，被评为

优秀指导老师

特发此证，以资鼓励。

广东省电子学会 广东省汽车行业协会 广东省机械行业协会

广东省电子信息行业协会 广东省测量控制技术与装备应用促进会 广东省仪器仪表行业协会

2024 年 1 月 5 日

5.2.2 优秀指导教师（省部级）

荣誉证书

卢家欢老师在广东省“菱朗杯”第九届广东省汽车与农机电子环保大赛中指导学生成绩突出，被评为

优秀指导老师

特发此证，以资鼓励。

广东省电子学会 广东省汽车行业协会 广东省机械行业协会
广东省电子信息行业协会 广东省测量控制技术与装备应用促进会 广东省仪器仪表行业协会

2024 年 12 月 30 日

5.2.3 年度考核优秀（校级）

5.3 其他业绩

5.3.1 全球前 2%顶尖科学家（国际级）

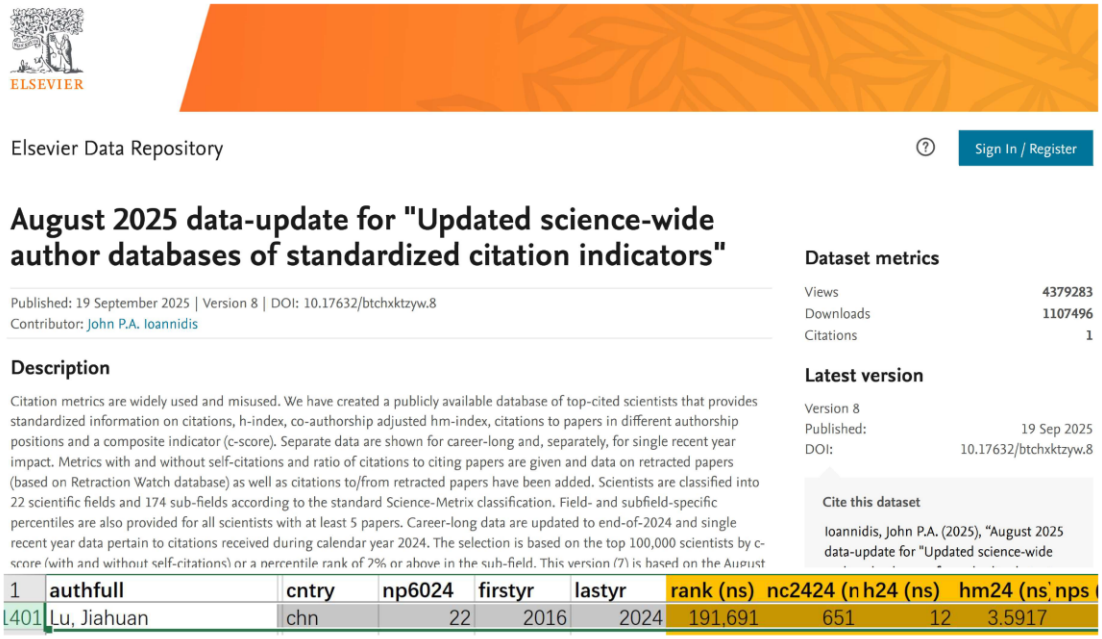

ELSEVIER

Elsevier Data Repository

Sign In / Register

August 2025 data-update for "Updated science-wide author databases of standardized citation indicators"

Published: 19 September 2025 | Version 8 | DOI: 10.17632/btchxktzyw.8
Contributor: John P.A. Ioannidis

Description

Citation metrics are widely used and misused. We have created a publicly available database of top-cited scientists that provides standardized information on citations, h-index, co-authorship adjusted hm-index, citations to papers in different authorship positions and a composite indicator (c-score). Separate data are shown for career-long and, separately, for single recent year impact. Metrics with and without self-citations and ratio of citations to citing papers are given and data on retracted papers (based on Retraction Watch database) as well as citations to/from retracted papers have been added. Scientists are classified into 22 scientific fields and 174 sub-fields according to the standard Science-Metrix classification. Field- and subfield-specific percentiles are also provided for all scientists with at least 5 papers. Career-long data are updated to end-of-2024 and single recent year data pertain to citations received during calendar year 2024. The selection is based on the top 100,000 scientists by c-score (with and without self-citations) or a percentile rank of 2% or above in the sub-field. This version (7) is based on the August

Dataset metrics

Views	4379283
Downloads	1107496
Citations	1

Latest version

Version 8
Published: 19 Sep 2025
DOI: 10.17632/btchxktzyw.8

Cite this dataset

Ioannidis, John P.A. (2025), "August 2025 data-update for "Updated science-wide

1	authfull	cntry	np6024	firstyr	lastyr	rank (ns)	nc2424 (n	h24 (ns)	hm24 (ns	nps (
401	Lu, Jiahuan	chn	22	2016	2024	191,691	651	12	3.5917	

5.3.2 IEEE PES 分委会中国区副秘书长（国际级）

No. 6080450056

Certificate of Appreciation

IEEE PES
Power & Energy Society®

IEEE Power & Energy Society Satellite Technical Committee

Sincere Appreciation is Hereby Expressed to

Jiahuan Lu

As the "IEEE PES China Satellite Technical Committee – Electric Vehicle Committee"

"Battery System Subcommittee"

Deputy Secretary General

2024 - 2025

IEEE

Chairman

IEEE PES China Satellite Technical Committee

Electric Vehicle Committee

5.3.3 我国首届电气人工智能大会分论坛主席（国家级）

博士分论坛

论坛主题： 储能电池健康与安全前沿技术

承办单位： 中国电工技术学会储能系统与装备专业委员会

主席： 卢家欢 华南农业大学

时间： 2024年12月8日 8:30-12:00

地点： 1楼扬子大宴会厅C厅

论坛介绍：

本次论坛以"储能电池健康与安全前沿技术"为主题，聚焦储能电池健康与安全领域的前沿技术，涵盖从机理解析到人工智能应用等关键创新领域。论坛旨在通过专题学术报告和专家互动，促进博士生与行业专家之间的深度学术交流，激发科研热情，助力青年学者的成长与学术进步。

活动日程

时间	报告题目	报告人	单位及职位
8:30-8:40	专业委员会主任开幕致辞		
8:40-8:55	基于迁移学习的锂电池健康状态估计	李建明	香港大学
8:55-9:10	机械负载下物理驱动的电池堆叠压力调控及仿真技术研究	蔡雪	德国亚琛工业大学 北京交通大学
9:10-9:25	人工智能在电池管理中的应用：电池状态估计及参数辨识	付俊成	西安交通大学国家储能技术产教融合创新平台(中心)
9:25-9:40	数据机理融合驱动的锂离子电池剩余寿命预测方法研究	赵明远	重庆大学
9:40-9:55	部分充电数据驱动的电池健康状态的理解与估计	林川平	西安交通大学
9:55-10:10	锂离子电池性能衰退诊断研究	孙越	北京理工大学
10:10-10:30	茶歇		
10:30-10:45	考虑多层工况预测的燃料电池混合动力汽车能量管理策略研究	徐宏扬	燕山大学
10:45-11:00	锂离子电池峰值功率预测研究	陈纳	华南农业大学
11:00-11:50	名师面对面		
11:50-12:00	证书颁发仪式		

5.3.4 电气工程、控制和机器人技术国际会议程序主席（国际级）

5.3.5 新加坡 ICEIV 分会主席（国际级）

5.3.6 主持中国科协决策咨询项目（国家级）

中 国 科 协 部 门 发 文

结项证明

中国农业机械学会:

你单位承接的2024年度决策咨询专家团队项目经专家评审，验收通过，准予结项，特此证明。

项目名称: 水果采摘机器人技术与产业发展路径与对策研究

团队名称: 智慧农业关键技术及装备创新团队

项目负责人: 卢家欢

评审结果: 合格

后续我们将结合工作需要，适时对项目成果进行加工凝练，进一步使用，请专家团队继续予以支持。

中国科协战略发展部

2025年4月25日

5.3.7 北京市优博（省部级）

北京市优秀博士学位论文

荣誉证书

卢家欢

《锂离子电池性能衰退状态、轨迹评估与衰后特性预测》

指导教师：孙逢春教授

获评 2024 年度北京市优秀博士学位论文

北京市教育委员会

二〇二五年三月

编号：YB2024048

5.3.8 学术期刊感谢信（国际级）

亲爱的卢家欢老师：

您好，感谢您于2025年12月29日 *Designs* 专题研讨会：新能源动力系统智能管理与寿命预测前沿技术| MDPI Seminar中担任主讲人。在您的大力支持与配合下，本次研讨会圆满结束。

本次研讨会小鹏通直播间和MDPI开放科学微信视频号等合计共达到约15000人次。

MDPI诚挚地感谢您与我们联合开展本次线上研讨会。同时，也感谢您前期对MDPI出版工作的支持，相信通过进一步的交流，我们可以为广大青年学者及研究人员在学术论文出版方面做出进一步指导和探讨，真诚期待着与您再次合作。

谨祝您在科研领域不断突破，取得更高的成就。

MDPI市场部
2026年1月

5.3.9 入选百千万工程突击队优秀团队（校级）

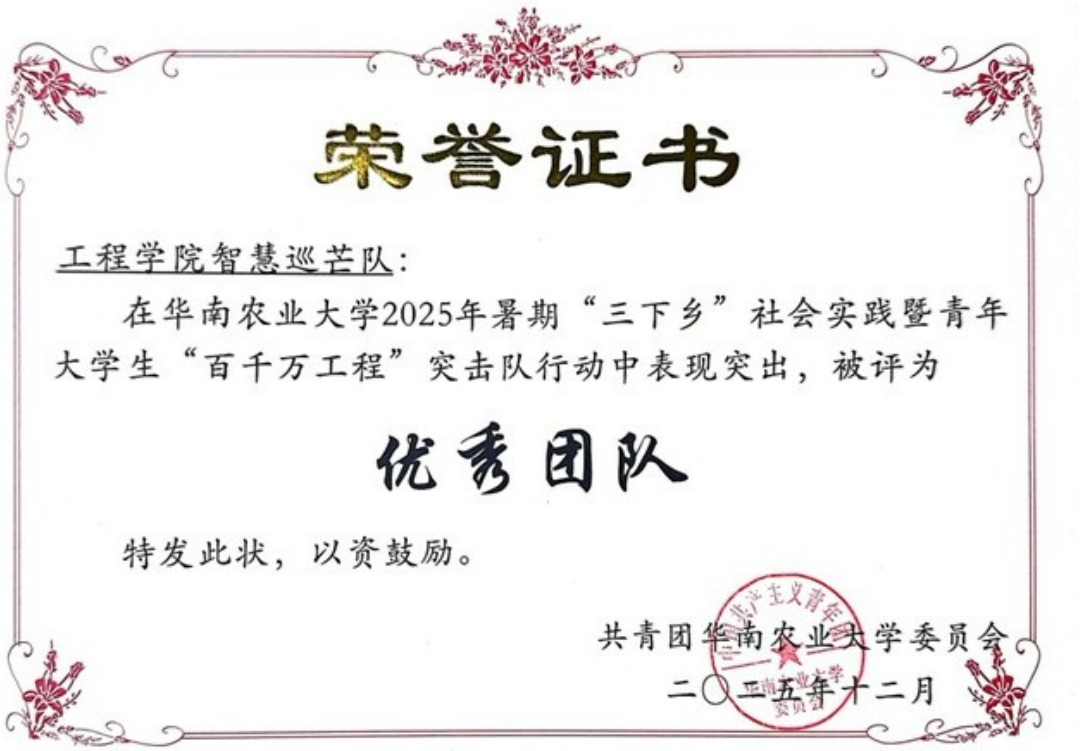

荣誉证书

工程学院智慧巡芒队：

在华南农业大学2025年暑期“三下乡”社会实践暨青年大学生“百千万工程”突击队行动中表现突出，被评为

优秀团队

特发此状，以资鼓励。

共青团华南农业大学委员会

二〇二五年十二月